# Multimode Structure of Resistive Wall Modes near the Ideal Wall Stability Limit

Jeffrey Peter Levesque

COLUMBIA UNIVERSITY

2012

**ABSTRACT**

**Multimode Structure of Resistive Wall Modes near the Ideal Wall Stability Limit**

**Jeffrey Peter Levesque**

This thesis presents the first systematic study of multimode external kink structure and dynamics in a tokamak using a high-resolution magnetic sensor set. Multimode effects are directly measured, rather than inferred from anomalies in single-mode behavior. In order to accomplish this, an extensive set of 216 poloidal and radial magnetic field sensors has been installed in the High Beta Tokamak – Extended Pulse (HBT-EP) device for high-resolution measurements of three-dimensional mode activity. An analysis technique known as biorthogonal decomposition (BD) is described, and simulations are presented to justify its use for studying kink mode dynamics in HBT-EP data. Coherent activity of multiple simultaneous modes is observed using the BD without needing to define a mode structure basis beforehand. Poloidal mode numbers up to $m = 8$ are observed via sensor arrays with full 360° coverage. Higher poloidal mode numbers are suggested by the data, but cannot be well-resolved with the available diagnostics. Toroidal mode numbers up to $n = 4$ are observed. Non-rigid, multimode activity is observed for coexisting external kinks having $m/n = 3/1$ and $6/2$ structures. Despite sharing the same helicity and same resonant surface, rotation of $6/2$ modes is independent of $3/1$ mode rotation – the $n = 2$ mode does not simply rotate with double the frequency of the $n = 1$ mode. During periods of $3/1$-dominated activity, the $6/2$ mode is observed to modulate the $3/1$ amplitude, and in brief instances can overpower the $3/1$. Statistical analysis over many shots reveals the multimode nature of the $3/1$ kink to be more significant when the resonant $q = 3$ surface begins internal, then is ejected from the plasma. This inference is based on the relative amplitudes of secondary modes during $3/1$-dominated activity, as well as spectral content of the modes. Conformal conducting wall segments were also retracted away from the plasma surface using low-order poloidal and toroidal asymmetries to excite measurable differences in low $m$- and $n$-number modes. Kink mode amplitudes increase as the wall segments are withdrawn, and non-symmetric wall configurations modulate the amplitude and frequency of the rotating modes depending upon their toroidal orientation with respect to the non-symmetric wall. Modulations of mode amplitude and rotation are larger for the toroidal wall asymmetry than for the poloidal wall asymmetry.

# Contents

# List of Figures

xi

# List of Tables

# Acknowledgments

My experience at Columbia during the past six years has been a period of great personal and professional growth. I owe this to the professors, staff, and students associated with the HBT-EP experiment. Without our tight-knit community, I would not have enjoyed graduate school nearly as much. I thank Mike Mauel, Jerry Navratil, and Dave Maurer for their leadership in running the group, and keeping our research on track. Thanks go to Nick Rivera and Jim Andrello for keeping the tokamak operational, and to former students Jeremy Hanson and Royce James for teaching me nuances of running the machine.

I am indebted to Dave Maurer for accepting a professorship at Auburn so that I may fill his role at HBT-EP. I had always considered his position the ideal job – being part of a small research group, yet still having access to a world-class tokamak. I'm glad that I will be able to continue research on HBT-EP after completing my degree.

I thank my relatives for supporting my choice of such an obscure career. I especially thank my wife Annette for putting up with me over the years, including during the late nights while writing this thesis – I dedicate this thesis to her.

# Chapter 1

# Introduction

With global energy consumption on the rise, and growing concerns over the environmental impact of society, developing improved green energy sources is necessary. Existing forms of green power generation, such as solar and wind energy, may not meet the high power density needs of heavily populated regions. These also rely on environmental conditions, and therefore cannot sustain base load requirements without significant energy storage. Conventional gigawatt-scale power plants that burn fossil fuels and can be placed close to populated areas produce greenhouse gasses. Fission power plants produce nuclear waste, and pose a proliferation problem unless carefully monitored.

A potential solution to the growing energy demands of the world lies in harnessing fusion energy [1, 2, 3]. First-generation deuterium-tritium (D-T) fusion power plants will produce low-grade radioactive waste that decays on the timescale of decades, rather than millenia as from a conventional nuclear power plant. This short-lived waste problem may be mitigated by developments of improved structural materials. Future fusion plants using aneutronic reactions offer the possibility of no nuclear waste at all.

## 1.1 Nuclear fusion

Fusion is the process of combining light nuclei into heavier elements, releasing energy in the process. The reaction with the largest cross-section and with the easiest confinement requirements is

$$D + T \longrightarrow He^4(3.5 \text{ MeV}) + n(14.1 \text{ MeV}) \tag{1.1}$$
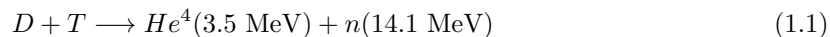
where deuterium and tritium nuclei fuse to form a helium nucleus and a fast neutron. Each reaction product has much more kinetic energy than the original particles had. In order for fusion to occur, incident nuclei must overcome Coulomb repulsion enough for the strong nuclear force to take over, which requires high kinetic energies. The likelihood of particles fusing in any given approach is low however, thus there will be many collisions that cause momentum scattering and the emission of bremsstrahlung radiation. Particles in the system will thermalize before a significant number of fusion reactions occur. When the system contains enough thermal energy for fusion rates to be significant, light elements will necessarily form a fully-ionized plasma due to the relatively low ionization energies that bind outer-shell electrons to nuclei. Keeping fusion energy production larger than loss rates will require the confinement of a hot plasma, with a temperature above the Lawson criterion [4].

## 1.2 Plasma confinement

For plasma particles to remain energetic enough for fusion to occur in the laboratory, they must be restrained from touching the material walls in a device. One way to do this is by exploiting the Lorentz force, $\vec{F} = q(\vec{E} + \vec{v} \times \vec{B})$. In the presence of a uniform magnetic field, charged particles will experience a force perpendicular to that field. This causes the particles to make closed orbits when viewed in a plane normal to the magnetic field, provided there is no electric field. The radius of this orbit is known as the Larmor radius for that particle, given by $r_L = mv_\perp/|q|B$, where $v_\perp$ refers to the component of the particle's velocity perpendicular to the field. Faster particles require a stronger field for confinement within the same space.

There is no magnetic force along the field, however, so a simple uniform field will not suffice for confinement in 3 dimensions. A common way to avoid this problem is to bend the field into a circle, or otherwise closed path, so that motion along the field will be periodic. We call this periodic coordinate the *toroidal* direction, denoted by $\phi$ in the context of this work. The field-bending necessarily creates gradients in the field as a consequence of Maxwell's equations, thus there will be associated $\vec{B} \times \nabla \vec{B}$ drifts which move the particles perpendicular to the magnetic field.

Because of the particle drifts in toroidal confinement devices, the field must be helical. Helical fields can be created by running a current through the plasma along the toroidal direction. This produces a field component that wraps around the current, which we then call the *poloidal* direction,
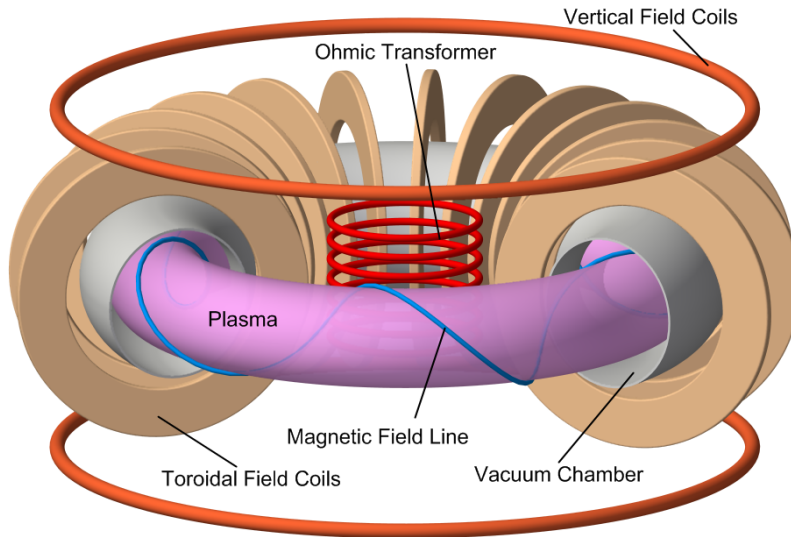
Figure 1.1: Generic features of a tokamak.

denoted by $\theta$. The resulting twist in the field causes drifts to cancel out when averaged over a poloidal transit. This twist can be quantified using the "safety factor," $q$, which is the number of transits a field line makes in the toroidal direction before returning to the same poloidal angle. The concept of having strong toroidal field combined with a plasma current producing a poloidal field is known as a *tokamak*. Figure 1.1 shows a diagram of a tokamak's generic features. To date, tokamaks have been the most successful device at reaching fusion-grade plasma conditions in a magnetic confinement scheme.

### 1.2.1 Fusion conditions

In order to achieve self-sustaining fusion reactions (where the energy released from fusion exceeds radiation and confinement losses), a plasma must be dense and hot enough, and energy must be confined long enough for reactions to persist. These requirements lead to the "fusion triple-product" condition:

$$nT\tau_E \gtrsim 5 \times 10^{21} \frac{\text{keV} \cdot \text{s}}{\text{m}^3} \tag{1.2}$$

for D-T fusion, where the variables are density, temperature, and energy confinement time [5]. Reasonable fusion-grade parameters to achieve in a tokamak are $n \sim 10^{20}$ m$^{-3}$, $T \sim 10$ keV, and $\tau_E \sim 5$ s. Note that this temperature is over 100 *million* degrees Celsius!

A substantial portion of the cost for confining plasmas comes from generating the magnetic field.

For fusion energy to be a viable option for generating electrical power, the magnetic field must be used efficiently. A metric for measuring efficiency of using the field is the ratio of the plasma pressure to the magnetic pressure, $\beta$. Three common $\beta$ parameters are [6, 7]

$$\beta_t = \frac{\langle p \rangle}{\langle B_t \rangle^2 / 2\mu_0} \tag{1.3}$$

$$\beta_p = \frac{\langle p \rangle}{\bar{B}_p^2 / 2\mu_0} \tag{1.4}$$

$$\beta_N = \frac{\beta_t}{I_p / aB_t} \tag{1.5}$$

where $\langle p \rangle$ is the volume-averaged plasma pressure, $B_t$ is the toroidal field, $I_p$ is the plasma current, $a$ is the minor radius, and $\bar{B}_p = \mu_0 I_p / 2\pi a\kappa$. The elongation $\kappa$ gives deviation of the poloidal cross-section from being circular, $\kappa = A/\pi a^2$, with $A$ as the area of the cross-section. For fixed magnetic fields, fusion power density scales like $\beta^2$, thus small increases in $\beta$ significantly increase a machine's efficiency. Toroidal $\beta$ values up to $\beta_t \sim 40\%$ have been achieved in a low-aspect ratio tokamak called NSTX [8].

## 1.3 Symmetry in tokamaks

Tokamaks are nominally axisymmetric in the toroidal direction by design. However, small 3D fields will arise in actual machines. When these 3D fields are constant or slowly evolving in time, they are called "error fields." Error fields are caused by finite magnetic field coils and by misalignments of the coils. Even small 3D fields on the order of $\delta B/B_t \sim 10^{-4}$ will cause noticeable effects on plasma performance [9, 10]. Several negative effects include energetic particle losses [11], rotation damping through neoclassical toroidal viscosity [12, 13, 14], and an increase in low-density limits before the onset of locked modes [15, 16]. Thus eliminating 3D fields is generally desirable in tokamaks. A technique called error field correction [17] uses non-axisymmetric coils to cancel out 3D fields as much as possible, where success is inferred from reduction of the negative effects mentioned above.

### 1.3.1 Instabilities and error field amplification

As tokamak discharges approach fusion-grade conditions, magnetohydrodynamic (MHD) instabilities limit plasma performance, preventing access to high-efficiency operation [18]. These instabilities
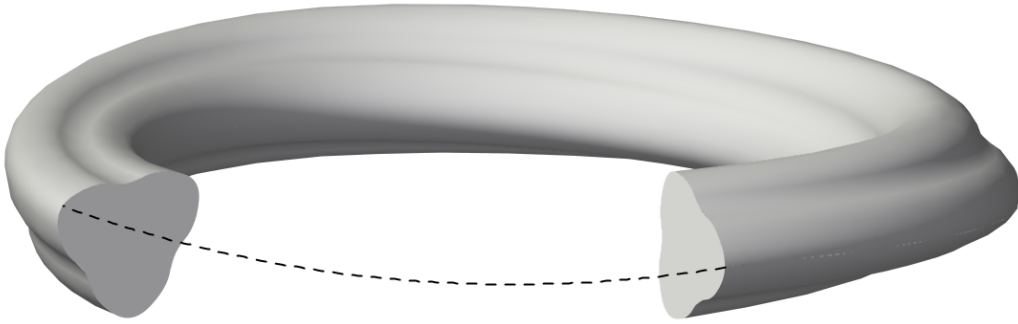
Figure 1.2: Representation of an $m/n = 3/1$ helical distortion from an axisymmetric torus. The surface distortion is exaggerated from realistic perturbation magnitudes.

produce 3D fields, and are commonly referred to as "modes." Highly stable modes pose no problems, as they will damp away quickly when they are driven. Modes that are marginally stable (i.e. almost unstable) can be problematic since they amplify background error fields [19, 20]. This necessitates *dynamic* error field correction [21], as the effective error field changes with plasma conditions. Unstable modes can produce 3D fields that evolve quickly and can terminate discharges if left uncontrolled.

An important instability that limits plasma performance in tokamaks is the external kink mode [22]. This mode causes a helical distortion to the axisymmetric equilibrium, as shown in Figure 1.2. When unstable, the external kink mode grows on an Alfvénic time scale, which is typically microseconds. Pressure and current gradients at the plasma edge drive the kink mode, thus high-pressure machines are inevitably susceptible to the instability. To stabilize the mode, a conducting wall can be placed near the plasma boundary. Eddy-currents in the wall then oppose changing fields from the kinking plasma surface, and prevent growth of the mode. However, this introduces a new instability called the resistive wall mode (RWM) [23, 22], which grows due to decay of the eddy currents. The eddy-current decay rate is set by physical details of the wall, and can be designed to meet the requirements of a given experiment. Typical present-day tokamaks have RWM growth times on the order of milliseconds. This time-scale is slow enough that the mode can be measured and magnetically controlled with existing hardware.

### 1.3.2  Kink Stability Analysis

The stability of the external kink and the RWM can be studied using a perturbed energy analysis with linearized ideal MHD. Here, one considers the change in potential energy ($\delta W$) of the plasma given

a prescribed perturbation. When the total $\delta W$ from all contributions is negative, it is energetically favorable for the instability to grow, releasing potential energy. An appropriate MHD stability analysis was performed by Haney and Freidberg, neglecting inertia, kinetic effects, and the plasma surface component $\delta W_S$ [24]. The resulting growth of the RWM can be written as:

$$\gamma \tau_w^* = -\delta W_\infty / \delta W_b \tag{1.6}$$

where $\gamma$ is the growth rate and $\tau_w^*$ is the resistive diffusion time of the wall. The perturbed energies are calculated with a perfectly conducting wall at a given location ($\delta W_b$) and without a conducting wall ($\delta W_\infty$, i.e. a wall at infinity). Plasma and mode rotation are not included here, but the ideal analysis could be extended to include these.

The perturbed potential energies can be written as

$$\delta W_\infty = \delta W_P + \delta W_V^{(\infty)} \tag{1.7}$$

$$\delta W_b = \delta W_P + \delta W_V^{(b)} \tag{1.8}$$

where

$$\delta W_P = \frac{1}{2} \int_{V_P} \left( \frac{|\delta \vec{B}|^2}{\mu_0} - \vec{\xi} \cdot (\vec{J} \times \delta \vec{B}) + \Gamma p |\nabla \cdot \vec{\xi}|^2 + (\vec{\xi} \cdot \nabla p) \nabla \cdot \vec{\xi} \right) dV \tag{1.9}$$

is the plasma contribution, which is the same with and without the wall, and

$$\delta W_V^{(\infty)} = \frac{1}{2\mu_0} \int_{S_P} (\hat{e}_n \times \delta \vec{A}_\infty) \cdot \hat{e}_n \times (\hat{e}_n \times \nabla \times \delta \vec{A}_\infty) dS \tag{1.10}$$

$$\delta W_V^{(b)} = \frac{1}{2\mu_0} \int_{S_P} (\hat{e}_n \times \delta \vec{A}_b) \cdot \hat{e}_n \times (\hat{e}_n \times \nabla \times \delta \vec{A}_b) dS. \tag{1.11}$$

Here $\vec{\xi}$ is the plasma displacement associated with the RWM, $\delta \vec{A}$ is the perturbed vector potential, and $\hat{e}_n$ is the outward-facing unit normal. Note that Equation 1.10 above can be written as the familiar vacuum energy equation $\delta W_V^{(\infty)} = \frac{1}{2\mu_0} \int_V |\delta \vec{B}_\infty|^2 dV$.

Helical eigenmodes of the form $e^{i(m\theta + n\phi)}$ minimize the perturbed potential, and are taken as the shape of the perturbations with given poloidal ($m$) and toroidal ($n$) mode numbers [5]. When the saftey factor at the edge of a limited plasma ($q_a$) is slightly below a rational value, $q_a \lesssim m/n$, there is significant drive for an RWM with a helicity which resonates with that rational safety factor.

To evaluate which mode numbers may be important for circular cross-section plasmas with a given equilibrium, the cylindrical *kink safety factor*, is defined as [6]

$$q_* \equiv \frac{aB_t(R_0)}{R_0\bar{B}_p} = \frac{2\pi a^2 \kappa B_t(R_0)}{\mu_0 R_0 I_p} \tag{1.12}$$

The vacuum perturbed potentials $\delta W_V$ represent energy from compressing or bending the magnetic field outside the plasma, and are always positive (stabilizing). The plasma contribution may be positive or negative, depending on the pressure and current terms in Equation 1.9. When $\delta W_\infty$ and $\delta W_b$ are both positive, the resistive wall mode is stable with a negative $\gamma\tau_w^*$. When $\delta W_\infty < 0$ and $\delta W_b > 0$, the resistive wall mode is unstable. From Equation 1.6, one can see that the growth rate approaches infinity as $\delta W_b$ approaches zero – this is called the "ideal wall limit." For a fixed wall position, this happens when the $\delta W_P$ term becomes large and negative enough to cancel out $\delta W_V^{(b)}$. When the plasma is above the ideal wall limit, the external kink becomes unstable even with a perfectly conducting wall.

Stability of a given perturbation depends on the poloidal and toroidal mode numbers through the $\delta W$'s. The shapes and $\delta W$'s for the least-stable kink modes can be determined through the perturbed energy analysis above using DCON [25]. Coupling of each mode to the 3D conducting wall can be calculated using the VALEN code [26] in order to determine growth rates.

### 1.3.3 Multimode RWMs

When actively suppressing resistive wall modes in tokamaks with magnetic feedback, only the dominant unstable mode is generally considered, providing *single-mode* feedback. However, when there are two or more unstable modes, or when a mode is near marginal stability, multimode effects may become important [19]. The term *multimode* (or equivalently *non-rigidity*) may be interpreted as applying to several situations:

- The presence of a single *rotating* perturbation of a given fixed shape, which depends on the equilibrium. This can be thought of as a pair of degenerate modes [27] (e.g. sine and cosine) which freely exchange energy. Although this may sound like a loose definition, it can be significant in actual devices. The degeneracy is broken when the system is not axisymmetric, as in the case of a realistic non-uniform conducting wall geometry [28].

- A change in the observed mode shape when magnetic feedback is applied. This implies that the mode has a non-rigid structure, as applied fields deform its shape [29, 30]. Seeing no change in the structure implies that a rigid, single-mode description is sufficient [31].

- A change in observed mode shape when the instability drive (e.g. $\beta$) is increased, other than what would be expected from a single DCON mode. An individual mode's poloidal mode number spectrum will change as $\beta$ changes, which is *not* a multimode effect. The multimode aspect appears if the poloidal mode spectrum from more than one DCON mode is present. For instance, a situation could arise where there is one unstable $n = 1$ mode at a given $\beta$. Then if $\beta$ is increased, there could be a second $n = 1$ mode with a different $m$-spectrum that is marginally stable. If the observed perturbation does not have an $m$-spectrum from only the unstable mode, this would be a multimode observation.

- The presence of multiple independent modes within the overall perturbation, indicated by having independent growth or rotation rates, regardless of the instability drive. Evidence for this could appear as one mode speeding up while another slows down.

Multimode effects are commonly seen in reversed field pinch devices due to the large number of $m = 1$ resonant surfaces [28, 32, 33], and must be taken into account when applying feedback [34]. Single-mode treatments have been mostly successful for feedback systems in tokamaks; however, multimode plasma response to feedback may be responsible for loss of RWM control at high $\beta$ in the NSTX tokamak [35]. A detailed study of the multimode structure of RWMs near the ideal wall limit is necessary to ensure successful control of RWMs in fusion-relevant plasmas. The HBT-EP tokamak is well-suited to perform multimode RWM studies under a variety of plasma and wall conditions.

## 1.4 The HBT-EP Tokamak

The High Beta Tokamak – Extended Pulse (HBT-EP) is a university-scale tokamak designed to study $\beta$-limiting MHD instabilities [36, 37]. Specifications of the device are given in Table 1.1, and a picture is shown in Figure 1.3. The toroidal field is set at 0.33 T for every discharge. An air-core transformer induces plasma current and provides ohmic heating. A fast start-up ($\sim$9 kA in 100 $\mu$s) followed by a current ramp of $\sim$2.5 kA/ms creates strong current gradients near the plasma edge, producing current-driven kink modes.

| HBT-EP Parameters | | |
|---|:---:|---|
| Major radius ($R_0$) | $=$ | 88–96 cm |
| Minor radius ($a$) | $=$ | 11–15 cm |
| Plasma current ($I_p$) | $\lesssim$ | 20 kA |
| Toroidal field on axis ($B_T$) | $=$ | 0.33 T |
| Electron temperature ($T_e$) | $\lesssim$ | 150 eV |
| Electron density ($n_e$) | $=$ | 1–3×$10^{13}$ cm$^{-3}$ |
| Pulse length | $\sim$ | 5–10 ms |

Table 1.1: Typical parameters for HBT-EP plasmas.
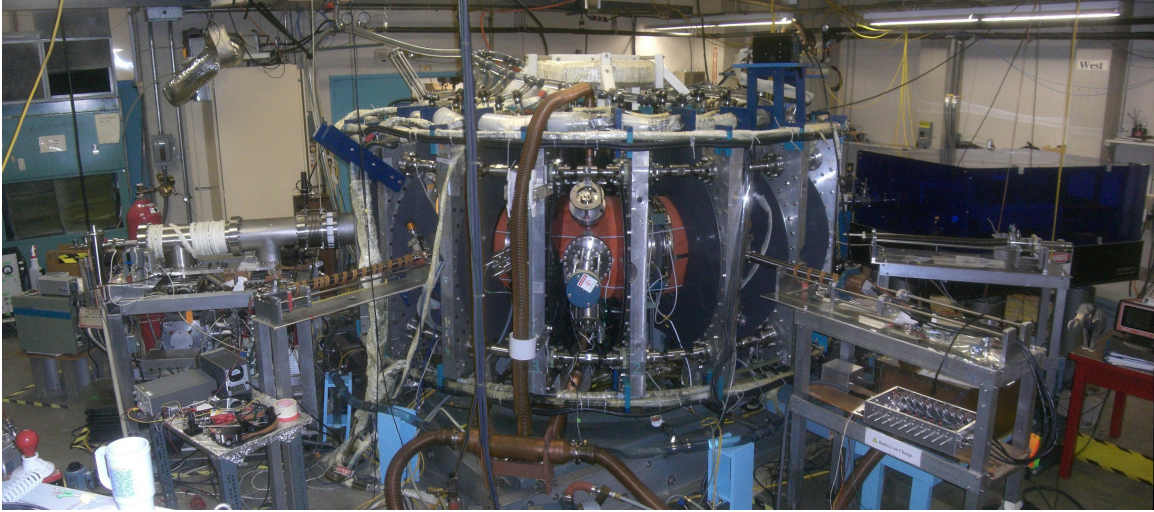


Figure 1.3: Photograph of the HBT-EP device.

The unique adjustable conducting wall in HBT-EP has allowed detailed studies of kink stabilization as a function of the wall geometry [38, 39, 40]. *Passive* kink stability can be studied by moving the wall itself, instead of simply changing the location of the plasma with respect to a fixed wall. HBT-EP has also pioneered the use of *active* magnetic feedback to control the resistive wall mode [41, 42, 43, 44]. Resistive wall modes have been suppressed or enhanced as a function of feedback parameters. Recent experiments have focused on high-resolution MHD spectroscopy using upgraded magnetic sensor and control coil sets [45, 46]. Applied 3D fields have been large enough to induce nonlinear effects including major disruptions and saturation of the resonant plasma response.

HBT-EP plasmas are limited and have a circular cross-section with $\kappa = 1$. A diagram of the plasma and chamber cross-section is shown in Figure 1.4. The major radius is controlled by pre-programming the vertical field evolution to compensate for plasma current and pressure. The minor radius is dictated by limiting surfaces – plasma on flux surfaces outside of the limiting materials quickly free-streams to the walls and neutralizes, setting the plasma boundary. The upper-limit to
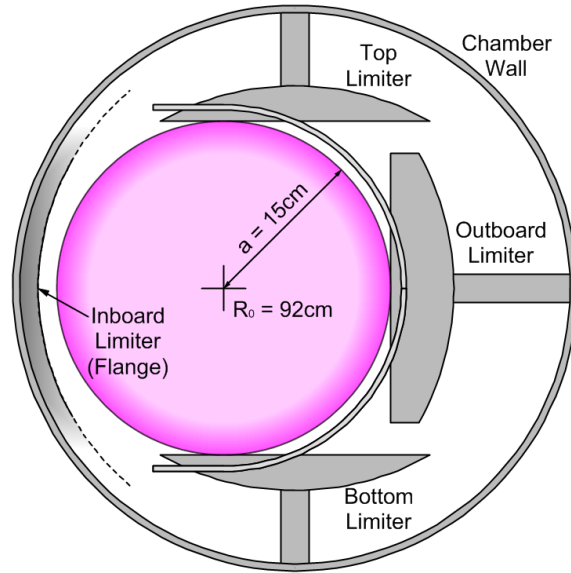
Figure 1.4: HBT-EP cross-section showing an $R_0 = 92\ cm$ plasma, fully-inserted conformal walls, limiters, and the chamber walls. Chamber end-flanges act as the inboard limiters.

the minor radius is 15 cm, as set by the top and bottom limiters in the present configuration. The limiters are movable in the event that larger or smaller plasmas are desired. Diagnostic capabilities of the HBT-EP device along with details of the conducting conformal wall will be given in Chapter 2.

## 1.5   Organization of this thesis

This thesis elucidates multimode behavior of resistive wall modes in tokamak plasmas. Multimode kink effects have been inferred from loss of passive and active RWM stabilization at high $\beta$ [35, 47], but detailed studies of multimode RWM structures of under various plasma and wall conditions have yet to be done. Important questions include:

- Are there certain equilibrium conditions for which multimode effects are more pronounced? If so, are the mode structure differences big enough to cause concern?

- Are secondary modes always present for a given equilibrium, or do they just randomly appear?

- If a port is added to a given machine, changing the conducting boundary, will it make a difference for RWM stabilization?

The remaining chapters of this thesis utilize the HBT-EP tokamak to answer questions like these. Chapter 2 describes the HBT-EP diagnostic capabilities in detail. The recent machine upgrade, which enabled the studies presented in this thesis, is discussed.

Chapter 3 describes an analysis technique known as Biorthogonal Decomposition (BD) that is used throughout the thesis. Simulations are shown which validate the use of this technique for HBT-EP data. This technique was chosen for its flexibility of basis functions and robustness against sensor misalignments, which are important when considering the level of detail necessary for studying multimode effects.

Chapter 4 gives results of using the BD on several individual HBT-EP discharges. Varying mode behavior is observed for plasmas with the same equilibria, motivating a statistical treatment. Analysis of mode structure under differing plasma conditions is done in Chapter 5. The HBT-EP passive stabilizing wall is changed in Chapter 6, leading to different mode behavior. Finally, a summary of important results and implications is given in Chapter 7.

# Chapter 2

# HBT-EP Capabilities

A new segmented conducting wall and diagnostic set was installed in HBT-EP as part of this thesis research [37]. The wall serves for passive stabilization of external kink modes, and is instrumented with control coils for active mode control. This chapter describes the wall and passive diagnostics in HBT-EP.

## 2.1   Conformal walls and diagnostics

HBT-EP plasmas are surrounded by a conformal conducting wall on the low-field-side. The wall consists of 20 wall segments ("shells"), each of which can be individually moved radially outward from the plasma surface.

The shells are made from 3/16" thick 316 stainless steel, spun from flat sheets into a toroidal geometry. The toroidal extent of each shell is $33°$. A little over half of each shell is designed for passive stabilization of ideal external kink and resistive wall modes, while the remaining half acts as a support structure for active control coils. A rendering of a standard shell is shown in Figure 2.1. The region for passive stabilization is continuous except for diagnostic cutouts and mounting holes, and is electroplated with copper on the inside and outside faces. The designed copper thickness was 2.5 mils, but inspection of the copper coating under a microscope revealed that the coating is actually much thicker than nominal on the shells, at $\gtrsim 10$ mils in some places. The coating is also non-uniform, being thicker near the shell edges. The control coil side has "window-frame" cutouts under each coil which allow faster field penetration than for an otherwise solid wall. The entire

shell is electroplated with 0.3 mils of chrome to prevent copper sputtering during standard plasma operations and glow-discharge cleaning. A picture of one of the shells before chrome plating is shown in Figure 2.2.

The shells are nominally conformal to the outboard surface of plasmas having a 15 cm minor radius, centered at a major radius of 92 cm, with a 1 cm gap between the plasma and inner shell surface. The high-field-side shell surfaces are flat for major radii inside of 92 cm, extending radially inward 2.5 inches. The flat portion allows the plasma to move radially inward without scrapping against the shells as it retains the same minor radius. Drawings of the shell cross-sections are shown in Figures 2.3 and 2.4.
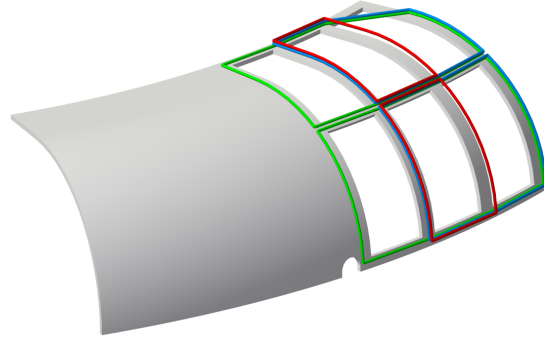


Figure 2.1: Rendering of a standard wall segment. Active control coils are shown in green (large), blue (medium), and red (small). Feedback sensors are on the plasma-facing side, hidden from view.

### 2.1.1   Flexibility of HBT-EP wall configurations

The inner face of each shell normally resides 1 cm from the plasma surface for a plasma centered at a major radius of 92 cm. Armatures that hold the shells in place can be used to move each



Figure 2.2: Picture of an HBT-EP wall segment after copper plating, but before chrome plating. This shell has a large cutout at the top center for an interferometer beam.
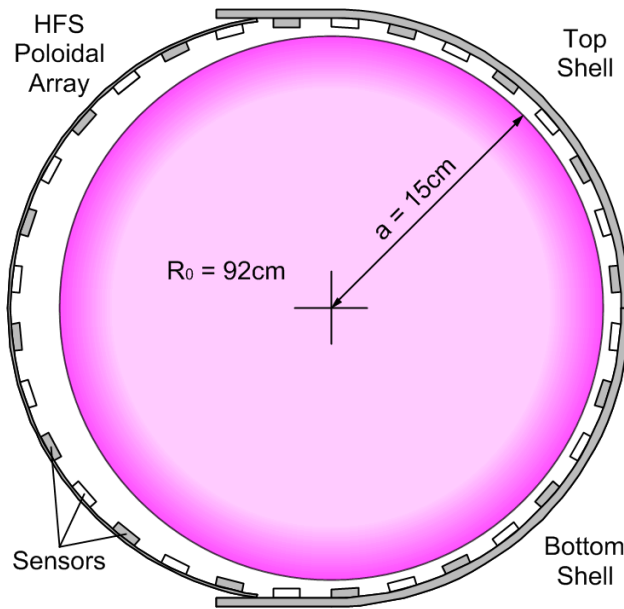
Figure 2.3: Poloidal cross-section of the plasma and shells. The machine centerline is off the left side of the page. The shells were designed to be conformal to a 15 cm plasma center at a major radius of 92 cm. The high-resolution poloidal sensor array layout is also shown, with poloidal sensors as white boxes, and poloidal+radial sensors as filled boxes.
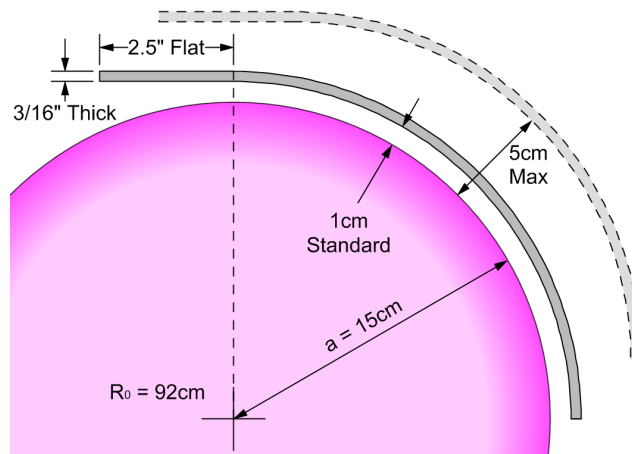


Figure 2.4: Poloidal cross-section of the top shells with dimensions of interest. The standard fully-inserted position of each shell locates its inner face 1 cm from the plasma surface. Individual shells can be retracted up to 5 cm from the surface along a 45° angle, as shown by the dashed shell outline.

shell radially on a shot-to-shot basis. The full range of motion for each shell varies depending on its surrounding chamber segment. All shells move independently and can be retracted to locate the inner surface up to 5 cm from the plasma surface, as shown in Figure 2.4. Non-symmetric wall configurations that were used for this thesis are described in detail in Chapter 6.
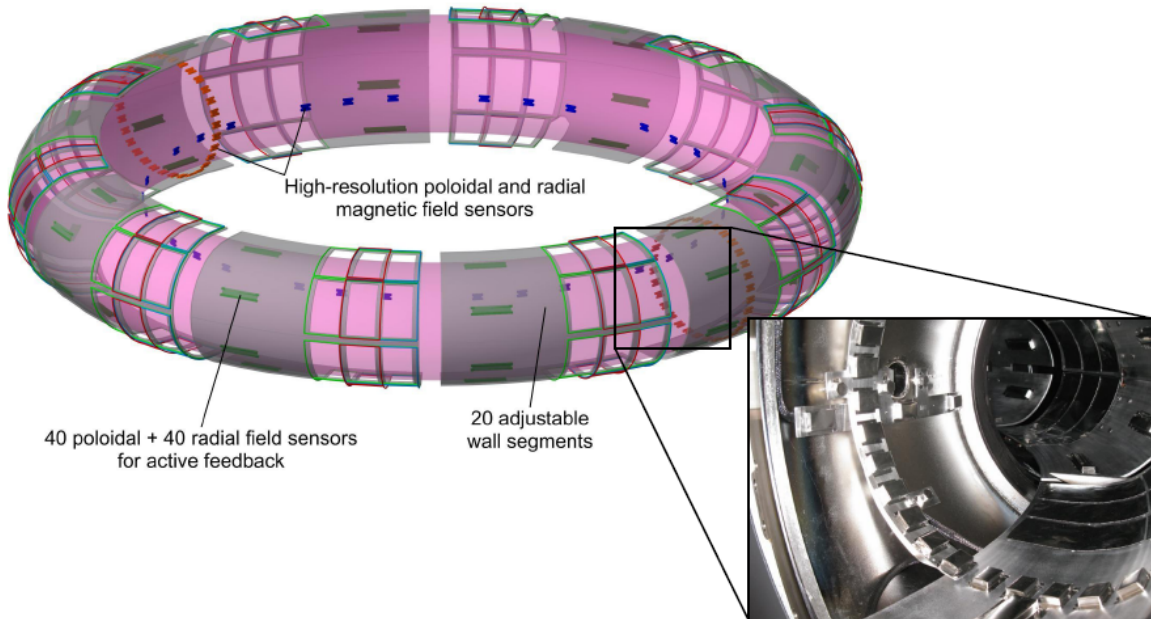
Figure 2.5: HBT-EP's new conducting wall, magnetic sensors, and active control coils. Feedback sensors are shown in green, poloidal array sensors are orange, and toroidal array sensors are blue. The inset shows a picture of sensors and shells as installed in-vessel.

## 2.1.2 Magnetic sensors

A major magnetic diagnostic upgrade was performed as part of this thesis to enable high-resolution, high-sensitivity measurements of magnetic fluctuations from kink modes. Multimode kink structures can now be characterized accurately using the new set of 216 magnetic sensors that were installed close to the plasma surface. Figure 2.5 shows the upgraded sensor set with all shells in their standard fully-inserted positions. All sensors are "pickup" coils, measuring $\partial B/\partial t$ via a voltage induced around a loop of wire due to the changing enclosed flux.

Previous HBT-EP mode studies with active feedback control [43, 44] utilized 20 magnetic feedback sensors that detected poloidal fields. The new feedback (FB) sensor set has 40 poloidal field and 40 radial field sensors (Figure 2.5, green boxes) designed to easily interface with the active control coils described in Section 2.1.4. Radial field sensors allow determination of eddy-current contributions to the poloidal sensors, and allow one to project mode-related $\delta B$ oscillations to the plasma surface using measurements at the wall.

Two new high-resolution "poloidal arrays" (PAs) each measure poloidal fields at 32 locations and radial fields at 16 locations distributed evenly around the poloidal cross-section (Figure 2.5, orange
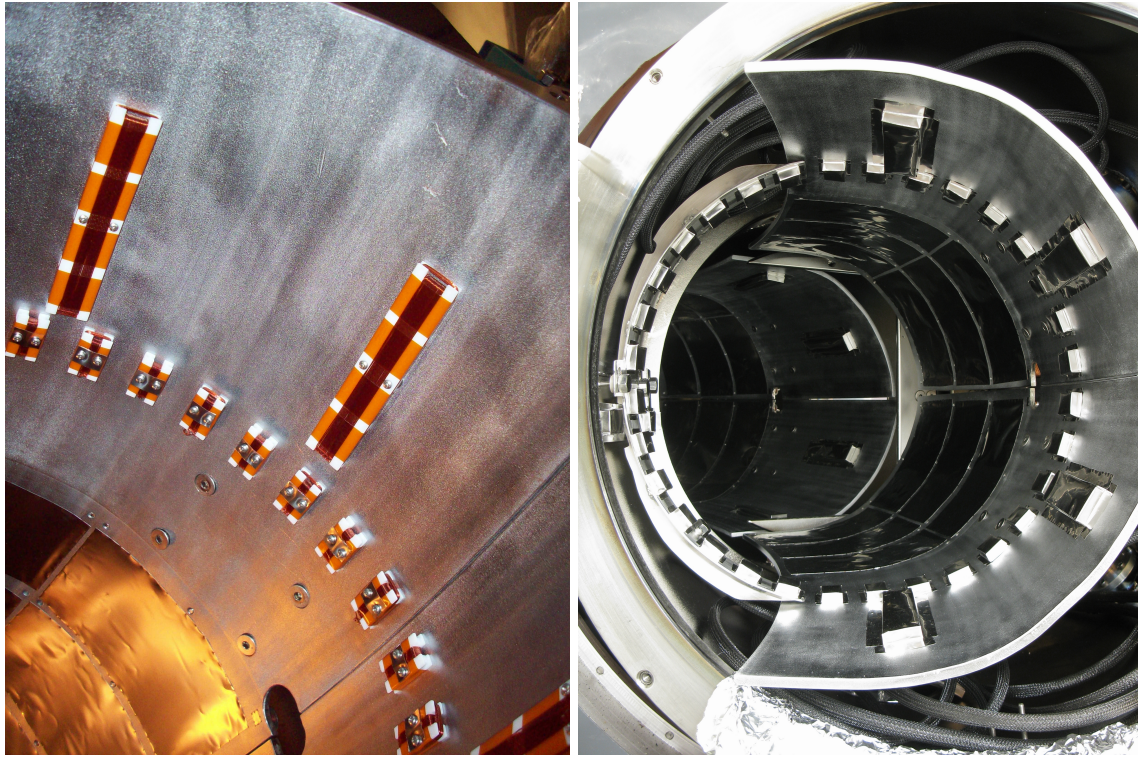
Figure 2.6: Pictures of a high-resolution "poloidal array" (PA) and feedback sensors before and after installing thin stainless steel shields.

boxes). The two arrays are spaced apart toroidally by 180° to give accurate odd versus even toroidal mode number information. Fourteen locations in each array are mounted on a thin stainless steel spine on the high-field-side of the torus, providing reduced eddy-current contribution to signals as well as positions that remain fixed when shells are moved. In contrast, the previous poloidal array only measured fields on the low-field side with shell-mounted sensors, covering a little over 180° of the poloidal cross-section. Pictures of the new poloidal arrays in-vessel before and after installing stainless steel shields are shown in Figure 2.6. The larger feedback sensors are also seen in the pictures.

Another part of the upgrade was the addition of a high-resolution "toroidal array" (TA) on the high-field-side of the plasma. Poloidal fields are measured at 30 locations, while radial fields are measured in 10 locations (Figure 2.5, blue boxes). These sensors are well-separated from the active control coils, providing very low direct coupling for feedback experiments. The 30-point $B_p$ sensor set allows determination of high $n$ numbers when the plasma edge is close to the inboard side of the vessel. Figure 2.7 shows one tenth of the toroidal array, before installing shielding.

| Nominal sensor dimensions | | |
|---|---|---|
| Sensor type | Number of turns | $N \times$ Area |
| Feedback poloidal | 20 | 80.0 cm$^2$ |
| Feedback radial | 10 | 176.8 cm$^2$ |
| High-resolution poloidal | 10 | 8.0 cm$^2$ |
| High-resolution radial | 10 | 28.8 cm$^2$ |

Table 2.1: Nominal dimensions for the magnetic sensors.

**Physical details of sensors**

The magnetic sensors consist of Teflon® forms wound with 10 to 20 turns of wire. Dimensions of the sensitive coil areas are shown in Table 2.1. Actual $N \times A$ values for each sensor were bench-calibrated to better than 1% using a Helmholtz coil before installation. Attaching sensors to their mounts was found to deform the coils enough to change the $N \times A$ by several percent for poloidal field windings. Thus care was taken to tighten screws that hold the sensors in place using the same amount of torque as used for the calibration.

To provide electrostatic and particulate shielding, the sensors are covered by thin stainless steel shim stock. Voltage signals measured by each probe are routed to differential amplifiers, and are partially integrated with an $RC$ time of 200 $\mu$s. Amplifier gain is $\times$10 for the feedback sensors, and $\times$100 for the high-resolution sensors. Full integration is completed in software. Signals are stored using D-TACQ ACQ196CPCI digitizers with 16-bit resolution and a sampling rate of 500 kHz.



Figure 2.7: Picture of the "toroidal array" (TA) and the high-field-side poloidal array in one chamber section before shielding the sensors. Toroidal array sensors are in all 10 chamber sections.

**Processing sensor signals**

The method used for processing magnetic signals is shown in Figure 2.8. First the partially integrated signals (containing a mixture of $B(t)$ and $\partial B/\partial t$) are fully integrated in software to give $B(t)$. Then a smoothed version of $B(t)$ is calculated for each sensor separately, and taken as the equilibrium

1) Measure $\partial_t B_{r,\theta}(t)$ using pickup coils and integrate to get $B_{r,\theta}(t)$

2) Subtract smoothed signal for individual sensors

3) Contour plot sensor groups
   – Shows dominant mode activity

Figure 2.8: Explanation of generating contour plots for magnetic sensor data.

value versus time. Smoothing is done using either boxcar averaging or a polynomial fit to the data, depending on details of the discharge. The equilibrium field is then subtracted from each sensor to determine perturbations to the equilibrium, $\delta B_p$ and $\delta B_r$. All analysis in this thesis uses only the perturbed fields.

Data are contour-plotted by grouping sensors into their respective sets. Figure 2.8 shows a contour plot of one of the poloidal feedback sensor groups. Feedback sensors are grouped in sets of 10, each having the same poloidal location but different toroidal angles. The toroidal array is one set, and each poloidal array is a set. Angular locations of included sensors are denoted by white diamonds in each plot. Diagonal stripes appearing in the contour plots are caused by peaks and troughs of a given perturbation moving past the fixed sensors, indicating rotating mode activity.

## 2.1.3 Shell modifications

Several wall segments are modified from the standard shell to allow diagnostic access. The most-severe modifications are optical cutouts in the Thomson scattering and interferometry sections. In all cases, the modifications are far enough from the magnetic sensors that differing eddy-current patterns should not affect the measurements. Modeling with VALEN confirms that all sensors at a given poloidal location can be considered to have the same eddy-current contributions for the nominal

shell geometries. However, shell-to-shell differences in plated copper thickness do change local eddy-current decay times. This was investigated in Reference [46], and resulted in small modifications to the VALEN model.

### 2.1.4   Active control coils

The window-frame portion of each shell is instrumented with active control coils (see Figures 2.1 and 2.5). These are used to apply non-axisymmetric fields for a variety of experiments. They have been used to impose resonant magnetic perturbations for active MHD spectroscopy [46, 45], and can be used in feedback control of resistive wall modes to suppress deviations from axisymmetry. The coil layout is a $4 \times 10$ grid, matching the feedback sensor grid but shifted toroidally by $18°$. The active coils were not energized for any experiments in this thesis.

### 2.1.5   Other diagnostics

**Flux loops**

There are 7 flux loops for measuring poloidal flux to aid in equilibrium reconstructions. One additional flux loop on the high-field-side of the torus measures loop voltage. The flux loops are $RC$ filtered, while the loop voltage only uses a voltage divider before being digitized. Typical loop voltages in HBT-EP $\sim$100–200 volts during the startup phase, and 5–10 volts during the experimental period.

**Rogowski coils**

Several Rogowski coils are wound around the poloidal cross-section of the HBT-EP vacuum chamber. One Rogowski coil with uniform windings is used to measure the total plasma current. One coil is wound in a $\cos(\theta)$ pattern to measure the horizontal offset of the plasma current centroid in the vacuum vessel, and hence the major radius. The $R_0$ measurement was calibrated using the "copper plasma" technique described in Reference [46], where three in-vessel copper loops acted as toroidal current filaments to measure the $\cos(\theta)$ Rogowski signal versus major radius, after normalizing to the plasma current. The minor radius is determined using the major radius along with limiter positions shown in Figure 1.4, assuming a circular cross-section.

A $\sin(\theta)$ coil measures the vertical position of the plasma, but was not active throughout this
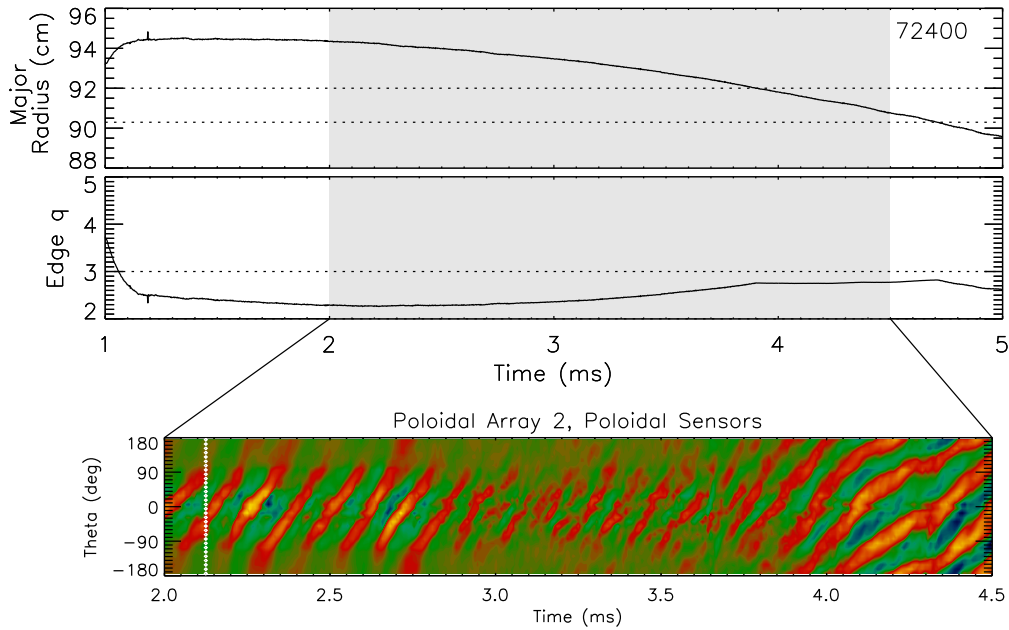
Figure 2.9: Major radius ($R_0$), edge safety factor ($q_*$), and $\delta B_p(\theta)$ fluctuations as seen by one of the poloidal arrays.

research. The remaining Rogowski coils are wound in $\sin(2\theta)$, $\cos(2\theta)$, $\sin(3\theta)$, and $\cos(3\theta)$ patterns in order to measure $m = 2$ and $m = 3$ mode activity. The $m > 1$ coils were used extensively in previous research [29, 43, 40], but are currently only used to get a rough idea of mode activity without looking at the other magnetic sensors.

Plasma current and radius measurements are used together with a probe measuring the toroidal field to determine the helicity of the equilibrium magnetic field at the plasma edge. This quantity, $q_*$ (Equation 1.12), will be used extensively throughout this thesis. The structure of mode activity seen in HBT-EP magnetic sensors is strongly linked to $q_*$. Example measurements showing $m/n = 2/1$ and 3/1 mode activity in one of the poloidal arrays are shown in Figure 2.9.

**Optical emission diagnostics**

Deuterium-$\alpha$ emission from plasma-neutral interactions is measured using a spectrometer viewing a vertical chord through the plasma. A soft x-ray (SXR) detector measures emission from bremsstrahlung, line radiation, and recombination radiation along a horizontal chord 2 cm above the midplane. This detector's signal is heavily polluted with non-optical contributions, however, and is only used for general comparisons across shots. An example of pickup in the SXR detector

is seen during the plasma startup in every discharge – the emission signal dips negative, which is clearly non-physical.

**Thomson scattering**

The HBT-EP Thomson scattering (TS) system is capable of directly measuring the electron temperature and density at a single point in space and time for a given discharge. The beamline was removed from the machine for the duration of this research, preventing usage of the TS system. However, the system was active prior to the HBT-EP upgrade, and measured parameters of similar discharges.

Thomson measurements [48] from a discharge style that was similar to the high-q shots in this thesis are shown in Figure 2.10. Core electron temperature is seen to rise roughly linearly during the shot, reaching nearly 150 eV. Density rises above the Greenwald limit [49], then crashes and produces a corresponding drop in the soft x-ray emission. HBT-EP plasmas routinely operate near the Greenwald limit due to the low plasma current relative to the density. One cause of the density rise throughout the shot is the large difference in plasma volume versus chamber volume – gas fills the large space behind the shells (see Figure 1.4) before startup, then accumulates in the plasma during the shot.
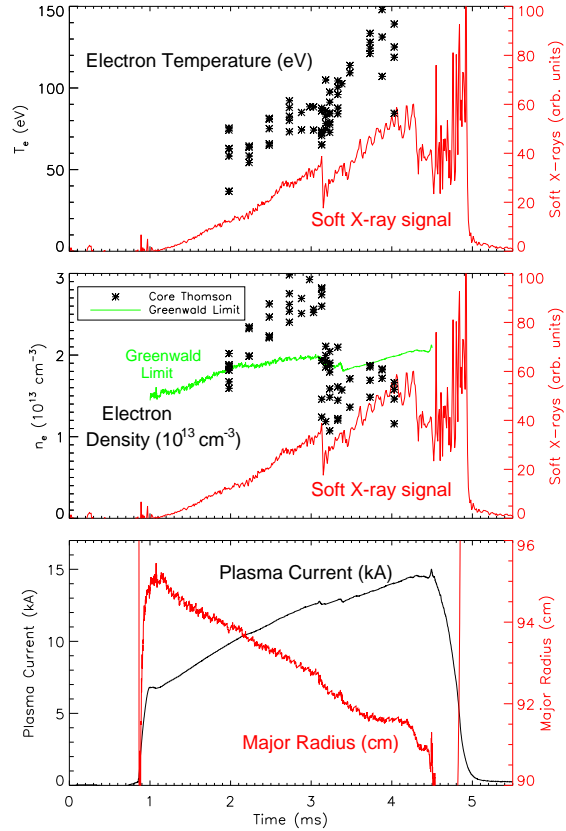


Figure 2.10: Thomson scattering data from a discharge style that was similar to high-q shots in the present research. Each Thomson data point was acquired from a separate, reproducible shot. Electron temperature and density are shown in the top two panels, along with soft x-ray data from one shot. The Greenwald density limit is shown for comparison, though it applies to the volume-averaged density instead of just the core density. Plasma current and major radius are shown in the bottom panel.
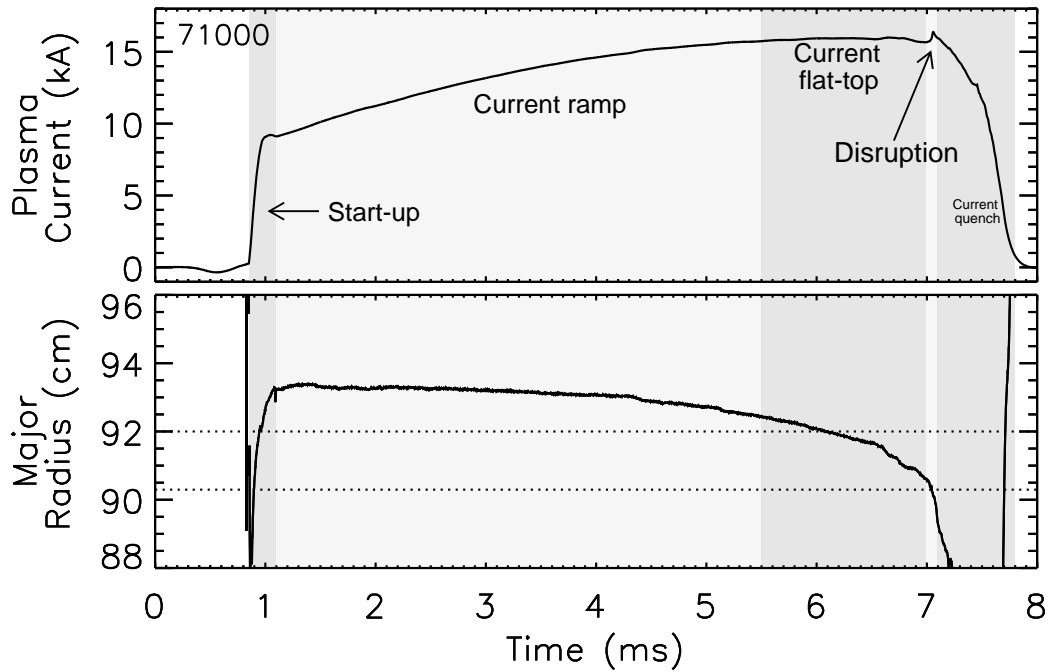
Figure 2.11: Plasma current and major radius for a standard discharge. Various stages of the discharge are labeled.

## 2.2 Discharge pre-programming

All plasmas in this thesis are formed using the technique described in Reference [36], where a fast start-up is followed by a gradual plasma current ramp. The initial plasma current and current ramp are pre-programmed by setting the voltage on two capacitor banks, which are then discharged through the ohmic transformer. Two similar capacitor banks are pre-programmed to create the vertical field, and thus control the plasma's major radius. Plasma current and major radius for a standard discharge are shown in Figure 2.11, along with different stages of the discharge.

All plots of major radius in this thesis show two dotted lines at 92 cm and 90.3 cm. Between these lines, the plasma is limited by the top and bottom limiters (see Figure 1.4), giving a minor radius of 15 cm. Outside of $R_0 = 92$ cm, the plasma is outboard limited, and minor radius decreases with *increasing* major radius. Inside of 90.3 cm, the plasma is inboard limited, and minor radius decreases with *decreasing* major radius. The edge safety factor (Equation 1.12) is established by programming the current and major radius, while considering the large effect from varying minor radii. Note that the outer half of each poloidal array is centered about 92 cm, while the inner half is centered about 90.3 cm.

# Chapter 3

# Biorthogonal Decomposition

This chapter explains the primary analysis technique used in this thesis, known as Biorthogonal Decomposition (BD). Simulations are done to validate its use for HBT-EP data. The effect of coherent noise structures in the data is also explored.

## 3.1 Mathematics of the biorthogonal decomposition

The Biorthogonal Decomposition is mathematically equivalent to Singular Value Decomposition (SVD). A data matrix $S$ is formatted such that time points form the rows and different sensor measurements form the columns. The matrix is then is decomposed into two unitary matrices, $U$ and $V$, and a diagonal matrix of singular values, $\Sigma$, through:

$$S = U\Sigma V^{\dagger} \tag{3.1}$$

with $\vec{u}_i \cdot \vec{u}_j = \delta_i^j$ and $\vec{v}_i \cdot \vec{v}_j = \delta_i^j$. Rows of $V^{\dagger}$ represent the spatial modes, while columns of $U$ represent the temporal modes. Components of the matrices are:

$$
\begin{pmatrix}
\uparrow & \uparrow & & \uparrow \\
s_1 & s_2 & \cdots & s_N \\
\downarrow & \downarrow & & \downarrow
\end{pmatrix}
=
\begin{pmatrix}
\uparrow & \uparrow & & \uparrow \\
u_1 & u_2 & \cdots & u_M \\
\downarrow & \downarrow & & \downarrow
\end{pmatrix}
\begin{pmatrix}
\sigma_1 & & & \\
& \sigma_2 & & \\
& & \ddots & \\
& & & \sigma_N
\end{pmatrix}
\begin{pmatrix}
\leftarrow & v_1 & \longrightarrow \\
\leftarrow & v_2 & \longrightarrow \\
& \vdots & \\
\leftarrow & v_N & \longrightarrow
\end{pmatrix}
\tag{3.2}
$$

with $s_i$ as each sensor signal over time. Temporal modes, singular values, and spatial modes are $\vec{u}_i$, $\sigma_i$, and $\vec{v}_i$ respectively. Here there are $N$ sensors and $M$ time points.

Temporal modes are obtained through the eigenvectors of $SS^\dagger$, while spatial modes are the eigenvectors of $S^\dagger S$. The singular values are square-roots of eigenvalues of either scatter matrix. By convention the singular values are arranged in decreasing order in $\Sigma$, which also orders the associated temporal and spatial modes. Biorthogonal decomposition analysis in this thesis was done using the SVDC command in IDL.

The original data $S$ can be reconstructed through Equation 3.1 after $U$, $\Sigma$, and $V$ are determined. When coherent signals are present, an approximation of $S$ can be reconstructed by using only the first few singular values and modes. The information in $S$ corresponding to a single decomposed mode is reconstructed using the outer product $S_i = \sigma_i \vec{u}_i \otimes \vec{v}_i$.

## 3.2   Interpretation of BD modes

Biorthogonal decomposition can be used for a wide range of applications in measurements of plasma phenomena. It has been used for ion saturation current and floating potential measurements of density fluctuations [50] and edge turbulence [51], and soft x-ray and magnetic measurements of sawteeth and mode activity [52, 53, 54]. The interpretation of BD results will depend on the quantities analyzed.

Biorthogonal modes are a set of orthonormal vectors which can represent the coherent information from the data matrix in a compressed manner. The larger the singular value, the more important that mode is in representing the data set. The fluctuation energy contained in each mode is given by $\sigma_i^2$, yielding the relative energy in each mode [53]:

$$p_i = \sigma_i^2 / \sum_{j=1}^{N} \sigma_j^2. \tag{3.3}$$

For data matrices with coherent structures in space and time, a small number of BD modes can represent the majority of the correlated information.

When $S$ contains fluctuations from traveling waves, the implicit space-time symmetry causes degenerate eigenvalues for the scatter matrices [53]. The resulting degenerate modes are then paired to represent the traveling wave, and can be interpreted as *sine* and *cosine* components forming the

basis for that wave. In the case of a periodic system like the HBT-EP magnetic sensor set, the pairs represent rotating modes.

When a given mode pair $\{\vec{u}, \sigma, \vec{v}\}_a$ and $\{\vec{u}, \sigma, \vec{v}\}_b$ is found that represent a rotating mode, we can define an amplitude analogous to the amplitude of a traveling wave formed by a standard sine/cosine basis:

$$A(t) = \sqrt{2/N} \sqrt{(\sigma_a \vec{u}_a(t))^2 + (\sigma_b \vec{u}_b(t))^2} \tag{3.4}$$

where $N$ is the number of sensors included in the analysis. Since the $\vec{u}_i$ and $\vec{v}_i$ are normalized, including $\sigma_i$'s and the factor $\sqrt{2/N}$ restores the resulting amplitude to the original units of $S$, assuming a Fourier-like mode structure. Likewise, a phase for the mode pair can be defined as

$$\phi(t) = \arctan\left(\frac{\sigma_b \vec{u}_b(t)}{\sigma_a \vec{u}_a(t)}\right) \tag{3.5}$$

where we have assigned

$$\{\vec{u}, \sigma, \vec{v}\}_a \longrightarrow \cos(m\theta + n\phi - \omega t) \qquad \text{and} \qquad \{\vec{u}, \sigma, \vec{v}\}_b \longrightarrow \sin(m\theta + n\phi - \omega t) \tag{3.6}$$

The contribution of the rotating mode to the original sensor signals can be reconstructed using

$$S_{mode} = \sigma_a \vec{u}_a \otimes \vec{v}_a + \sigma_b \vec{u}_b \otimes \vec{v}_b \tag{3.7}$$

This signal gives what the sensors would see if *only* that mode pair was present in the system. Reconstructions shown throughout this thesis will use this method. Examining reconstructed modes is a good way to assign mode pairs when the singular value pairing is not clear from their magnitudes.

## 3.3  Validation of the technique

Using BD for data containing a single, noiseless, constant amplitude, sinusoidal traveling wave can be shown to give spatial and temporal modes that are identical to the discrete Fourier transform of the wave [53], but realistic data are more complicated. In order to validate the use of BD on HBT-EP data, several test analyses were conducted with synthetic data.

A cylindrical plasma was used for these simulations. Two 32-point sensor arrays, separated toroidally by 180°, measure poloidal fields at 2 $\mu$s time intervals around the poloidal cross-section,
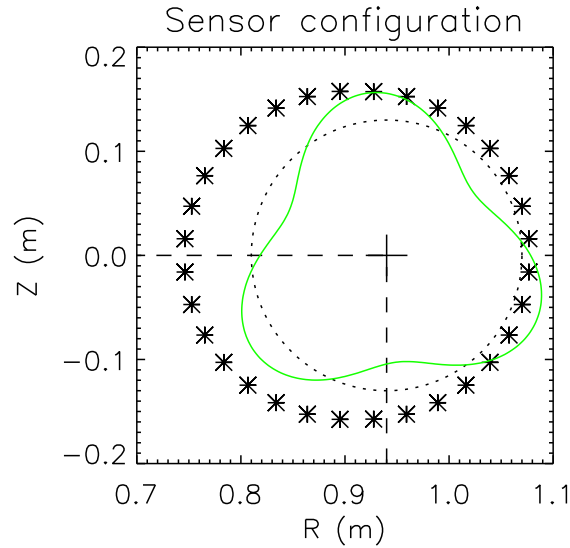
Figure 3.1: Synthetic sensor configuration (stars) used for BD simulations. The plasma shown here is centered at $R_0 = 94\ cm$, with an unperturbed surface given by the dotted line and an exaggerated $m = 3$ mode shown in green.

as shown in Figure 3.1. These model both of the HBT-EP "poloidal arrays" (PAs) used for $m$-number measurements, neglecting eddy-current contributions to signals. Gaussian noise was added to the signals with reasonable amplitude based on what is experimentally measured.

### 3.3.1   Individual well-behaved modes at constant major radius

The BD analysis requires a matrix of data with spatial points versus time. Rather than analyzing the entire available dataset for a given shot, a subset of the temporal data is more appropriate. The assumption of spatiotemporal separability, which justifies using the BD, breaks down if the equilibrium changes too much during the analysis window. The duration of the BD time window can be chosen somewhat arbitrarily, assuming it is long enough for the signal to show spatiotemporal coherence.

Several simple test cases of varying the BD window width were done for individual rotating modes. An example dataset is shown in Figure 3.2, where a simulated $m = 3$ mode rotates at 5 kHz. The BD window width was varied from 20 $\mu$s ($1/10^{th}$ of a period) to 1 ms (5 periods). Figure 3.3 shows the first four singular values versus BD window width. Examining the spatial modes clearly reveals that the 2 dominant modes form a quadrature pair for a rotating $m = 3$ mode. As
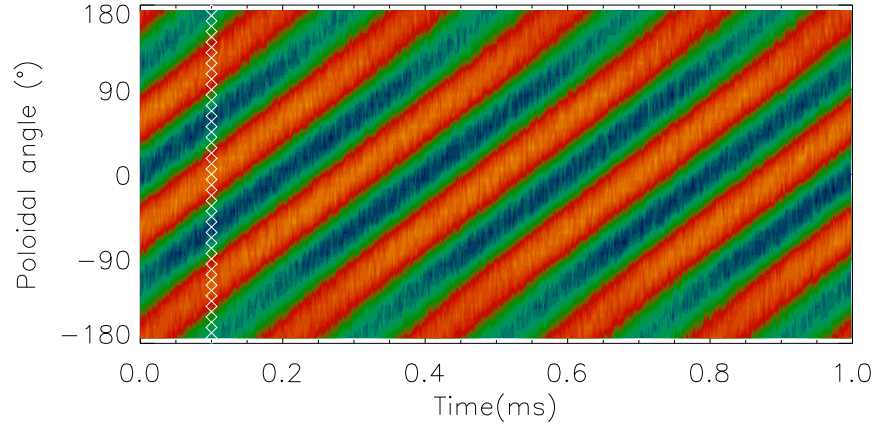
Figure 3.2:  Simulated data for an $m = 3$ mode rotating at 5 kHz, as seen by one of the poloidal arrays. White diamonds represent the sensor angular locations. The mode is centered at $R_0 = 92\ cm$ with a surface amplitude of 6 G. Signals have Gaussian noise with a standard deviation of 0.5 G.
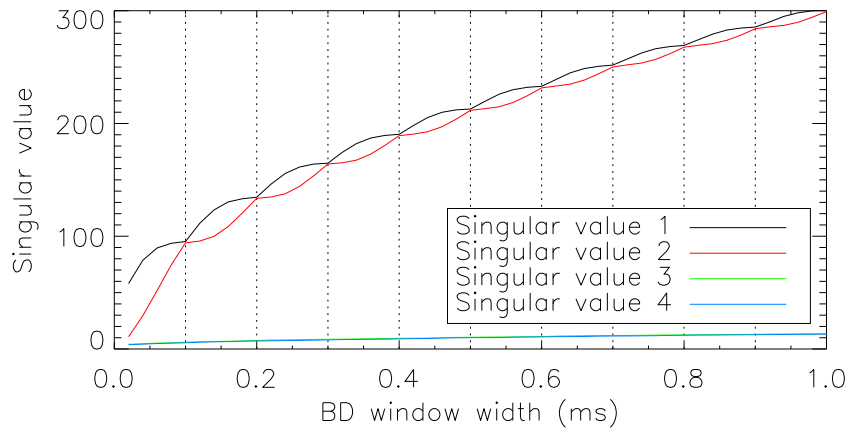


Figure 3.3:  Singular values from analyzing simulated data for one of the poloidal arrays over different time window widths. The first four singular values are plotted. Values 3 and 4 nearly overlap and are in the noise. The vertical dotted lines represent half-periods of the simulated 5 kHz mode.

more periods are represented in the data, the 2 dominant singular values further separate from the noise. Dominant singular value pairs are exactly degenerate when the analyzed data contain an integer number of half-periods for the mode. This happens when the data represent the *sine* and *cosine* phases with equal weight. When the analyzed data doesn't contain an integer number of half-periods, the mode effectively spends more time in either the *sine* or the *cosine* phase, which is reflected in the slight splitting of the singular value pair.
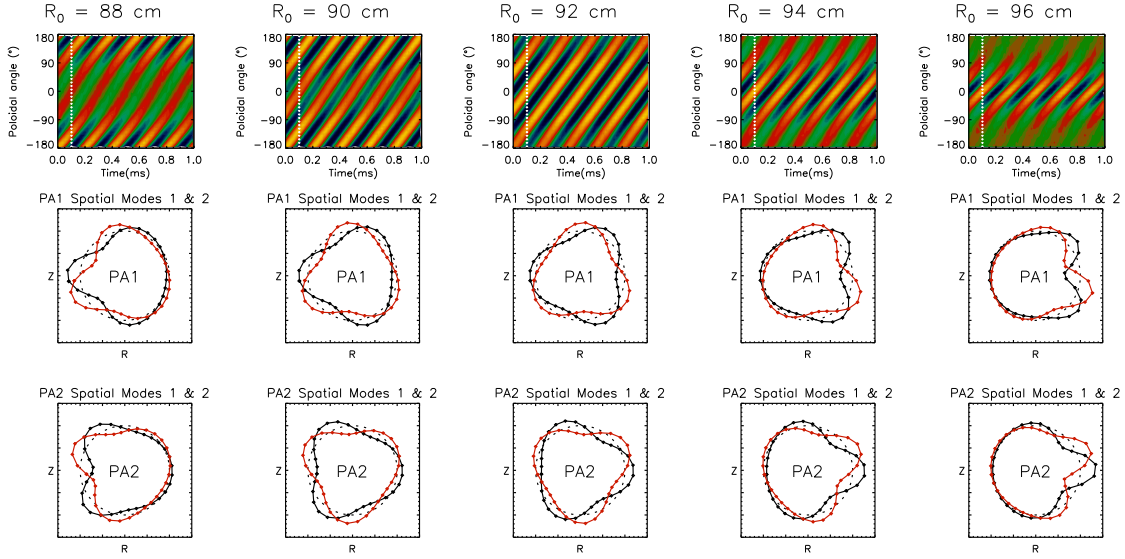
Figure 3.4: Examples of measurements and spatial mode structures for a simulated non-ballooning $m/n = 3/1$ mode. Each column shows results for a given constant major radius, as labeled at the top of each column. Contour plots show the poloidal field measured by the sensors. Black lines represent the *sine* spatial mode, while red lines are the *cosine* mode. Apparent bulging of the mode inward/outward is due to the plasma being closer to the inner/outer sensors. Distortion of the surface in the spatial modes is exaggerated for visualization. Note that the sensor layout was designed for plasmas centered at $R_0 = 92~cm$

One can see that singular values from the dominant mode are clearly paired and well-separated from the noise if there is at least half of a period represented in the data. If the mode amplitude is weaker (or equivalently if there is more noise), the noise floor will be raised in the singular values, thus more periods will be needed to be sampled to unambiguously separate the mode. Running this test with other frequencies or mode numbers gives similar results.

Examples showing the ability of biorthogonal decomposition to determine mode structure without knowing the major radius or a spatial basis beforehand are given in Figures 3.4 and 3.5. Only $m/n = 3/1$ and 6/2 modes are shown, but the results are applicable to any mode number that can be resolved by the sensor set. For each case, only one significant BD mode-pair (*sine* and *cosine* for one rotating plasma mode) is seen. With a Fourier analysis centered at a constant major radius, multiple $m$-numbers would be necessary to represent the full signal. *Odd* versus *even* toroidal mode numbers can easily be inferred by comparing spatial mode structure phases for each poloidal array – *even* toroidal mode numbers look the same in both PAs.
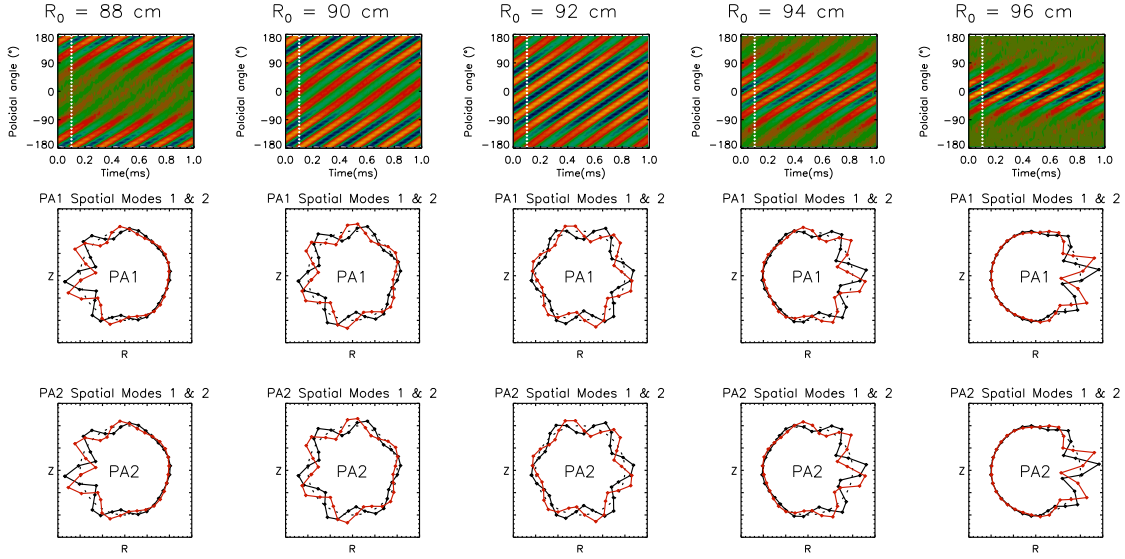
Figure 3.5: Examples of measurements and spatial mode structures for a simulated non-ballooning $m/n = 6/2$ mode. Details of the plots are the same as in Figure 3.4.

## 3.3.2   Multiple modes with growth, decay, and chirping

Individual modes with constant amplitudes and frequencies are well-resolved by the BD analysis, however the effects of mode growth, decay, and frequency-chirping should also be quantified. The example in Figure 3.6 shows a case with a decaying 3/1 mode accompanied by a growing 6/2 mode. The plasma is centered at $R_0 = 92 \; cm$. Initially, a 3/1 mode rotates with a surface amplitude of 6 Gauss. At 0.2 ms, the mode exponentially decays while a 6/2 mode starts to grow. At 0.8 ms, the 6/2 mode stops growing with a surface amplitude of 6 G. Biorthogonal decomposition of the given time window yields the singular values in Fig. 3.6(b). Two clear pairs of singular values are seen well above the noise floor, which is near $\sigma = 6$ (arbitrary units). The four paired spatial modes shown in panels 3.6(c-f) clearly reveal the 3/1 and 6/2 modes. Accompanying temporal modes, amplitudes, and phases are shown in panels 3.6(g-l). The modes' growth and decay are captured without introducing other spurious modes. Initial and final amplitudes are lower than 6 G due to the $\sim 1/r^{m+1}$ field falloff from the plasma edge to the sensors.

Modes in HBT-EP often change rotation frequency during discharges. To show that BD results are well-behaved in this situation, an example is shown in Figure 3.7. The layout of this figure is the same as Figure 3.6. Here a 3/1 mode begins rotating at 4 kHz, then slows to 1 kHz while growing slightly. The mode then decays and speeds up to 10 kHz. The resulting spatial mode structure in

Fig 3.7(c-d) is still intact, and the temporal behavior in 3.7(g-i) matches expectations. Note that the apparent rotation in Fig. 3.7(i) is in the opposite direction as Fig. 3.6(i), though modes seen by the sensors rotate in the same direction. This happens because the assignment of sine versus cosine modes for Equation 3.6 in this analysis is arbitrary. Reconstructions using *both* temporal and spatial modes together show the 3/1 modes propagating in the same direction for each case. The singular values in 3.7(b) show only one significant mode-pair. The second pair of modes is noise, and shows no spatial or temporal coherence.

The previous examples used modes which persist for a large portion of the BD time window. Short bursts of mode activity can also be extracted from the data using the biorthogonal decomposition. Figure 3.8 shows an example with a dominant growing and chirping 3/1 mode. Around 0.6 ms, the 3/1 mode decays briefly and a 6/2 mode appears. The 6/2 mode grows and decays during two revolutions. The 3/1 mode then continues to grow as the 6/2 disappears. Higher-order mode activity is suggested in the raw data of Fig 3.8(a), but its structure and growth may not be completely obvious. Since this mode represents less information in the data than the 3/1 mode (i.e. it's only a transient), its singular values are far smaller.

In each of these cases, the BD-inferred modes represent the simulated data well. Spatial mode structures match the simulated Fourier modes, with reduced fluctuation amplitude for sensors that are farther away from the plasma. The temporal mode pairs reproduce amplitudes and rotation frequencies from the input.

### 3.3.3   Gain variations among sensors

A benefit of the empirical basis derived using biorthogonal decomposition is that modes are not forced to have particular shapes as seen by the sensors. This is especially important when there are non-uniformities in sensor sets, such as variations in gain or misalignments that are not accounted for.

Consider the situation in Figure 3.9. A perfect $n = 1$ sine mode is present at this time, but the sensor at $120°$ has no signal (e.g. from a faulty amplifier). Applying the standard Fourier basis in this situation would lead to a spreading of the spectrum to components other than $n = 1$. However, the BD would assign the "sine" basis as it is seen here, with a zero at $120°$. The difference is absorbed into the spatial mode for that one mode, versus being spread across multiple mode numbers. The same would be true in more subtle cases where a given sensor could be more or less sensitive by
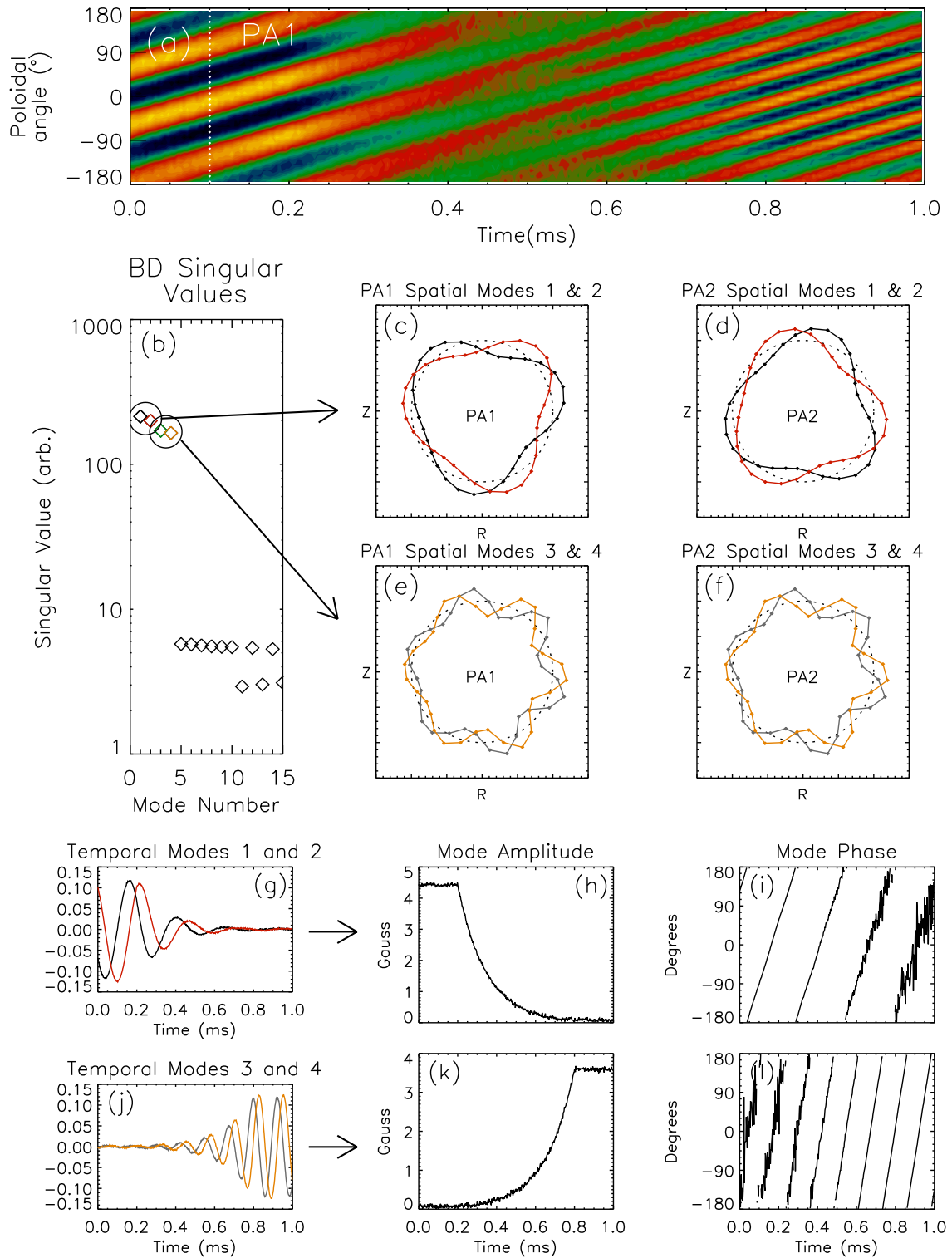
Figure 3.6: Poloidal array measurements (a) and biorthogonal decomposition results (b-l) from analyzing a decaying 3/1 mode accompanied by a growing 6/2 mode, each with a constant frequency. The plasma is centered at $R_0 = 92$ cm.
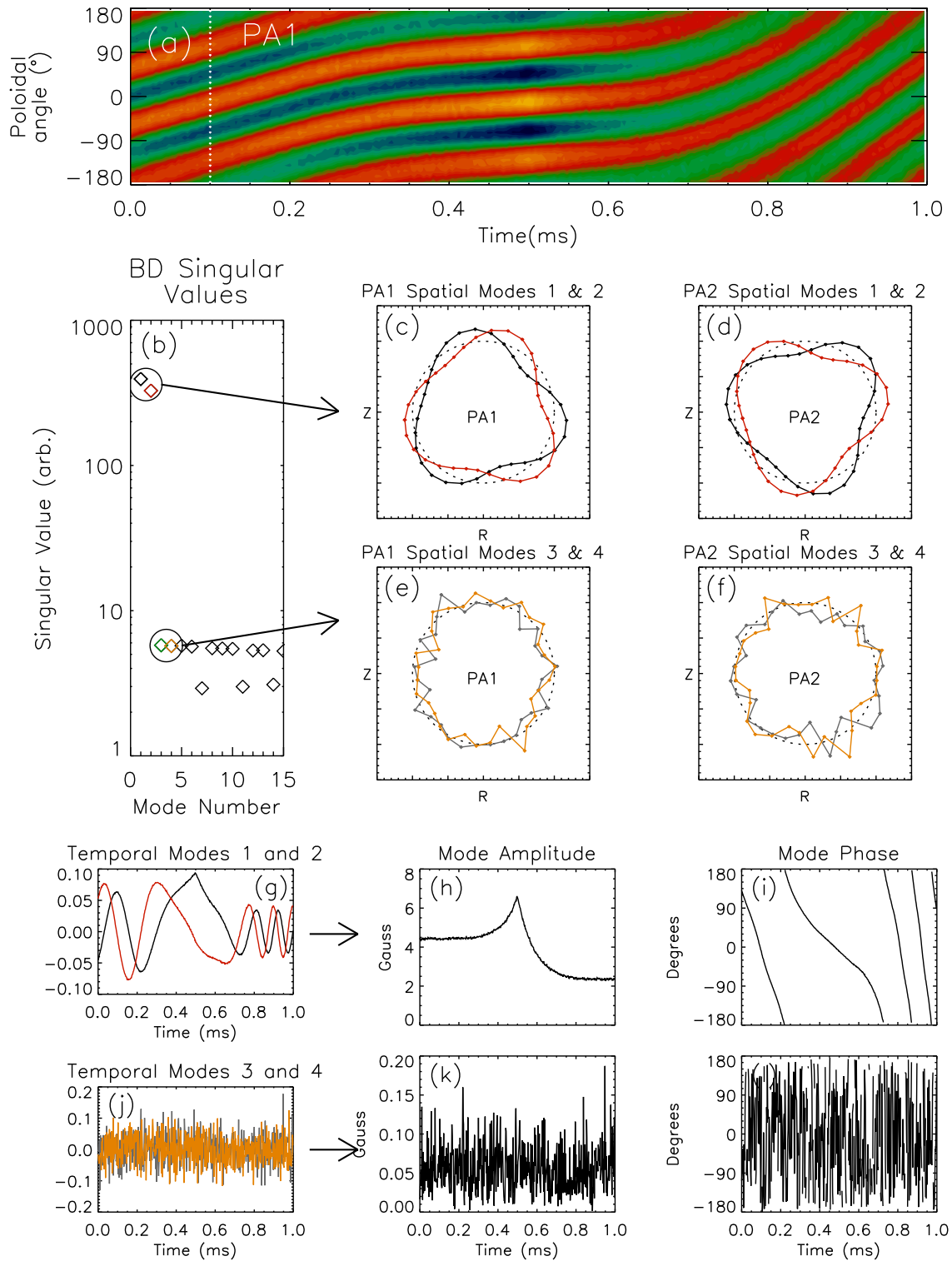
Figure 3.7:  Poloidal array measurements (a) and biorthogonal decomposition results (b-l) from analyzing a chirping 3/1 mode with growth and decay. The plasma is centered at $R_0 = 92$ cm. The second mode pair is noise.
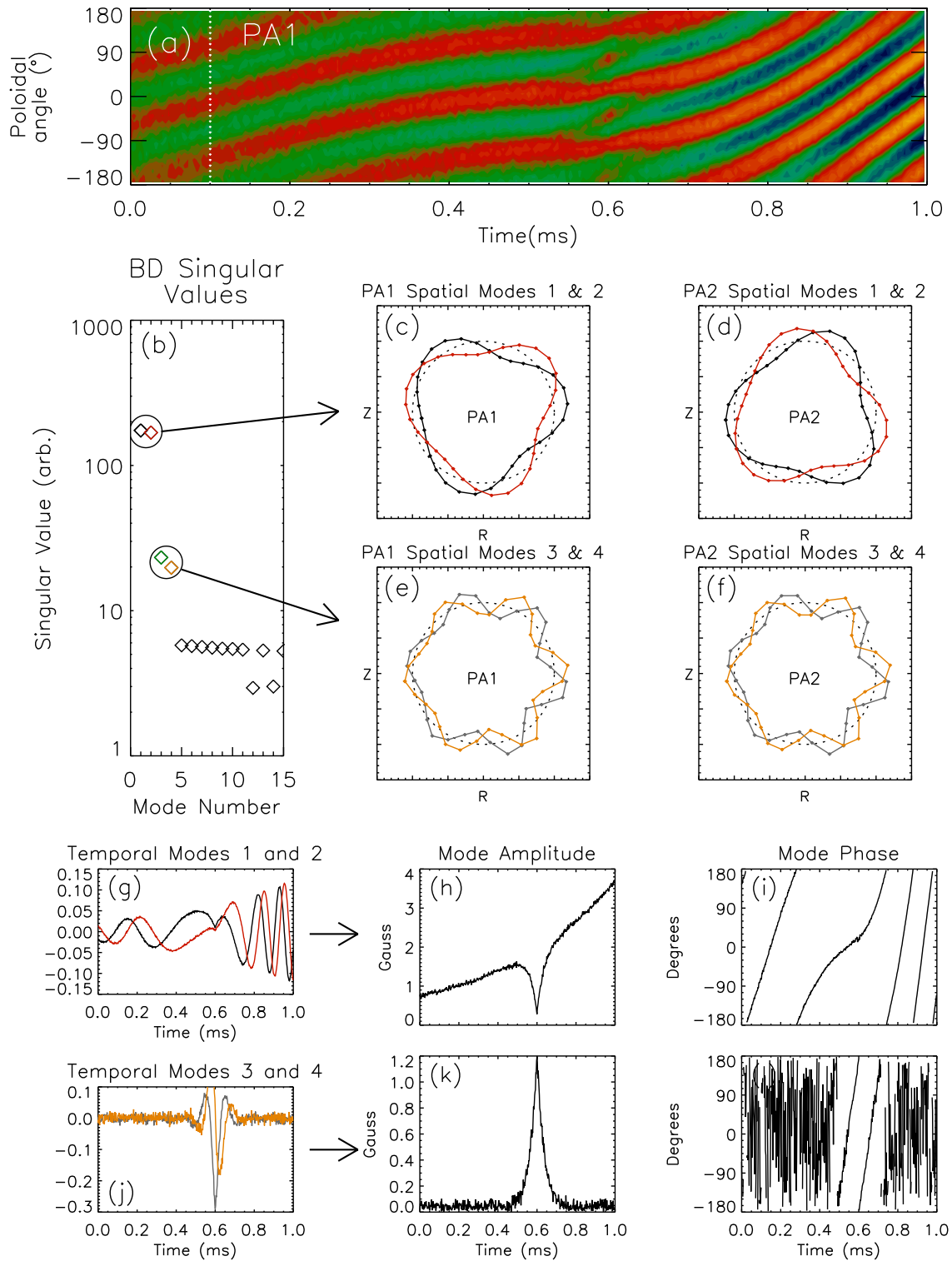
Figure 3.8: Poloidal array measurements (a) and biorthogonal decomposition results (b-l) from analyzing a growing, chirping 3/1 mode. Near 0.6 ms, the 3/1 disappears along with a burst of 6/2 activity. The plasma is centered at $R_0 = 92$ cm.
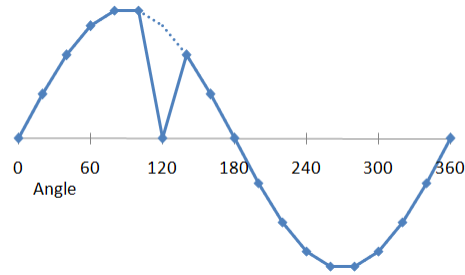
Figure 3.9: Signals seen when measuring a perfect $n = 1$ mode, but with a defective sensor.

several percent, or is misaligned so that it does not pickup the full field signal. If a poloidal field sensor is misaligned and receives some radial signal, this will also be absorbed into the spatial mode, as long as the separate field components evolve in the same way.

### 3.3.4   Changing major radius

As equilibrium parameters change, the utility of using BD analysis on fluctuations is diminished. Benefits of the BD come from the separability of signals in space and time. A non-separable variation, such as a changing major radius, cannot be represented in a single spatial-temporal mode pair, and will influence multiple BD modes [53]. This implies that BD modes will not accurately represent the plasma modes when equilibrium parameters change significantly during the analysis window. The major radius inevitably changes throughout HBT-EP discharges, so its effect on BD modes must be quantified to give confidence in the results.

As an example of how the changing major radius can influence measured BD modes, consider Figure 3.10. Here, a rotating 3/1 mode has a constant surface amplitude of 6 G. The major radius starts at 96 cm, then linearly decreases to 92 cm over 2 ms. The apparent 3/1 mode amplitude increases as the plasma's minor radius grows and the mode gets closer to the sensors, which is to be expected. However, two other BD mode pairs are apparent from the singular values seen in Fig 3.10(b). These modes allow the original sensor data to be more-accurately represented when reconstructed from the decomposed vectors, but they do not represent plasma modes that were originally present. The spatial structure of the first spurious mode pair, seen in Fig 3.10(e-f), looks like a 4/1 mode. The next spurious mode pair is not shown, but its spatial structure is 5/1, and its temporal modes give the same rotation frequency.

The noise floor in the above example was set by Gaussian noise with a standard deviation of
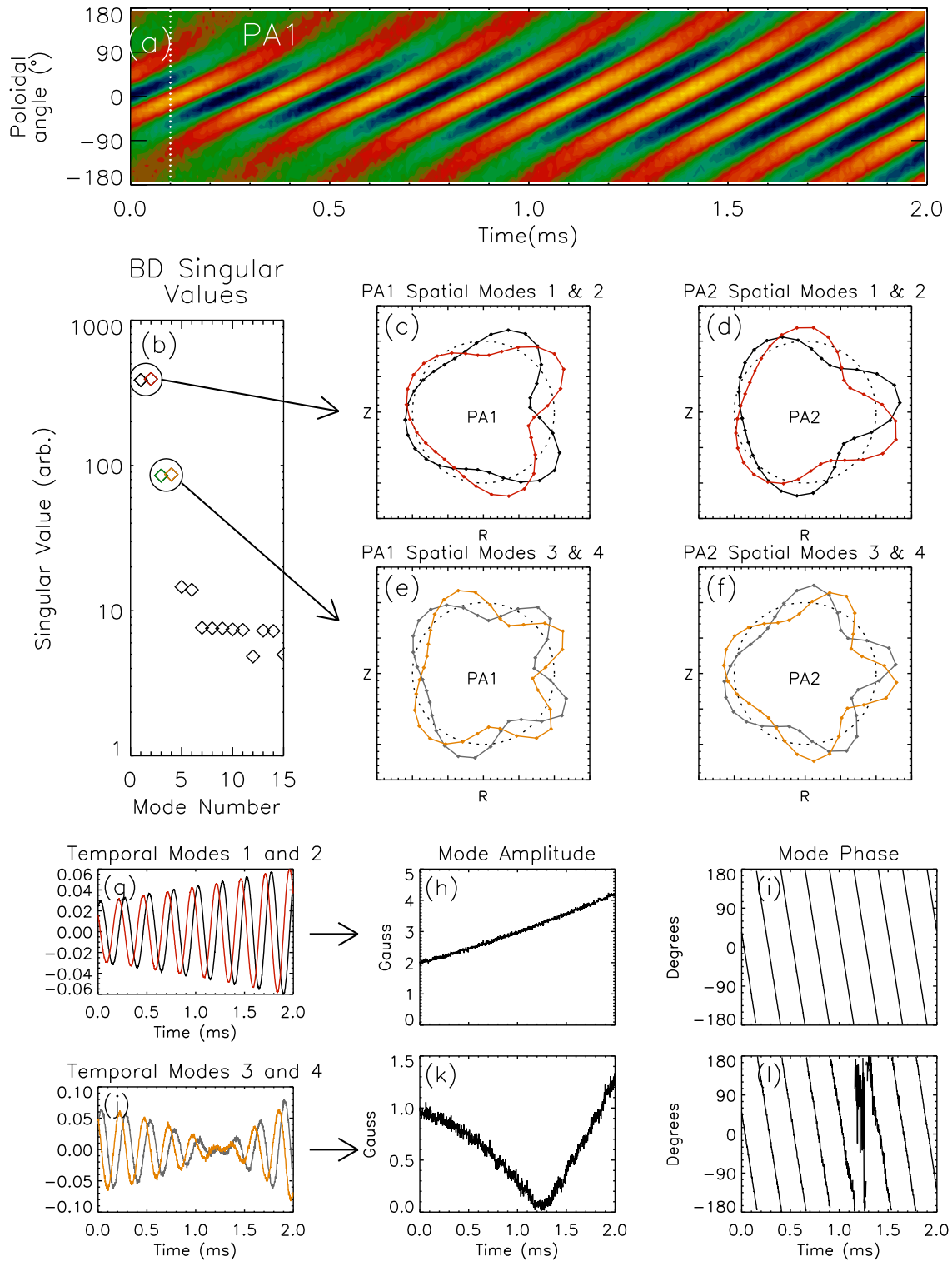
Figure 3.10: Poloidal array measurements (a) and biorthogonal decomposition results (b-l) from analyzing a constant-amplitude 3/1 mode with a changing major radius. The plasma starts at $R_0 = 96$ cm, then moves to $R_0 = 92$ cm at a constant velocity.
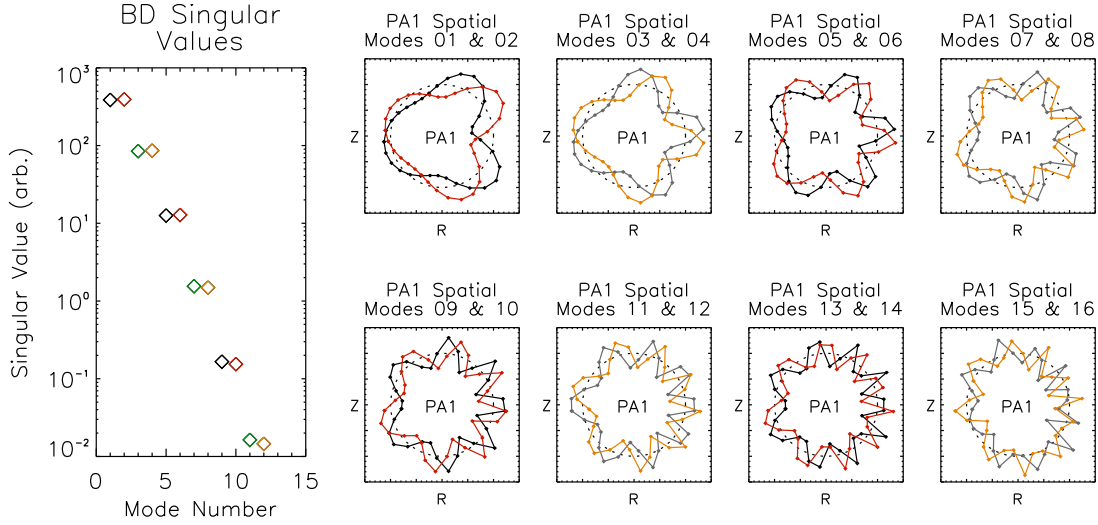
Figure 3.11: Singular values and spatial mode pairs after analyzing data from a pure 3/1 mode with a changing major radius and no sensor noise. The major radius decreases linearly from 96 cm to 92 cm over 2 ms. Many spurious modes at lower amplitude are introduced due to the changing major radius. Extra modes are all $m > 3, n = 1$.

0.2 G. If there's no noise, higher-$m$ mode pairs are seen until the poloidal array can no longer spatially resolve the modes. This is shown in Figure 3.11, where the simulation is the same as Figure 3.10 except without noise. In all cases considered, the resulting spurious modes have $m$-numbers greater than the simulated mode, and have the same $n$-number. For instance, the same analysis with a 6/2 mode will produce spurious 7/2 and 8/2 modes.

The radial excursion simulated in these examples is larger than ordinary variations seen experimentally in HBT-EP. To limit the possible spurious modes that may be seen in real analysis, simulations have been done with typical experimental major radii changes. Figure 3.12 gives the first 7 singular values versus a change in major radius over a 1 ms window for a rotating 3/1 mode with noise. Figure 3.13 uses the same simulation, but with the movement occurring over 0.5 ms and reasonable experimental $R_0$ changes are shown. These simulations apply to plasmas that are outboard limited with $R_0 \geq 92\ cm$, where the minor radius is changing along with $R_0$. Spurious modes also appear when the minor radius does not change with $R_0$ (i.e. when $91.3\ cm < R_0 < 92\ cm$), but are not as strong. The first pair of singular values is a 3/1 mode, and the next two pairs are spurious 4/1 and 5/1 modes when they are above the noise floor. The $7^{th}$ singular value is the noise floor for all major radius changes in this case. BD analysis windows in this thesis have maximum changes in $R_0$ of 1 cm over 0.5 ms, which occurs at the ends of the discharges.
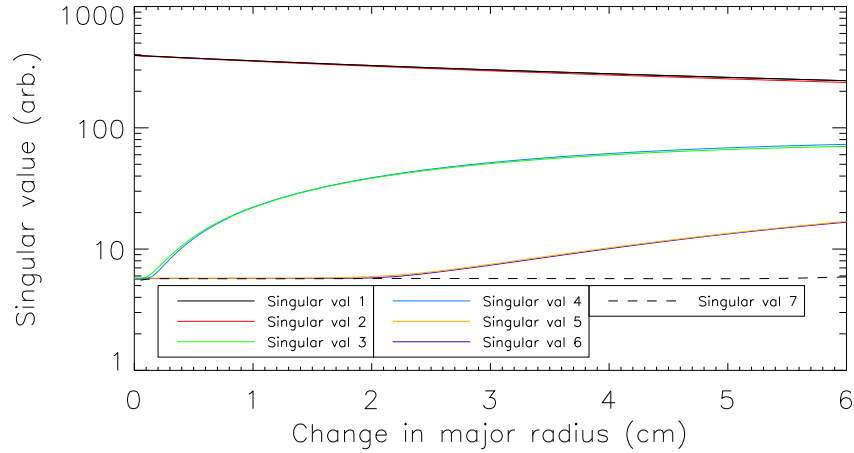
Figure 3.12: Singular values from analyzing a 1 ms time window containing a rotating 3/1 mode and changing $R_0$. The major radius starts larger than 92 cm by the distance given on the x-axis, then decreases to 92 cm over 1 ms. The first pair of singular values represent the simulated 3/1 mode. The $7^{th}$ singular value is the noise floor for all major radius changes in this simulation. When they are above the noise floor, singular values 3 through 6 are spurious modes that appear due to the changing $R_0$.
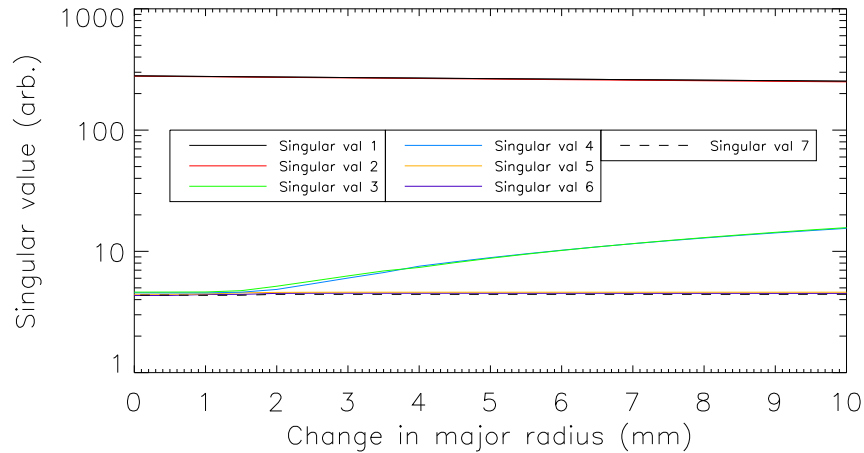


Figure 3.13: Singular values from analyzing a 0.5 ms time window containing a rotating 3/1 mode and changing $R_0$. Plotting details are the same as Figure 3.12. All short analysis intervals in this thesis fall within this range of changing $R_0$.

### 3.3.5    Benefits of biorthogonal decomposition

The above sections have shown several benefits of using the biorthogonal decomposition for HBT-EP data, while outlining its limitations. The BD is robust against errors from misalignments and gain variations among sensors, even when they are not considered in advance. There is no need for an

*a priori* basis assumption, as the BD formulates its own basis from the data. The interpretation of degenerate rotating spatial modes as *sine* and *cosine* pairs forming a traveling wave leads to natural definitions of mode amplitude and phase. Time-varying rotation frequencies and bursts of mode activity are accurately captured in BD modes.

The necessity of using a time window for the BD can be a drawback versus a spatial Fourier analysis, however. Biorthogonal decomposition cannot be done for a single time point, as suggested by its name. To find mode amplitudes at a individual time points, one must do a BD over a time window first, then amplitudes at each time point within that window can be determined.

## 3.4    Effects of coherent noise structures

The noise used in the previous sections was random Gaussian noise, however, there is noise in the HBT-EP magnetic sensors which has a reproducible, coherent structure. Figure 3.14 shows poloidal sensor signals for a background shot with no active equilibrium coils. Feedback sensor groups and half of the high-resolution sensors have $\sim 0.01 - 0.06$ G peak-to-peak noise due to their amplifier
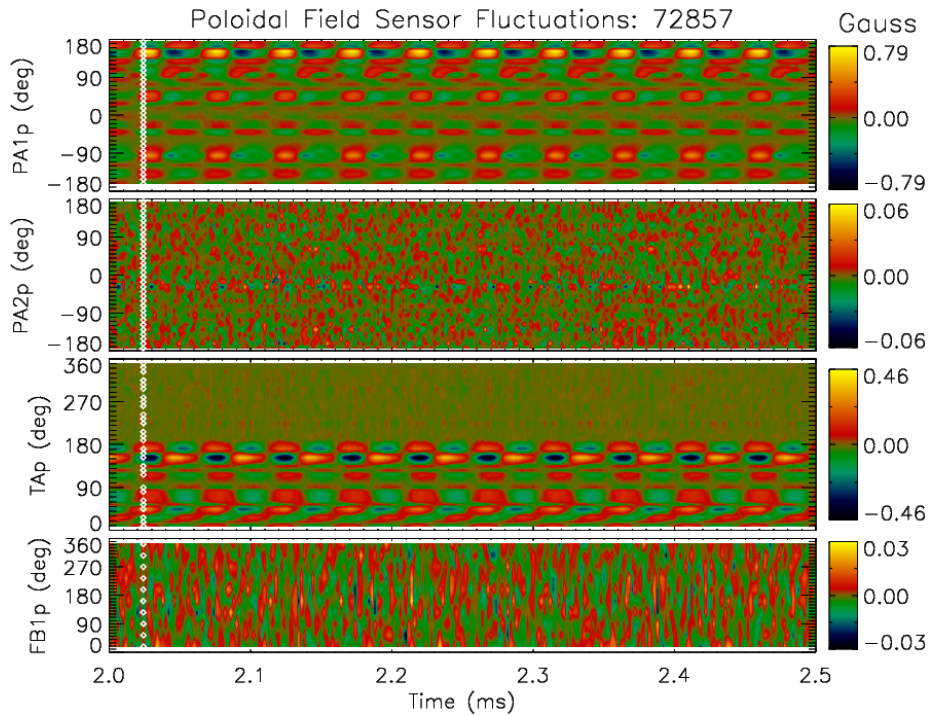


Figure 3.14: Magnetic sensor signals from a background shot with no active coils. Substantial coherent noise is seen in poloidal array #1 and in half of the toroidal array.
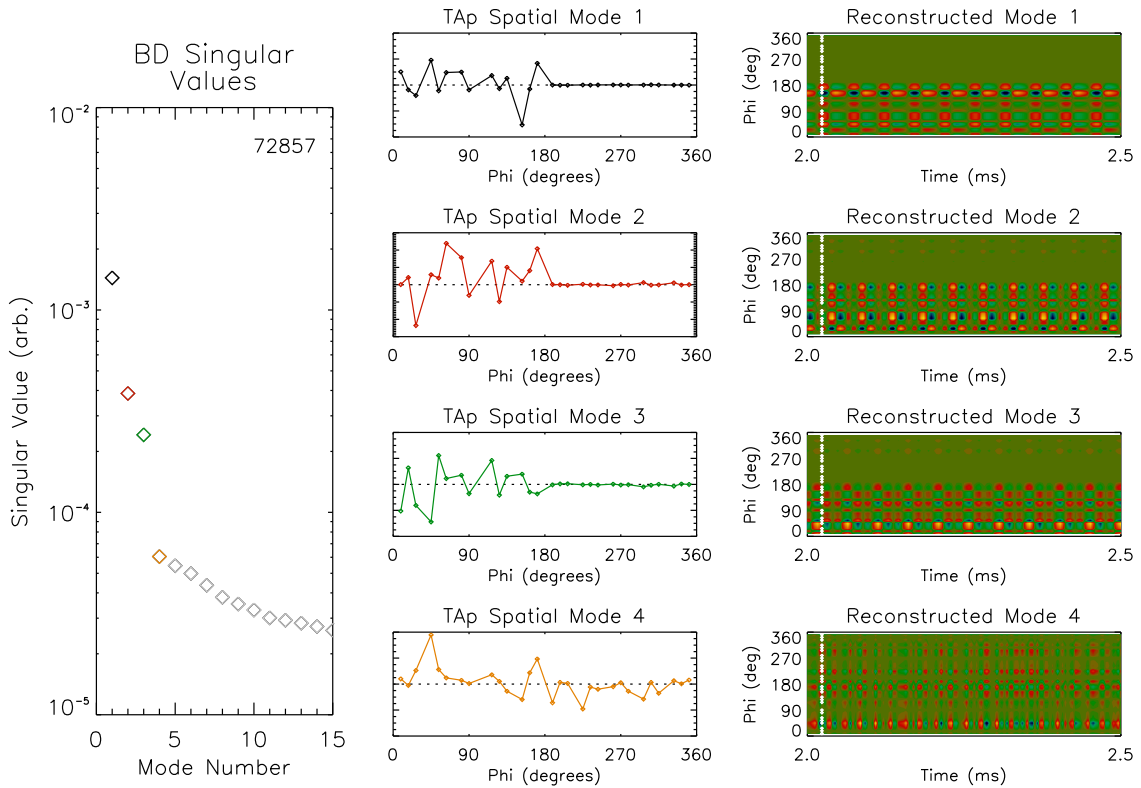
Figure 3.15: Singular values and spatial modes after analyzing the noisy data shown in Figure 3.14 for all working sensors. Spatial modes are plotted using the same color as their respective singular values. Reconstructed modes show the space-time evolution of each individual mode.

circuits. The electronic noise is similar for each sensor set, but differences in collection areas give different effective noise values when signals are converted to field strength. A distinct ~20 kHz signal is seen in all sensors in poloidal array #1, and half of the sensors in the toroidal array. The noisy high-resolution sensors have roughly 10 times the amplitude of the low noise level, but in coherent features. Raw signals from all noisy sensors are $RC$ filtered and amplified through the same amplifier rack, suggesting that this rack is causing the problem.

Since the large noise has a well-defined structure, it is recognized by the biorthogonal decomposition. Decomposing the data in Figure 3.14 gives the modes shown in Figure 3.15. Spatial modes are shown for the toroidal array because they show the problem most clearly. Comparing spatial modes for the noisy half of the TA to the quiet half gives an indication of how many BD modes are significantly affected by the coherent noise. The first three singular values are well-separated from the rest, and account for 98.5% of the total signal energy. These three spatial modes clearly

show more activity in the range of 0–180° due to the coherent noise. The first reconstructed mode looks very similar to the raw data. Note that the singular values here are much lower than in the simulations because the fields are analyzed in Tesla here, whereas they were in Gauss earlier.

Analyzing data during the period before any given discharge begins gives similar results for the first 3 modes. Spatial structures are the same, but the frequency changes. The noise appears between 12 kHz and 20 kHz in discharges that were examined. This frequency range overlaps with frequencies of observed $n > 1$ modes in HBT-EP, which precludes usage of a notch filter to remove the noise.

Since the BD will not separate phenomena with the same frequency, the coherent noise may cause problems in analyzing low-amplitude plasma modes at nearby frequencies. Although this noise may be problematic for analyzing low-amplitude plasma modes, it has not been filtered out for the results in this thesis.

An example case where the coherent noise appears in a plasma BD mode is shown in Figure 3.16. When shot 73009 is analyzed over 3.5–4.0 ms, the first mode pair in the toroidal array is clearly $n = 1$, while the second mode pair (Fig. 3.16(b), one mode from the pair is shown) looks noisy for half of the sensors. The structure in the noisy half looks similar to that of the first noise mode from shot 72857. When the noise mode from shot 72857 is subtracted from spatial mode #3 (part of the second rotating pair) in 73009, the result looks much cleaner than the original mode, and can be identified as $n = 2$ in Fig. 3.16(d). Subtracting this coherent noise automatically and reliably to prevent influence on the actual plasma modes will be a subject of future work.
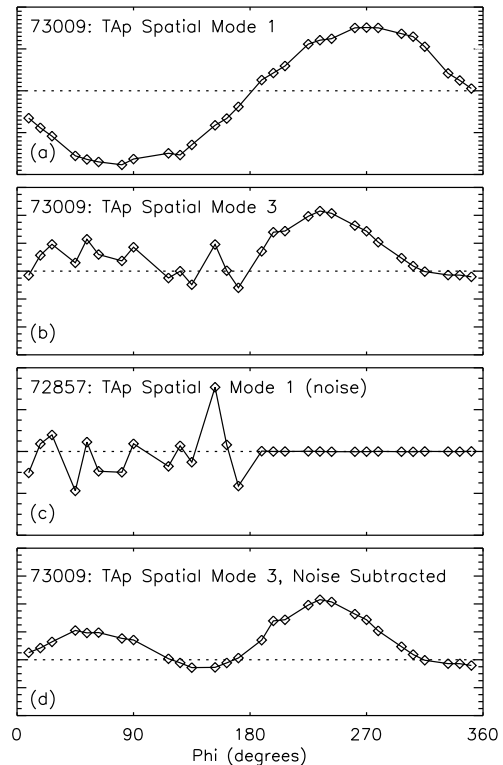


Figure 3.16: Toroidal array spatial modes for shot 73009 (a,b) and 72857 (c). One mode from each rotating pair is shown for 73009. The mode for shot 72857 in panel (c) contains only noise. Subtracting noise in (c) from the mode in (b) gives the result in panel (d).

# Chapter 4

# Multimode Observations in Standard Discharges

This chapter gives extended BD analysis of several individual HBT-EP discharges. Differences that appear when changing the time duration of BD analysis intervals are investigated using experimental data. The $m = 4$ to $m = 3$ transition for an $n = 1$ mode is studied. Non-rigid behavior is seen for 3/1 and 6/2 modes that exist together and accelerate differently. Modulation between 3/1 and 6/2 amplitudes are observed, along with differences in the interactions for two very similar shots, which motivates the statistical treatments in the following chapters.

Modes in HBT-EP are often observed to grow, saturate, and decay without terminating the discharge. The modes do not have simple exponential growth in most cases, even when equilibrium parameters are roughly constant.

## 4.1 Long-duration internal and external modes

Shot 70246 in Figure 4.1 is a standard plasma where $q_*$ crosses 3 from above. The resonant $q = 3$ surface moves from internal to external at around 2.2 ms. Magnetic fluctuations seen by the poloidal and radial field sensors are shown in Figure 4.2. The fluctuations in Figure 4.2 do not appear to show an abrupt change in the dominant $m/n = 3/1$ mode as the resonant surface goes external according to the $q_*$ measurement. The mode does change frequency and amplitude throughout the
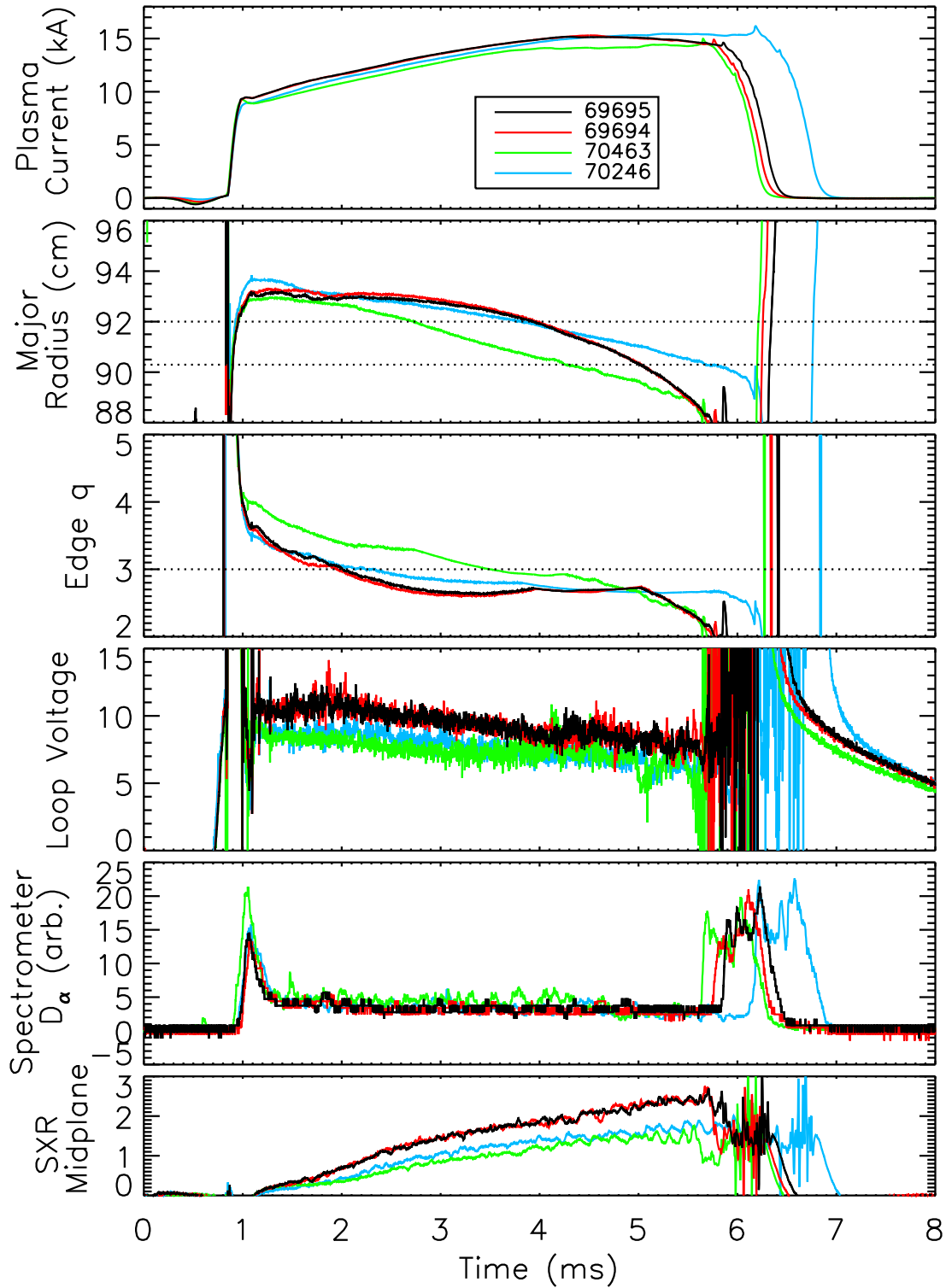
Figure 4.1: Plasma current, major radius, edge $q$, loop voltage, $D_\alpha$ emission, and soft x-ray measurements for the discharges analyzed in this chapter. Measured $D_\alpha$ emission is scaled up by a factor of 4 for shots 69694 and 69695 since the detector was modified around shot 70000.
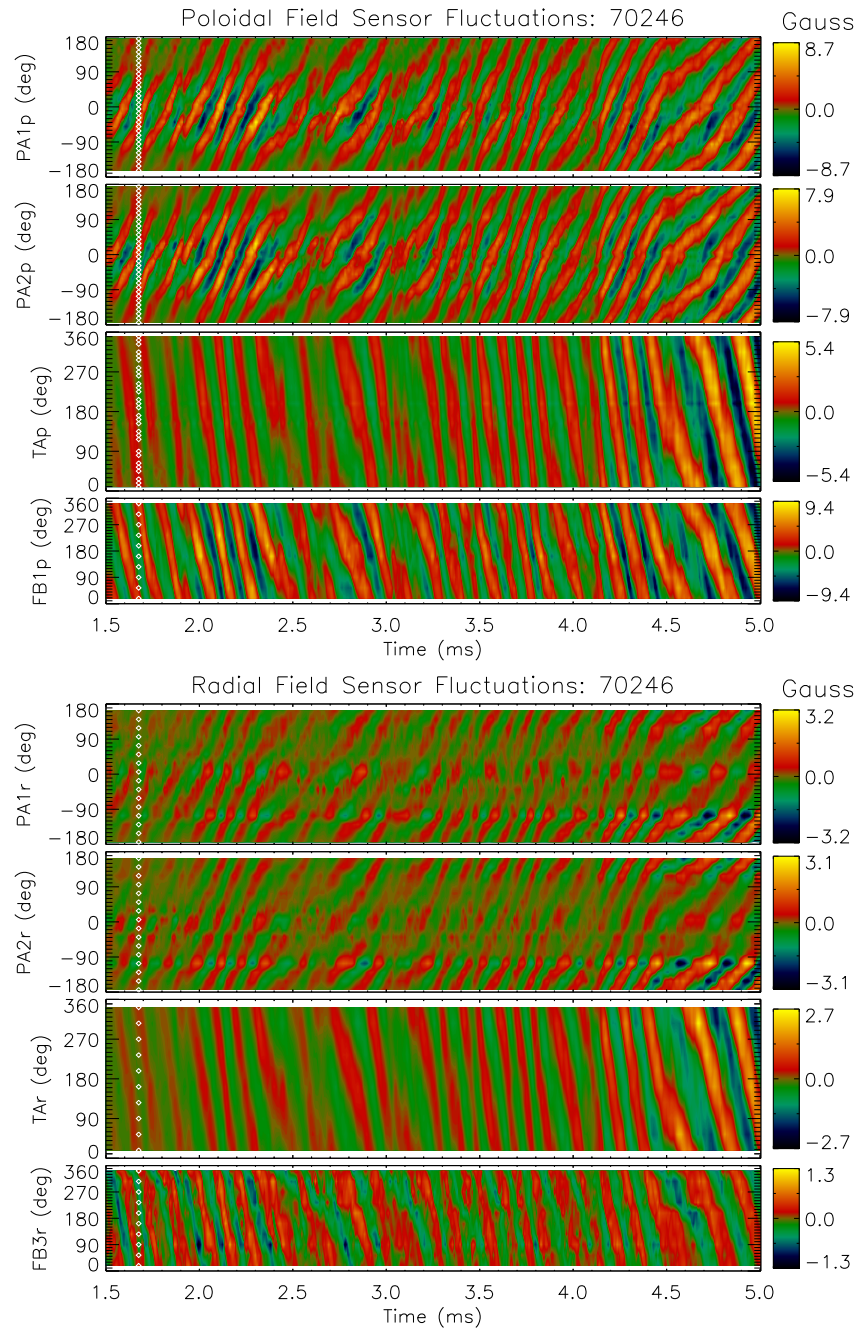
Figure 4.2: Poloidal and radial field fluctuations as seen by magnetic sensors for shot 70246. All working high-resolution sensors are shown, along with 1 of the 4 feedback sensor groups. White diamonds indicate individual sensor locations. Dominant 3/1 mode activity is seen throughout the time shown. The rise in fluctuation amplitude over time as seen by the toroidal array is partly due to the decreasing major radius – the plasma is moving closer to these sensors. Note that dim bands in the center of the poloidal array plots are caused by eddy currents in the shells shielding out radial perturbations.
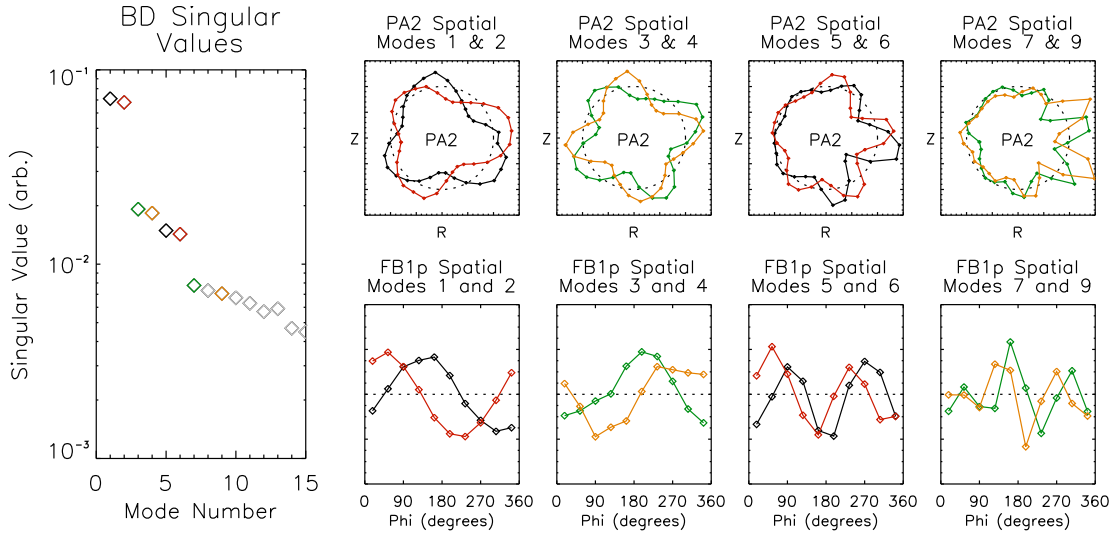
Figure 4.3: Biorthogonal decomposition singular values and spatial modes when analyzing shot 70246 over 1.5–5 ms in one time interval. Poloidal sensors are shown for one poloidal array and one feedback sensor group to give $m$ and $n$ information. Spatial modes are plotted using the same color as their respective singular values. BD mode number 8 is skipped since it is not associated with a quadrature pair.

time shown, but a dependence on the location of the resonant surface is not obvious from this single shot.

Biorthogonal decomposition of all poloidal sensors and radial feedback sensors for the time shown yields the results in Figures 4.3 and 4.4. The first two spatial mode pairs appear to be 3/1 and 4/1. The third pair is a 5/2 or 6/2 mode, and the fourth pair is $n = 3$ with an indeterminate $m$ between 7 and 9. These four modes pairs represent 85%, 6%, 4%, and 1% of the total fluctuation power in the magnetic sensors over the time window shown. The last 4% is in the total of the remaining 155 BD modes. Note that the singular values are much lower here than in the simulations of Chapter 3 because fields are analyzed in Tesla here, whereas they were in Gauss for the simulations.

Figure 4.1 shows that the major radius changes by ∼2.5 cm during the BD analysis window for this shot. Based on the simulation results of Section 3.3.4, the apparent 4/1 mode may actually be an artifact of using a long time window with a changing major radius. This mode has the characteristic spurious features of being the next-higher poloidal mode number relative to the dominant mode, and its amplitude trend in Figure 4.4(b) is similar to Figure 3.10(k).

To reduce effects of the $R_0$ translation, the time range of interest can be broken down into subsets, in which case a spurious 4/1 mode could be removed. Figure 4.4(b) shows that the 4/1
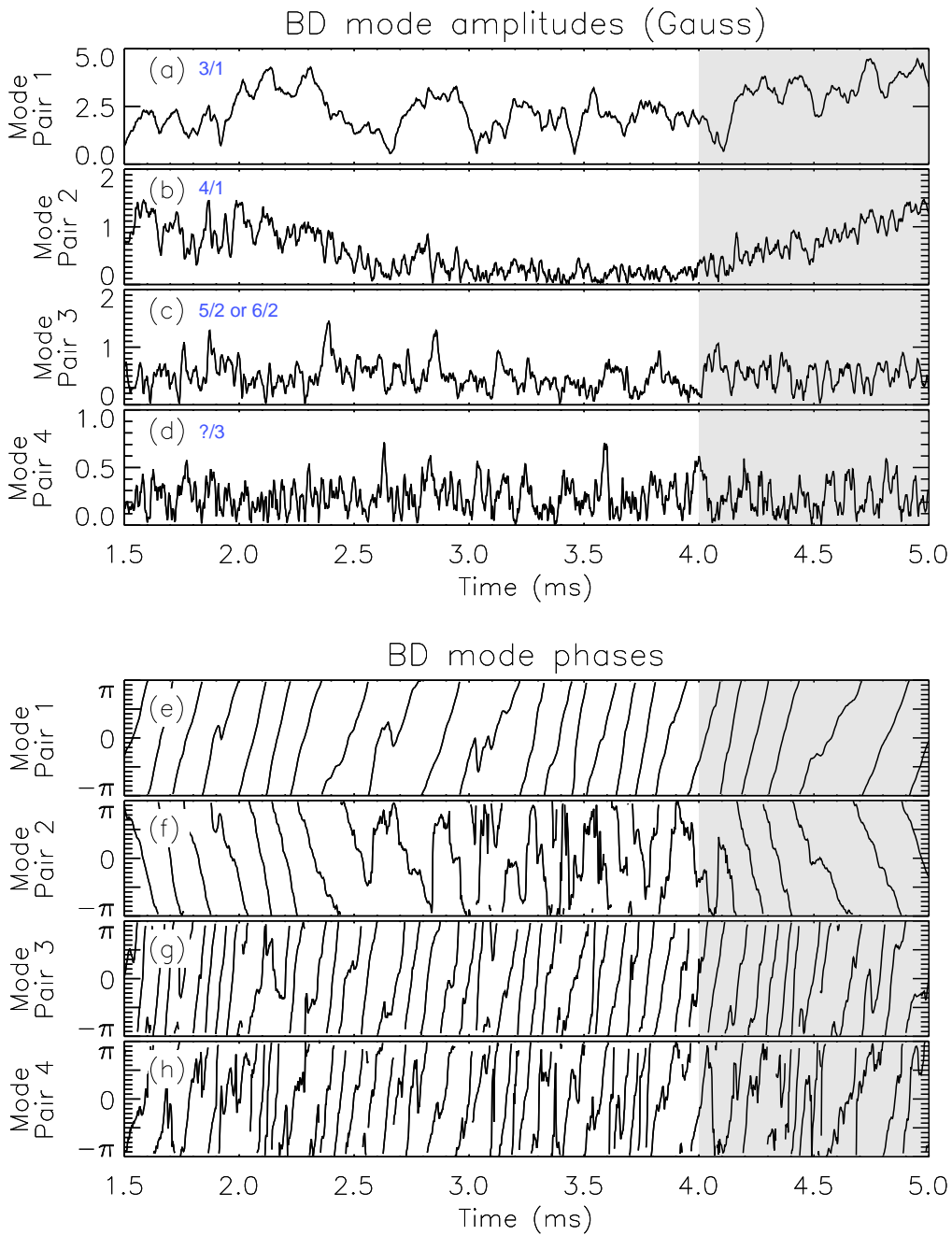
Figure 4.4: Amplitudes and phases for the modes shown in Figure 4.3.  Phases evolve smoothly when the amplitudes are non-negligible.  The reversed phase velocity of mode pair 2 is due to the arbitrary assignment of the *sine* and *cosine* modes, as discussed in Section 3.3.2 – they are swapped in this case.
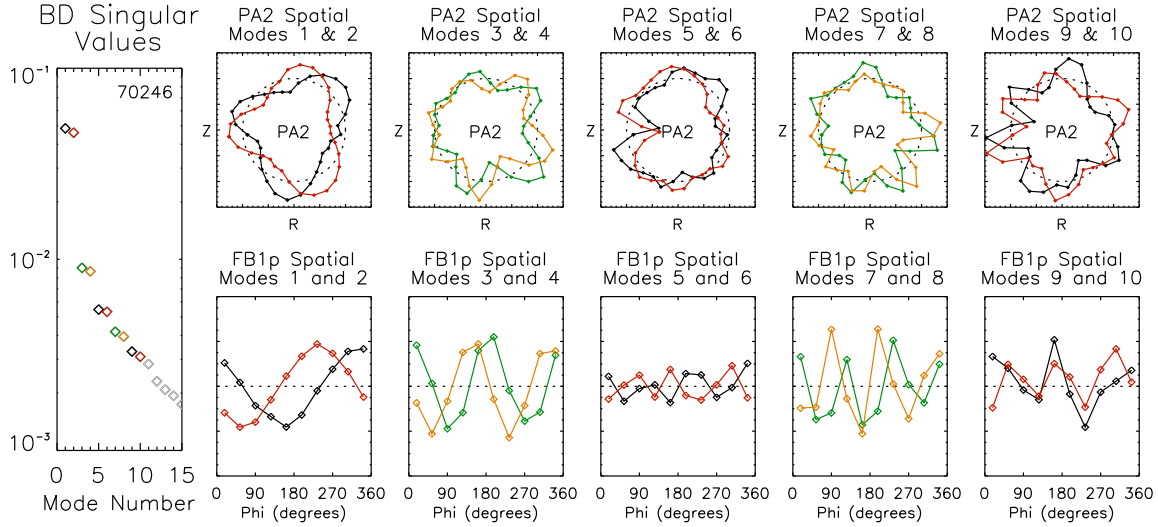
Figure 4.5: Biorthogonal decomposition singular values and five spatial mode pairs when analyzing shot 70246 over 4–5 ms in one time interval. Poloidal sensors are shown for one poloidal array and one feedback sensor group to give $m$ and $n$ information. Spatial modes are plotted using the same color as their respective singular values.

mode is significant during 4.5–5.0 ms when using the long time window. If only the 4.0–5.0 ms window is analyzed separately for the same data, the resulting BD modes are shown in Figures 4.5 and 4.6. No clear 4/1 mode is present, at least not at the amplitude found using the wide analysis window. Based on the $q_*$ measurement, there is no reason to expect a 4/1 mode leading up to 5.0 ms. This demonstrates the importance of selecting an appropriate time interval for the BD analysis, as simulated in Section 3.3.4 with a changing major radius. Analyzing the 1.5–2.5 ms window also doesn't produce a clear 4/1 mode, though there are signs of it in the $5^{th}$, $6^{th}$, and $7^{th}$ BD spatial modes. Standard spatial Fourier analysis would not have this spurious mode problem when major radius is considered.

The two dominant modes in Figure 4.5 are clearly 3/1 and 6/2, accounting for 93% and 3% of the fluctuation power in the 4–5 ms time interval, respectively. There is still evidence of $n = 3$ activity in higher-order BD modes. With this narrower time window, the possibility of spurious modes appearing significant is much less likely. Figure 4.6 shows that the 6/2 amplitude and rotation do not simply track the 3/1 mode; the 6/2 can grow and rotate independent of the 3/1. If the entire mode structure acted as a rigid body, the $n = 2$ mode would rotate at twice the frequency of the $n = 1$ mode. However, the 6/2 mode is observed to speed up while the 3/1 slows down during 4.0–4.4 ms. *This is clear evidence for non-rigid mode behavior.* Further evidence of non-rigid, multimode
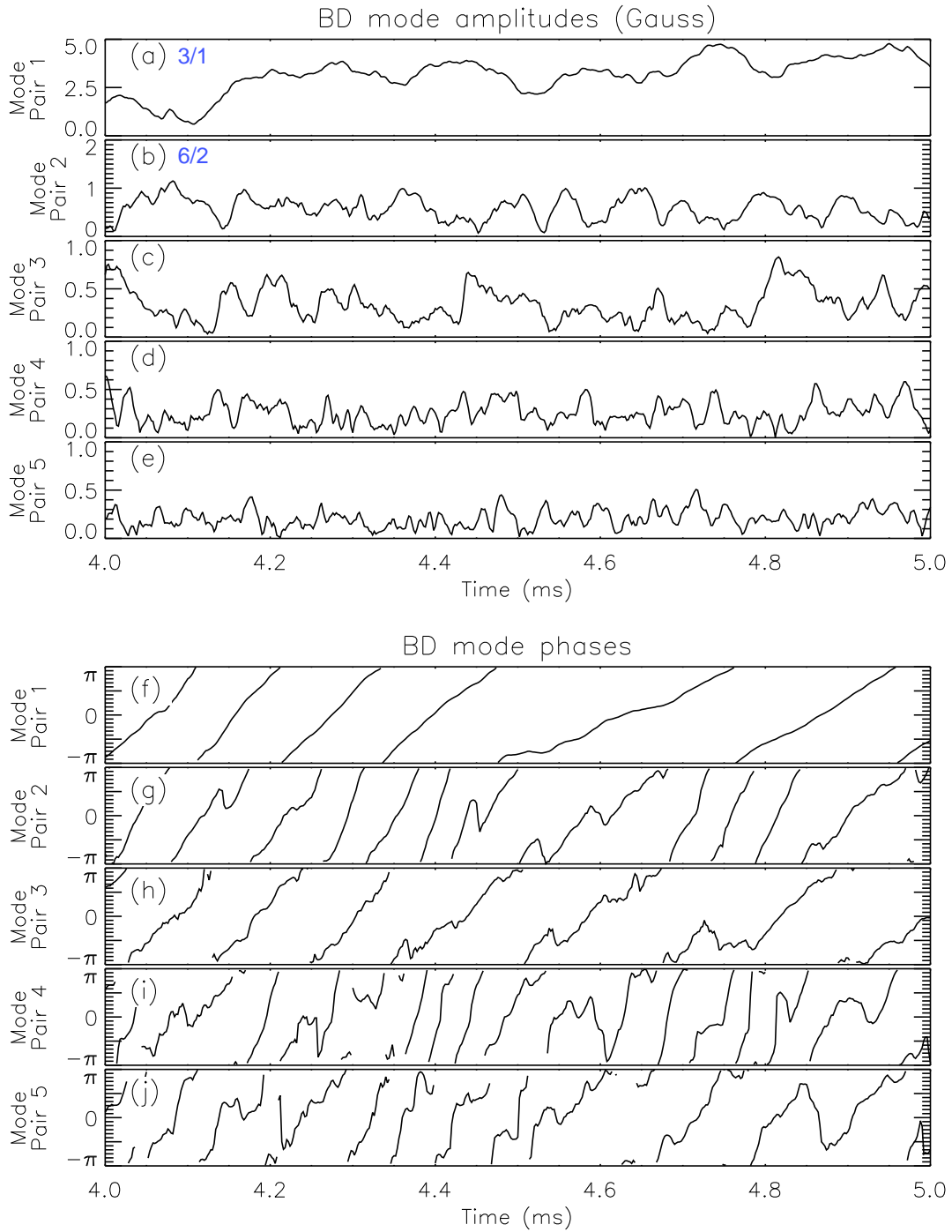
Figure 4.6: Amplitudes and phases for the five mode pairs shown in Figure 4.5.

behavior is given in Section 4.4. In order to study mode behavior over an entire discharge, subsets

of the discharge time can be analyzed through *piecewise* biorthogonal decomposition.

### 4.1.1   Piecewise Biorthogonal Decomposition

The most reliable way to use biorthogonal decomposition for HBT-EP data over long time periods

has been to analyze many overlapping subsets within the overall time range. If $S$ is the $M \times N$ matrix

of sensor signals over the range of interest, as defined in Section 3.1, we define a submatrix $S'$ as

$$S'(t) = S_{t-w,\ldots,t;1,\ldots,N} = U'\Sigma'V'^{\dagger} \tag{4.1}$$

with $w$ as the number of time points to include, and $N$ as the number of senors. All sensors are

retained, and a continuous subset of the times are used. Index $t$ is advanced from $w+1$ through $M$

with a desired step size. Temporal modes, singular values, and spatial modes for the subset are $\vec{u}'_i$,

$\sigma'_i$, and $\vec{v}'_i$ respectively. A given rotating mode's amplitude at time $t$ is then given by

$$A'(t) = \sqrt{2/N}\sqrt{(\sigma'_a \vec{u}'_a[w])^2 + (\sigma'_b \vec{u}'_b[w])^2} \tag{4.2}$$

where $a$ and $b$ indices refer to a quadrature pair of BD modes, and $\vec{u}'_i[w]$ is the last element in

the temporal mode array. In other words, mode amplitude at time $t$ is determined by using the

BD over the previous $w$ time points, then using the temporal mode information at time $t$ (i.e. the

end of the interval). The factor $\sqrt{2/N}$ puts the resulting amplitude in real units of field strength,

instead of the normalization from $\vec{v}'_i \cdot \vec{v}'_j = \delta^j_i$. This assumes a Fourier-like mode structure, but is

still representative otherwise.

Example modes from analyzing shot 70246 in 1 ms intervals are shown in Figure 4.7. Time

advances downward in the figure in 0.5 ms steps. Evolution of the spatial mode structures over time

is apparent by examining the poloidal arrays. The small structural change in this case is mostly

due to the changing major radius. The times shown in Figure 4.7 are overplotted in Figure 4.8 to

aid comparison of the spatial modes. These plots show the change in shape, but not the relative

importance (i.e. amplitude) of each mode.

Note that in these and other plots comparing mode shapes over time, BD spatial mode phase is

forced to be roughly the same across different analysis windows to allow easier structural comparison
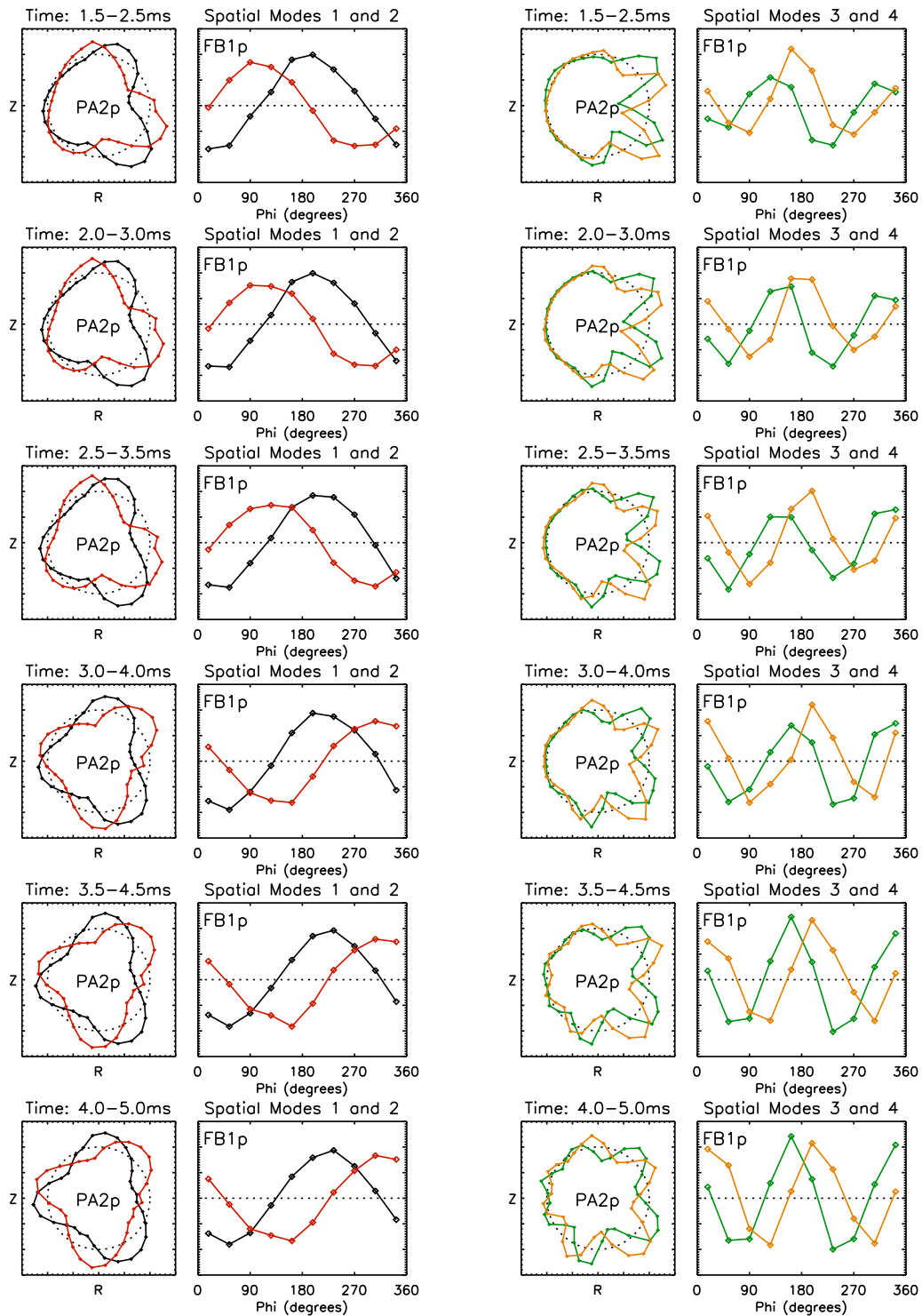
Figure 4.7: The first four BD spatial modes for shot 70246, as analyzed in 1 ms intervals. Poloidal sensors are shown for one poloidal array and one feedback sensor group to give $m$ and $n$ information. Modes are appropriately grouped into two quadrature pairs; the first mode pair is shown in the first 2 columns, while the second pair is in the last 2 columns. Time advances downward in 0.5 ms steps.
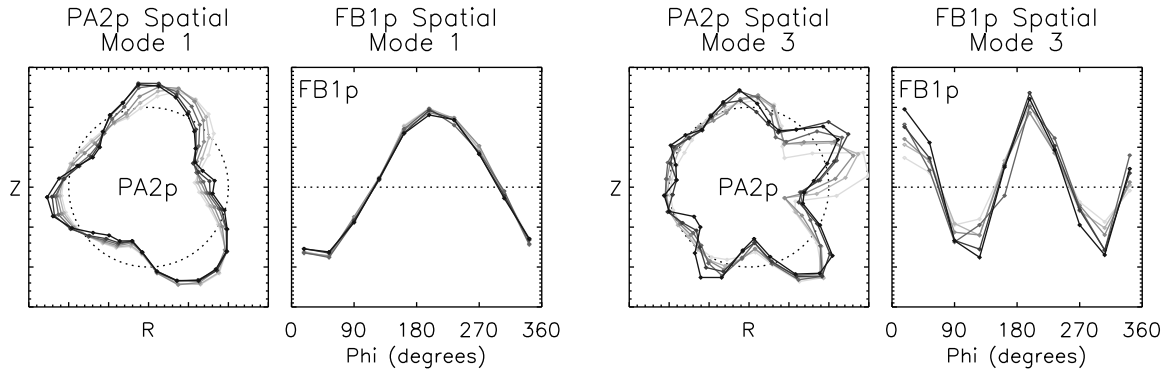
Figure 4.8: Spatial modes from Figure 4.7, overlaid for easier comparison. One mode from each pair is shown. Darker lines are from later time ranges.

by eye. This is done by linearly combining both spatial modes in a given pair as could be done for a *sine/cosine* pair to achieve a requested phase, assuming that the two modes are perfectly degenerate. Linearly combining modes is necessary because determination of the *sine* or *cosine* phase offset is somewhat arbitrary for the rotating mode pairs.

One possible drawback of this piecewise method is coupled with its benefit – modes in different time windows are not restricted to have the same spatial mode structure. This can cause misinterpretation of mode amplitude changes over time in a given shot if one only considers amplitudes based on singular values without examining shape of the BD spatial modes. An example would be a shot with a dominant external 3/1 mode in one early time window and a strong 2/1 tearing mode later, with a quiet period between. Looking only at the singular values, one would say that the observed (dominant) mode is strong early in the discharge, then recedes before becoming strong again. Even if the two modes are completely different, they would each show up as the dominant mode in their respective time intervals. The inherent flexibility of the BD-derived basis means that resulting modes must be interpreted carefully.

One way to enforce a specific empirical mode structure is to use the biorthogonal decomposition over a narrow time window for a given set of parameters, then apply those spatial mode structures to other shots or times. Measured fluctuations are dotted onto the previously calculated spatial modes to determine amplitudes and phases for a given time. This has the advantage of using empirically determined modes and will guarantee specific mode shapes, which would be beneficial when looking for desired helicities. However, this forces the shape to be the same across multiple shots or times, and removes some of the flexibility of BD analysis. This method was used in other HBT-EP research

to study effects of applied resonant magnetic perturbations [46]. Analysis presented in this thesis recalculates the BD basis for every time interval, retaining the spatial mode flexibility.

Figure 4.7 shows the two dominant mode pairs evolving smoothly over time for this shot. We can interpret these as two specific rotating modes that persist and change shape at the sensors over time. In this case the shape change is caused by the sensors sampling the modes more uniformly as the plasma moves closer to being concentric with the poloidal arrays. The first mode pair is clearly 3/1 during 1.5–5.0 ms. The second mode is $n = 2$ the whole time, with $m = 5$ or 6 at the start, then $m = 6$ by the end. Interactions between 3/1 and 6/2 modes will be discussed in Section 4.4.

## 4.2   Comparing spatial mode structures

Plots of BD spatial mode structures shown so far have allowed qualitative comparison of the mode shapes. The spectral content of a mode can be used to quantify its spatial shape. To calculate amplitudes of toroidal mode numbers in a given BD mode, we integrate against a Fourier basis:

$$A_n = \frac{1}{\pi} \left( \int_0^{2\pi} \delta B(\phi) \cos(n\phi) d\phi \right)^2 + \frac{1}{\pi} \left( \int_0^{2\pi} \delta B(\phi) \sin(n\phi) d\phi \right)^2 \tag{4.3}$$

where $\delta B(\phi)$ contains a portion of the spatial mode $\vec{v}_i$ corresponding to a uniform set of sensors in the toroidal direction, normalized to $\int_0^{2\pi} \delta B^2 d\phi = 1$. For example, to get toroidal mode number content from one of the feedback sensor groups, $\delta B(\phi)$ will contain the 10 entries in $\vec{v}_i$ which are for that set. Note that $\sum_{n=0}^{\infty} A_n = 1$, so $A_n$ represents the percentage of energy in each Fourier component. When two BD modes represent a rotating pair, their spectral content is averaged.

Poloidal mode numbers can be calculated in the same manner using $\theta$ instead of $\phi$. However, toroidal curvature in a tokamak causes the field line pitch to change while transiting the poloidal cross-section. The toroidal field is stronger on the inboard side of the plasma, making the local pitch of the field lower. We expect the phase of a kink mode to follow the field, which effectively reduces the poloidal mode wavelength on the high-field-side. The reference poloidal angle can be appropriately modified [55] using

$$\theta^* = \theta - \lambda \sin(\theta) \tag{4.4}$$

with

$$\lambda = \left( \beta_p + \frac{l_i}{2} + 1 \right) \frac{a}{R_0} \tag{4.5}$$

where $\beta_p$ is given by Equation 1.4, and $l_i$ is the plasma internal inductance. When $\lambda = 0$, the poloidal angle returns to its original cylindrical form. Using the modified poloidal angle $\theta^*$, poloidal mode number content is then calculated through

$$A_m = \frac{1}{\pi}\left(\int_0^{2\pi}\delta B(\theta^*)\cos(m\theta^*)d\theta^*\right)^2 + \frac{1}{\pi}\left(\int_0^{2\pi}\delta B(\theta^*)\sin(m\theta^*)d\theta^*\right)^2 \tag{4.6}$$

where $\delta B(\theta^*)$ contains a portion of the spatial mode $\vec{v}_i$ from one of the poloidal arrays.

We can estimate the $\lambda$ parameter in HBT-EP using the toroidal equilirium condition [6]

$$\beta_p + \frac{l_i}{2} = \frac{4\pi R_0 B_v}{\mu_0 I_p} - \ln\left(\frac{8R_0}{a}\right) + \frac{3}{2} \tag{4.7}$$

where $B_v$ is the vertical magnetic field at the major radius. Although the current centroid is measured in HBT-EP instead of the geometric center of the flux surfaces, analysis in this thesis assumes that the Shafranov shift [56] is negligible with respect to these calculations.

We also care about the relative amplitude of each observed mode, not just differences in shape. For instance, two shots could have the same shape for two dominant modes, but one of the shots could have more power in the secondary mode. This would indicate that the secondary mode is more important in certain cases than in others. Equations 3.4 and 4.2 are used for amplitude comparisons.

## 4.3  Transitions between dominant poloidal mode numbers for $n = 1$ modes

The edge-q naturally changes as plasmas evolve in HBT-EP discharges. This moves the kink-resonant surface, which is critical for kink stability in circular, limited plasmas. Typical $q_*$ values remain between 2 and 4 for most shots, giving rise to $n = 1$ modes with dominant poloidal modes numbers of $2 - 4$. The inherent symmetry of tokamaks in the toroidal direction makes $n$ a good quantum number, however the lack of symmetry in the poloidal direction will give rise to a spectrum of $m$ numbers for a given $n$. Toroidal curvature in a device causes the pitch of a given field line to change as it transits in the poloidal direction, which this produces geometric coupling to $m \pm 1$ Fourier modes for a given dominant poloidal mode number $m$ [55].

Transitions between dominant $m$-numbers have been seen for many HBT-EP discharges. An
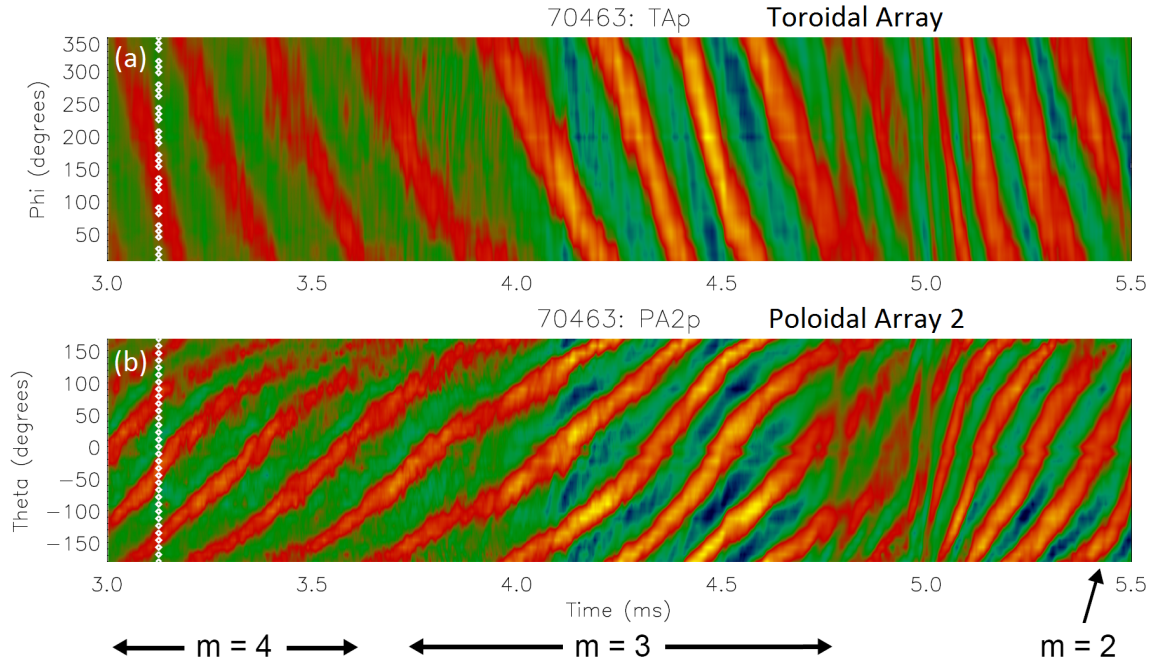
Figure 4.9: Toroidal and poloidal array $\delta B_p$ fluctuations for a discharge showing transitions between $m = 4$, 3, and 2 modes. Equilibrium parameters for this shot are shown in Figure 4.1. Top and bottom shells were retracted by 4 cm in 3 adjacent sections. Although the shell configuration is not standard, this shot was analyzed since it has a very clean example of $m$-transitions.

example is given by shot 70463, with plasma parameters shown in Figure 4.1. The edge safety factor steadily decreases from $\sim 4$ to near 2 before the plasma disrupts. Resulting $\delta B_p$ fluctuations seen by the toroidal array and one poloidal array are shown in Figure 4.9. The dominant toroidal mode number is 1 for the whole discharge, with strong higher-order mode activity seen near 4.8 ms. There are also hints of $n > 1$ activity during 3.5–4.5 ms in these contour plots. The dominant poloidal mode number begins as $m = 4$, then evolves to $m = 3$ until becoming $m = 2$ just before the disruption at 5.6 ms. Fluctuations remain smooth through the transition.

When piecewise BD analysis is applied in cases like this, the spatial mode structure is allowed to differ for each interval. This is seen in Figure 4.10, where the dominant mode pair changes from 4/1 to 3/1, and the second mode changes from 7/2 to 6/2. The transition from $m = 4$ to $m = 3$ occurs when two peaks on the high-field-side ($\theta \sim \pm 180°$) merge into one. This is characteristic of $m = 4 \rightarrow 3$ and $3 \rightarrow 2$ transitions in HBT-EP – *peak merging always occurs on the high-field side.* This demonstrates the importance of having 360° coverage in the poloidal arrays. An outboard-only array would not witness this transition; poloidal mode numbers would need to be inferred from
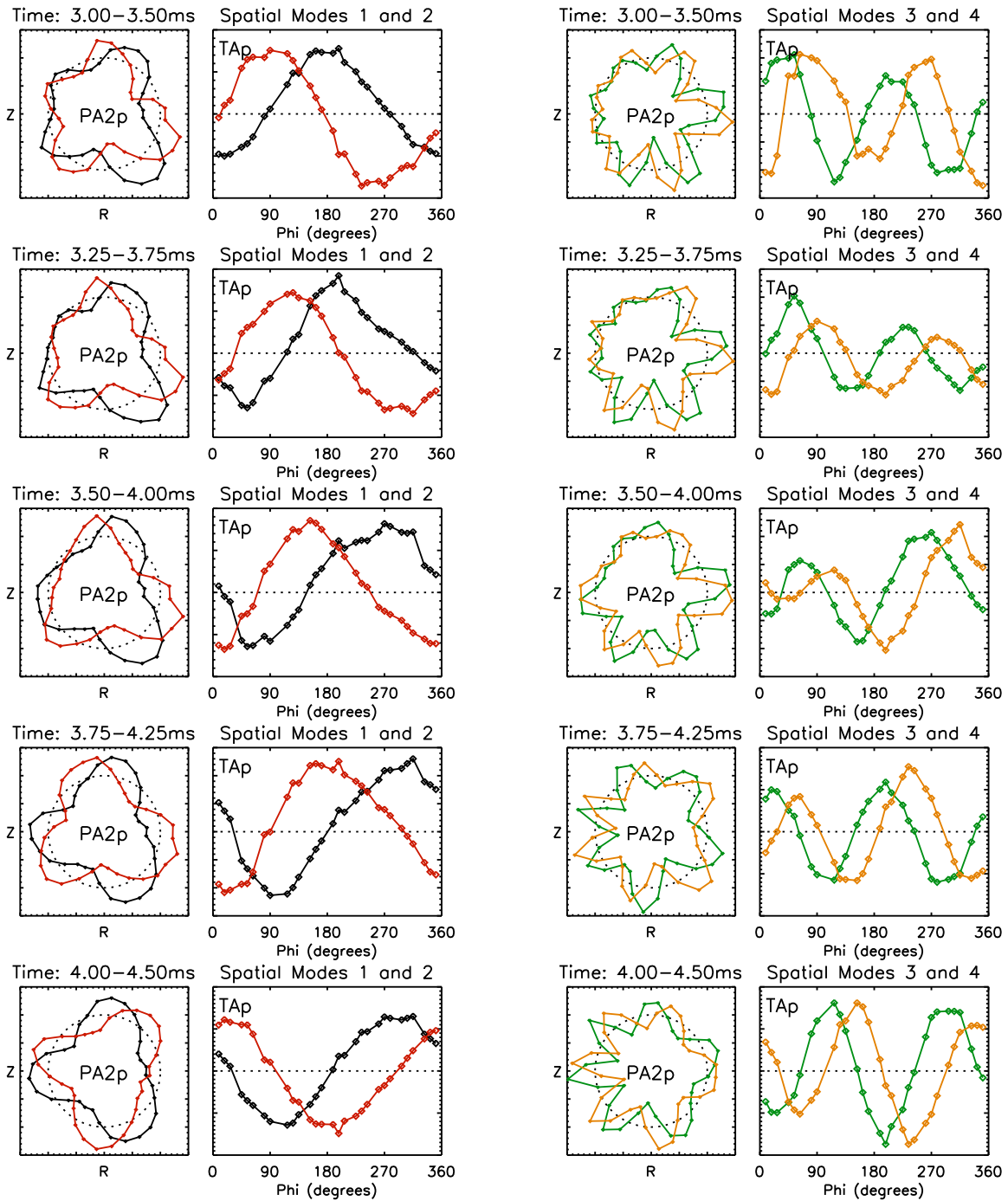
Figure 4.10: The first four BD spatial modes during the $m = 4 \rightarrow 3$ transition in shot 70463. Analysis intervals are 0.5 ms long, spaced by 0.25 ms, with time progressing downward. $\delta B_p$ modes are shown for one poloidal array and the toroidal array. The first mode pair is in the first two columns, while the second pair is in the last two columns.
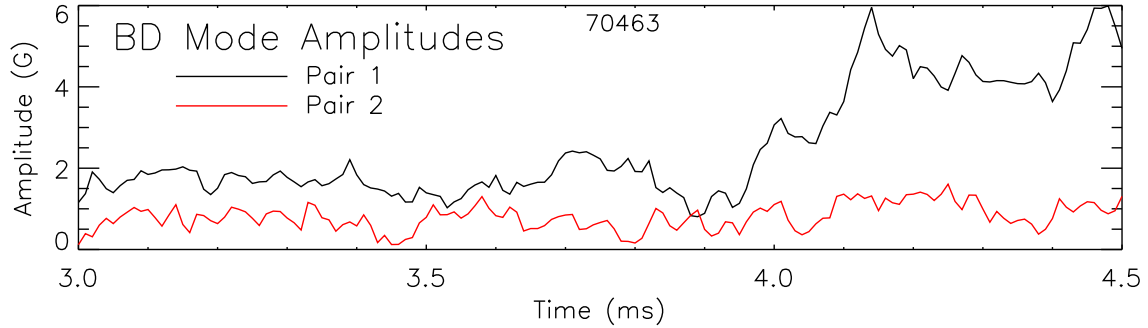
Figure 4.11: Amplitudes of the first two BD mode pairs when running the piecewise BD analysis.
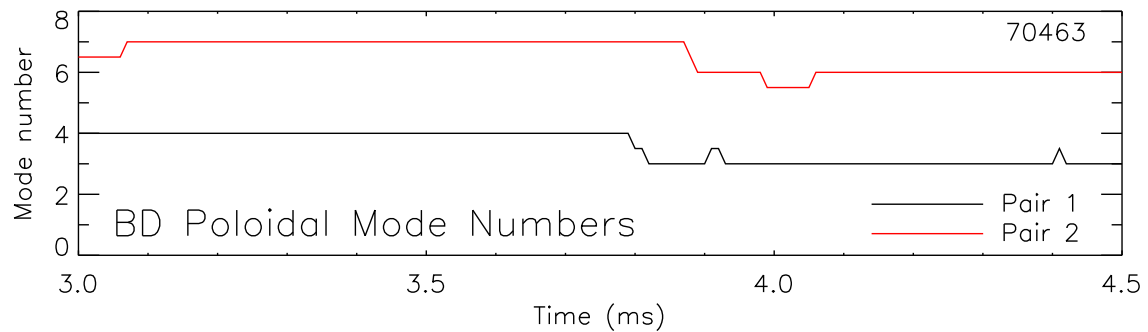


Figure 4.12: Poloidal mode numbers inferred from zero-crossings for shot 70463 having an $m = 4 \rightarrow 3$ transition for the dominant mode.

relative peak spacing on the low-field-side.

Amplitudes of the dominant mode pairs versus time are shown in Figure 4.11, as calculated using Equation 4.2. These amplitudes do not discriminate changing poloidal mode structures as Fourier analysis would. To assess mode numbers, we declare the characteristic poloidal mode number to be half the number of zero-crossings in the spatial mode. If there is a discrepancy between the 2 spatial modes in a given pair, then they are averaged. Poloidal mode numbers based on zero-crossings are shown in Figure 4.12. The first mode is seen to change from $m = 4$ to 3 near 3.8 ms, in agreement with the $\delta B_p$ plot in Figure 4.9(b). The second mode changes from $m = 7$ to 6 just before 3.9 ms. Toroidal mode numbers from the toroidal array are 1 and 2 for the first and second pairs, respectively.

Using zero-crossings gives discrete mode numbers, while having a mix of mode numbers would be a more-appropriate designation. The poloidal mode number spectrum of each spatial mode pair can be calculated at each time using the toroidal-curvature-modified basis functions in Equation 4.6,
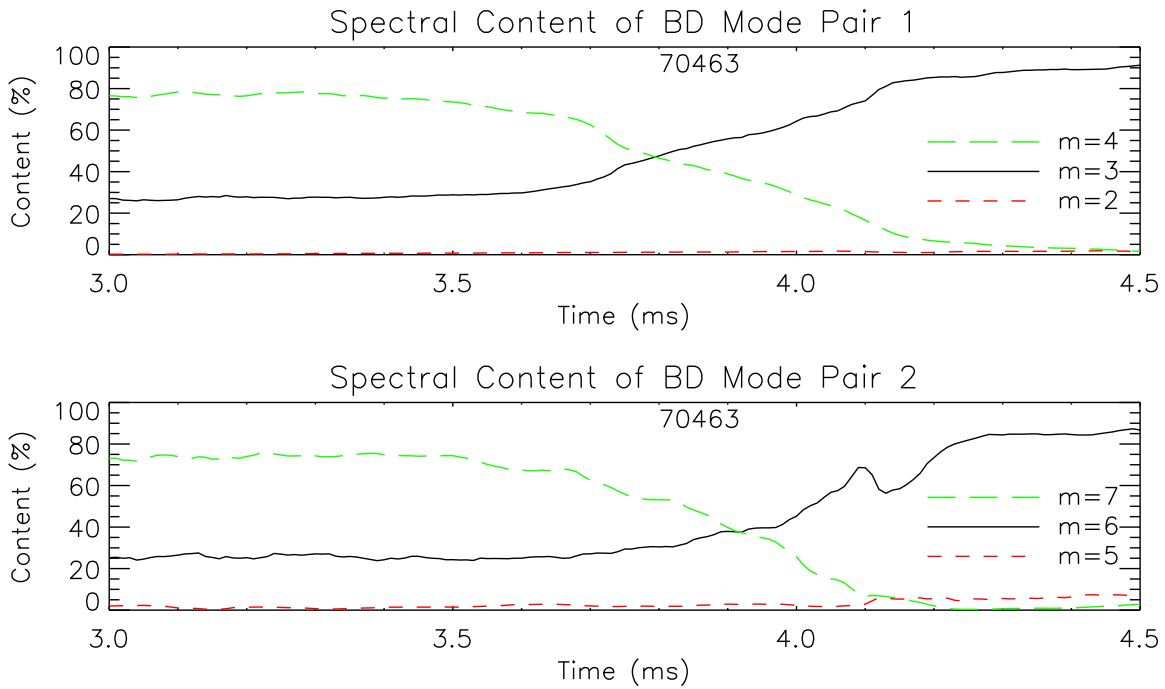
Figure 4.13: Poloidal mode number content of the two dominant BD mode pairs in shot 70463.

giving the results in Figure 4.13. The first mode is seen to have $m = 3$ characteristics the whole time, with $m = 4$ content dominating before 3.8 ms. For the second mode, the $m = 7$ nature dominates until becoming $m = 6$ near 3.9 ms. The interchanging of dominant spectral content agrees with the zero-crossing results, and gives additional information about mode structure.

**Analysis of a longer time window**

Decomposing the data during 3.0–4.5 ms in one interval gives the modes in Figure 4.14. Like in the case of the piecewise BD, the modes seen are 3/1, 4/1, 6/2, and 7/2. The 4/1 mode starts at around 1.5 Gauss, with a 3/1 mode at similar amplitude. The 4/1 decays slowly until a dramatic drop near 3.8 ms. Meanwhile the 3/1 grows slowly, then quickly grows starting around 3.9 ms until saturating at ∼5 G. The 6/2 mode is strongest toward the end of the time window. The 7/2 is weak, but still coherent throughout. The 3/1 and 4/1 modes rotate together, as do the 6/2 and 7/2 modes.

The relative mode amplitudes are consistent with the piecewise BD analysis, which showed strong 4/1 and 7/2 structure early, then 3/1 and 6/2 structure later. The long BD window shows four separate mode pairs that grow and decay independently. The piecewise BD only showed two prominent modes in any given interval, but these modes changed shape as time progressed. Whether
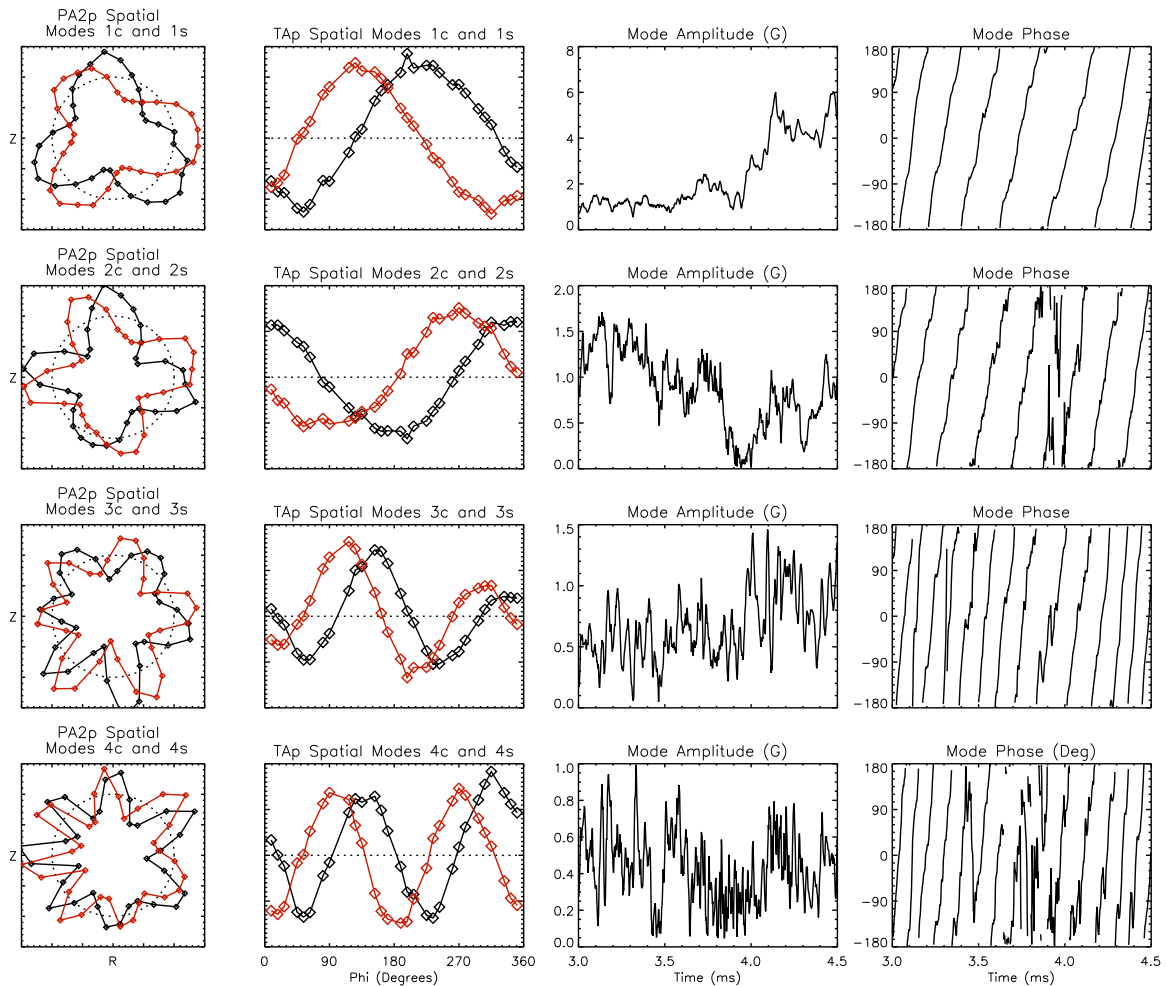
Figure 4.14: The first four mode pairs from analyzing an $m = 4 \rightarrow 3$ transition. Structures seen by a poloidal array and the toroidal array are shown in the first two columns, followed by each mode amplitude and phase. The phase is not accurately measured when mode amplitudes are near the noise floor of $\sim$0.1–0.2 G.

there were four separate modes growing and decaying simultaneously or two separate modes changing shape over time is a matter of semantics here; the $n = 1$ modes rotated together, as did the $n = 2$ modes, so the two interpretations are equivalent as far as the sensors are concerned.

It is interesting to note that for the long BD interval, the 4/1 mode phase flips by 180° relative to the 3/1 mode after its disappearance at 3.9 ms. This is another characteristic of a spurious 4/1 mode generated by analyzing a 3/1 mode when $R_0$ is changing, as seen in Figure 3.10(i,l). When analyzing a shorter time window of 3.5–4.5 ms, the 4/1 mode amplitude does not rise as much after 3.9 ms. This suggests that a 1.5 ms analysis interval is too long for this change in major radius.

## 4.4     Observation of multiple modes with the same resonance

Transitions between different dominant poloidal mode numbers as the edge-q changes are expected since the $q = m/n$ resonant surface moves. However, we have also observed many interesting cases where harmonics of the dominant mode, sharing the same helicity, become significant. The harmonics are often independent of the primary mode, and can sometimes dominate the overall mode structure for brief periods.

An exemplary case showing interaction of a dominant 3/1 mode with a secondary 6/2 mode is seen in shot 69694. Plasma parameters for this discharge are shown in Figure 4.1. Between 3 and 5 ms, the edge safety factor is measured to be relatively constant near 2.7 as changes in the plasma current, major radius, and minor radius balance. Poloidal field fluctuations during 4–5 ms are shown in Figure 4.15. The contour plots clearly reveal a rotating 3/1 structure for most of the time window. However, near 4.2 ms and 4.4 ms the mode behavior seems to change. After 4.2 ms the mode briefly becomes less coherent, or goes away. At 4.4 ms a higher-order mode structure becomes apparent with roughly double the spatial frequency. The 3/1 mode then grows until around 4.7 ms, followed by decay through the end of the time window. One can also see modulations of the 3/1 mode during 4.8–5.0 ms.

Biorthogonal decomposition of all poloidal sensors and radial feedback sensors produces the mode structures shown in Figure 4.16. Spatial mode structures are clearly 3/1 and 6/2 quadrature pairs. Singular values, amplitude, and phase of the mode pairs are shown in Figure 4.17. Although the modes have the same helicity and resonate with the same rational surface, the phase plots in Figure 4.17 show independent rotations – the 3/1 mode slows down while the 6/2 speeds up. The 6/2 phase appears coherent during the whole time window, in spite of its low amplitude most of the time.

Neither the phase nor amplitude of the 6/2 simply track with the 3/1 mode, indicating non-rigid multimode behavior. Between 4.2 and 4.7 ms there is exponential growth of the dominant 3/1 mode while the 6/2 remains at low amplitude. However, at 4.4 ms, the 6/2 mode rapidly grows at the expense of the 3/1. The 6/2 mode then decays, and the 3/1 grows again. There are no abrupt changes in equilibrium parameters at this time which might explain the interchanging mode amplitudes. After 4.6 ms the 6/2 mode appears to modulate the 3/1, as quick bursts of 6/2 activity are accompanied by reductions in 3/1 amplitude. Bursts of mode activity were simulated in Section 3.3.2, and pose no problems in the BD analysis. Although the major radius decreases significantly
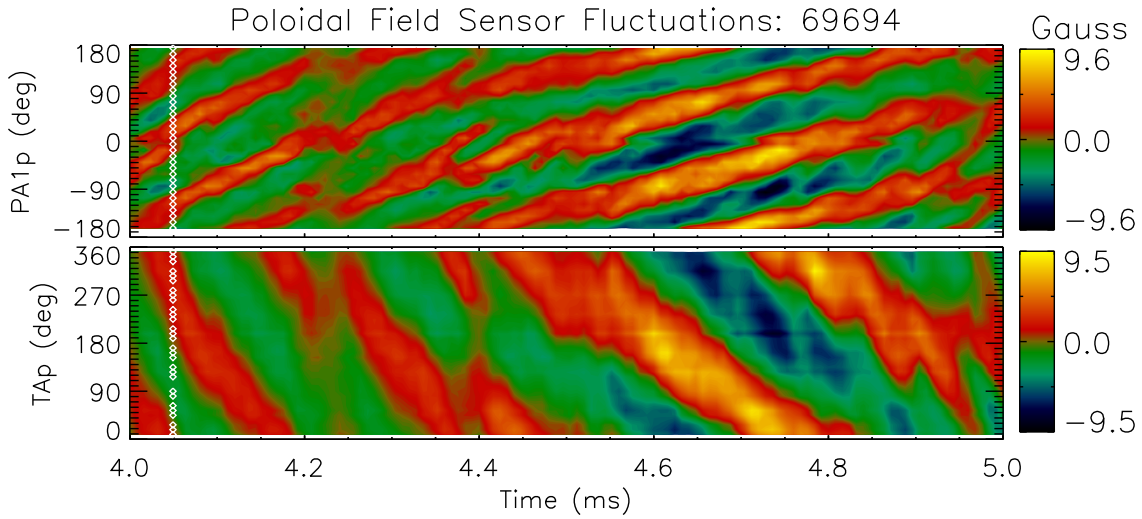
Figure 4.15: Plot of poloidal field fluctuations as seen by a poloidal array and the toroidal array. Plasma current is slightly above 15 kA, and $q_* \approx 2.7$ during the time shown. Distortion of the dominant 3/1 mode is seen at 4.4 ms and during 4.8–5.0 ms.
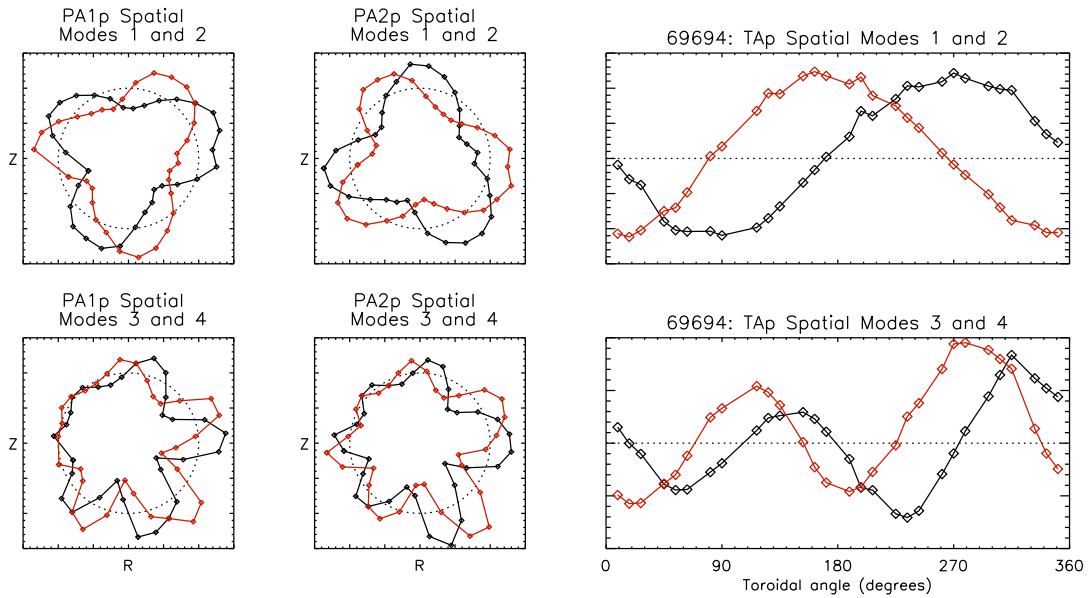


Figure 4.16: Spatial modes from biorthogonal decomposition of shot 69694 are shown for the poloidal and toroidal arrays. Clear 3/1 and 6/2 modes are seen, with no *a priori* assumption of mode structure.

during the 4–5 ms period, using shorter BD analysis windows does not change the observed 3/1 and

6/2 interactions.
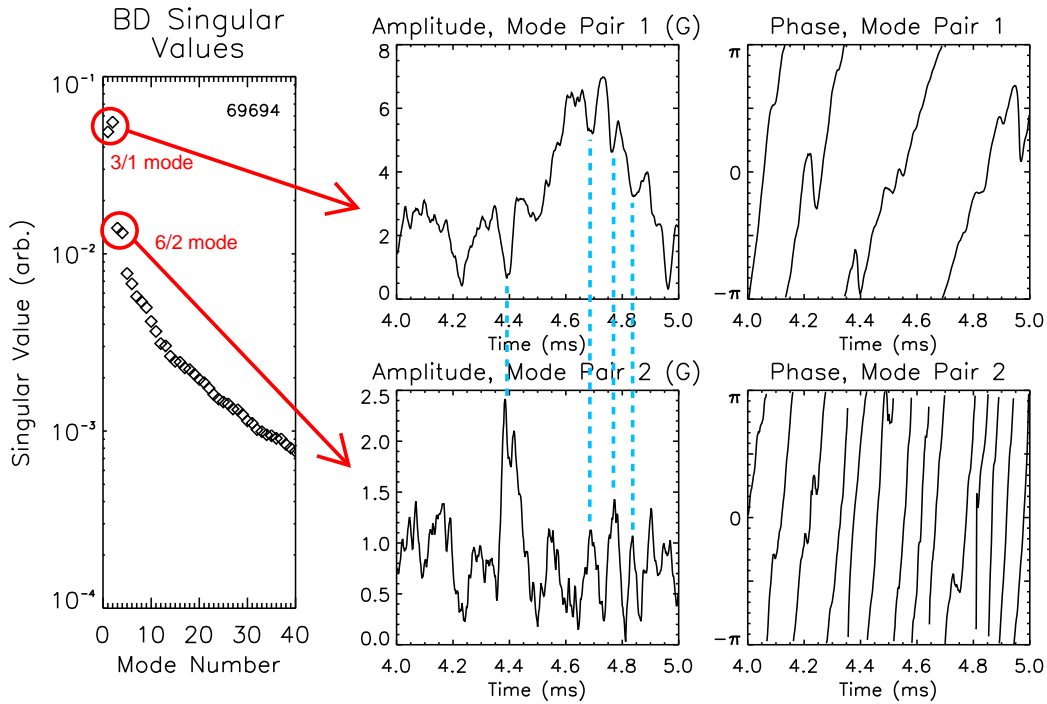
Figure 4.17: Biorthogonal decomposition for shot 69694 shows clear pairing of singular values for the rotating 3/1 and 6/2 modes. Modes 1 and 2 correspond to the 3/1 mode (*sine* and *consine*), modes 3 and 4 represent the 6/2 mode. Amplitude and phase of the 6/2 mode do not simply track with the 3/1 mode. Rapid 6/2 growth is seen during periods of decreasing 3/1 amplitude, notably at 4.4 ms. (Note that the second singular value is larger than the first – this is a numerical result of the IDL SVDC routine, and does not affect the analysis.)

## 4.4.1   Mode behavior variability between shots

Interactions of specific modes is not necessarily consistent across shots with the same equilibrium parameters. Multimode activity can be very different, even though the equilibrium parameters and their evolution are the same as far as we can measure on HBT-EP. Figure 4.1 shows measured equilibrium parameters for the shot discussed in the previous section overlaid with the following discharge (69694 and 69695). The two shots had resonant magnetic perturbations applied during 2–3 ms with different amplitudes, but the perturbation strengths were small enough that they shouldn't have influenced the rest of the discharge.

Figures 4.18 and 4.19 show the poloidal field fluctuations and BD results from shot 69695. Again there are 3/1 and 6/2 modes present. The 6/2 still appears to modulate the 3/1, especially while the 3/1 mode slows down between 4.4 and 4.7 ms, but there is no time where the 3/1 disappears while the 6/2 takes over.
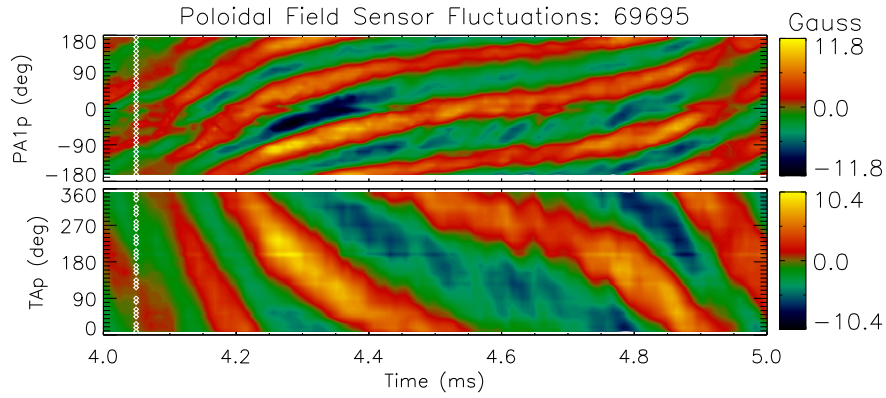
Figure 4.18: Plot of poloidal field fluctuations as seen by a poloidal array and the toroidal array. Equilibrium parameters are the same as for shot 69694 in Figure 4.15. Distortion of the dominant 3/1 mode is seen while it slowly rotates around 4.6 ms.
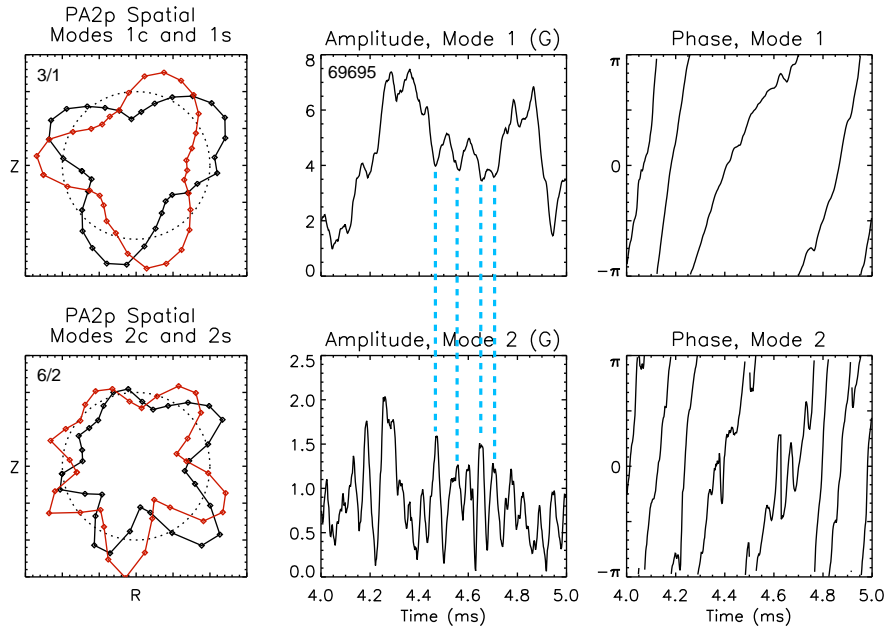


Figure 4.19: Two dominant modes from biorthogonal decomposition of shot 69695. Mode evolutions are different than shot 69694 with the same equilibrium.

Measured equilibrium parameters are nearly identical for the two shots, but the mode activity is different. However, there are equilibrium parameters that are not measured in HBT-EP, such as bulk plasma rotation or impurity content, which may affect mode behavior in cases like these. Single shots will not necessarily be representative of typical mode behavior when the measured plasma parameters are the same. Therefore the following chapters use statistics of mode behavior over many shots in order to establish trends.

## 4.5 Summary of observations

External kink modes in HBT-EP are often observed to grow, saturate, and decay without terminating the discharge. Choosing appropriate intervals for the biorthogonal decomposition allows these modes to be studied without predefining a basis. Using the BD for intervals that are too long with respect to the changing equilibrium was shown to produce spurious modes. This was simulated in Section 3.3.4, and seen experimentally in Section 4.1. Using a piecewise BD method allows analysis of an entire discharge while having appropriate length subintervals.

Biorthogonal decomposition yields mode structures that are coherent in space and time. Spectral analysis can be done on the resulting spatial modes to quantify poloidal and toroidal mode number content. This contrasts with calculating the spectral content at each time point separately, which does not include temporal coherence.

During transitions between dominant $m$-numbers for $n = 1$ modes, merging of peaks always occurs on the high-field side of the torus. This demonstrates the importance of having adequate poloidal coverage of sensors when determining poloidal mode numbers. Coexistent 3/1 and 6/2 modes are observed as independent in both amplitude and rotation, giving clear evidence for non-rigid, multimode behavior. Amplitude modulation is observed between 3/1 and 6/2 modes, and the 6/2 mode is able to dominant the perturbation for brief periods. Variation is seen in multimode interactions across discharges with the same measured equilibrium parameters, which motivates the statistical treatments used in the following chapters.

# Chapter 5

# Plasma Parameter Changes

As we saw in Section 4.4.1, mode behavior can vary dramatically on a shot-to-shot basis. Examining one shot will not necessarily give results which are representative under similar equilibrium conditions. Comparing many similar shots to establish statistical significance is necessary for making firm statements about typical mode behavior. This chapter presents statistical analysis of mode amplitudes and spectral content over tens of shots, separated by low-initial-$q$ and high-initial-$q$ designations.

## 5.1   Natural variation of HBT-EP parameters

HBT-EP discharges are developed by pre-programming voltages and timings on six capacitor banks. There is no active control of the equilibrium during a given discharge. This leads to natural variation and evolution of plasma parameters due to various uncontrolled conditions. It is difficult to exactly reproduce parameters such the major radius on a shot-to-shot basis, as there is no active vertical field control. This prevents exact programming of the discharge evolution, but allows parameters to be scanned with small random variations by comparing shots that were similarly programmed. An example of such differences is shown in Figure 5.1, where all of the shots had the same capacitor bank timings, bank voltages, puff time, and the same base pressure. The discharges shown have initial $q_* < 3$ at the end of the startup period; discharges with initial $q_* > 3.3$ tend to have better reproducibility.

   Aside from shot-to-shot variation, plasma parameters will also vary significantly during periods of
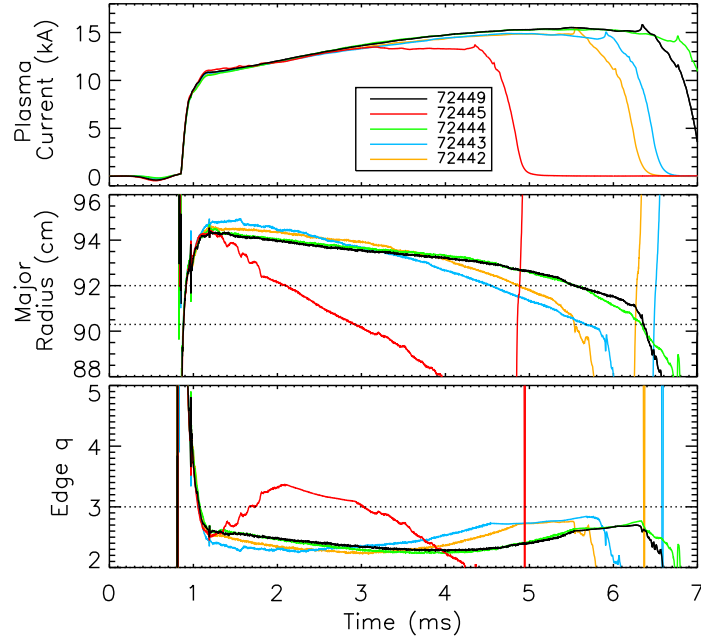
Figure 5.1: Plasma current, major radius, and edge q for five shots with the same bank settings and base pressure, showing shot-to-shot variation for discharges starting with $q_* < 3$. Shots like 72445 were not included in the standard analysis.

interest within a single discharge. This allows us to scan parameters within a single shot, in addition to using multiple shots. Figure 5.1 also shows examples of variation in plasma current, major radius, and edge-q within individual shots. Shots like 72445 were not included in the following statistical analyses since they were dramatically different and had rapidly changing equilibrium characteristics.

## 5.2 Comparing mode amplitudes

In order to average mode behavior over many shots, the piecewise BD analysis was run on several shot databases using 0.5 ms intervals. Mode amplitudes at the end of each interval were used via Equation 4.2. For example, the amplitude of a mode at time 3.5 ms corresponds to doing the BD analysis over 3.0–3.5 ms, then using the BD temporal mode amplitudes at 3.5 ms. A representation of two analysis intervals and the resulting amplitude versus time is shown in Figure 5.2.

Since major radius and edge safety factor are both expected to have a large impact on observed mode activity, small differences in either one cannot be ignored when studying mode amplitudes. A plot of mode amplitude versus $R_0$ and $q_*$ for shot 72400 is shown in Figure 5.3. This individual shot maps out one trajectory in $R_0$–$q_*$ space, beginning at 94.5 cm and $q_* = 2.4$. Data points
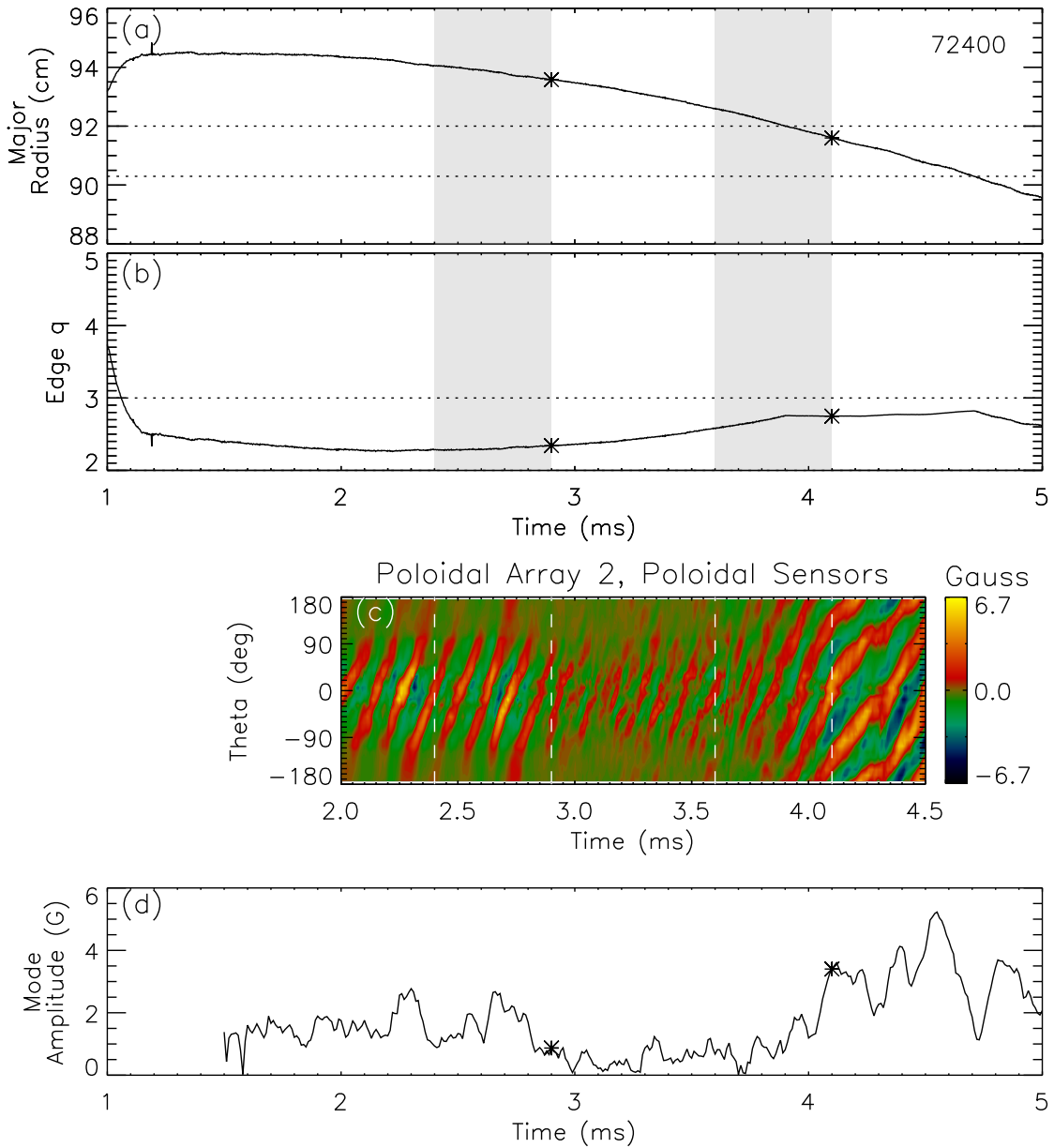
Figure 5.2: Major radius, edge safety factor, and $\delta B_p$ fluctuations as seen by one of the poloidal arrays. Also shown is the dominant BD mode pair amplitude, as calculated using Equation 4.2 with 0.5 ms intervals. The marked points use the shaded regions for BD analysis.

begin 1.5 ms into the shot, and time progresses downward. Figures 5.2 and 5.3 show that the mode amplitude is significant early in the shot, then decays away during 3–4 ms before rising again. The poloidal array plot in Figure 5.2(c) shows that the mode was primarily $m = 2$ prior to 3 ms, then becomes $m = 3$ before 4 ms. The earlier mode is actually a 2/1 tearing mode, while the later mode
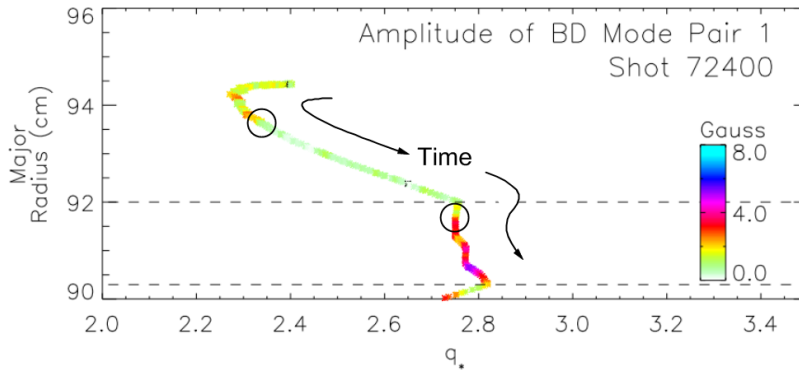
Figure 5.3: Trajectory of shot 72400 in major radius versus edge-$q$ space. Time progresses downward. Parameters versus time are shown in Figure 5.2. Colors at specific points represent the dominant BD mode pair amplitude at that time. Early in time the mode activity is 2/1 dominated, while later it is 3/1 dominated.
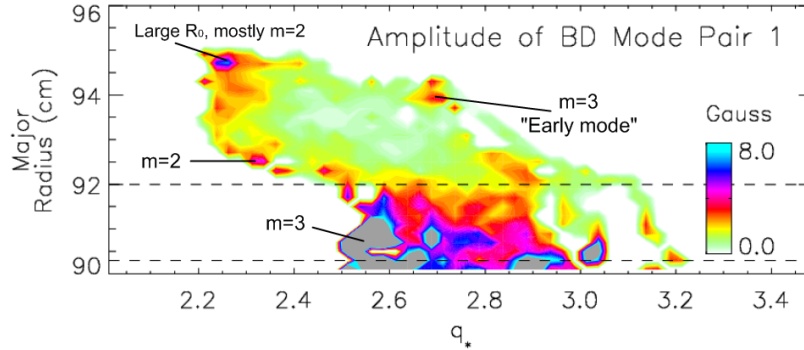


Figure 5.4: Averaged trajectories of 35 shots from low-$q$ experiments. Contours represent the dominant BD mode pair amplitude. Gray regions are above the upper limit of the color bar, $> 8$ Gauss. Several regions are annotated with the dominant poloidal mode structure.

is a 3/1 external kink. As discussed in Section 4.1.1, this analysis does not consider mode shapes when calculating amplitudes.

Calculating the $R_0$–$q_*$ trajectory for many shots will reveal typical mode behavior under similar conditions. Figure 5.4 shows a plot where 35 shots have been averaged for low-$q$ experiments. Several regions of the plot have been annotated with the measured spatial mode structure. Points along trajectories are binned according to $R_0$ and $q_*$, then all amplitudes falling within a given bin are averaged. Bins are 0.025 wide in $q_*$, and 0.2 cm tall in $R_0$. Plots like this are used to evaluate typical mode amplitudes in the following sections. Spectral contents of the modes are binned and averaged in a similar manner, with different $m$ and $n$ numbers occupying separate plots.

## 5.3    Different discharge categories

All plasmas analyzed in this thesis use the discharge programming described in Section 2.2, where a fast start-up is followed by a gradual current ramp. The main emphasis was on 3/1 modes and their interactions with other modes, thereby setting a target $q_*$ slightly below 3.

Most experiments since the 2010 HBT-EP shell upgrade have studied mode activity while crossing $q_* = 3$ from above. These plasmas pass through $m/n = 3/1$ tearing and ideal external kink regimes before reaching resistive wall mode conditions. In order to avoid complications arising from having a previously-existing saturated mode when the RWM goes unstable, shots were also developed for this thesis with $q_*$ approaching 3 from below. These low-$q$ shots are similar to those developed by Shilov for a previous conducting wall [57]. Typical high-$q$ and low-$q$ shots are shown in Figure 5.5. Low-$q$ shots are defined as those having $q_* < 3$ at the end of the *startup* stage of the discharge. Here, the $q = 3$ surface is external from the start of the discharge, precluding existence of 3/1 tearing modes until after the RWM regime has been passed. The figure also shows a "dip-style" shot, which will be discussed in Section 5.3.2. All three discharge categories were used in this thesis to investigate possible differences in multimode behavior.

### 5.3.1    Approaching $q_* = 3$ from below

When the edge safety factor approaches the $q = 3$ resonance from below, the 3/1 RWM can grow without starting as a saturated ideal external kink or tearing mode. Tearing modes resonant with $q < 3$ may still exist, and can present problems in the BD analysis when we are only concerned with 3/1 activity. Amplitudes for the two dominant BD mode pairs versus $R_0$ and $q_*$ for 35 shots are shown in Figure 5.6(a-b). Ratios of the secondary mode amplitude to the dominant mode are shown in Figure 5.6(c), and represent the relative importance of the second mode pair. The black and gray outlines are explained in later discussions.

Evaluating the poloidal and toroidal Fourier content of the dominant spatial mode structures in Figure 5.6(a) using Equations 4.6 and 4.3 gives the results in Figures 5.7 and 5.8. Here, spatial modes measured by one poloidal array are compared with a Fourier poloidal mode basis, correcting for major/minor radius effects. Likewise, spatial modes from one of the feedback sensor groups are compared against a Fourier toroidal mode basis. Figures 5.7 and 5.8 show $\sqrt{A_m}$ and $\sqrt{A_n}$ to give better dynamic range, thus the contours represent square roots of the percentage of energy in each
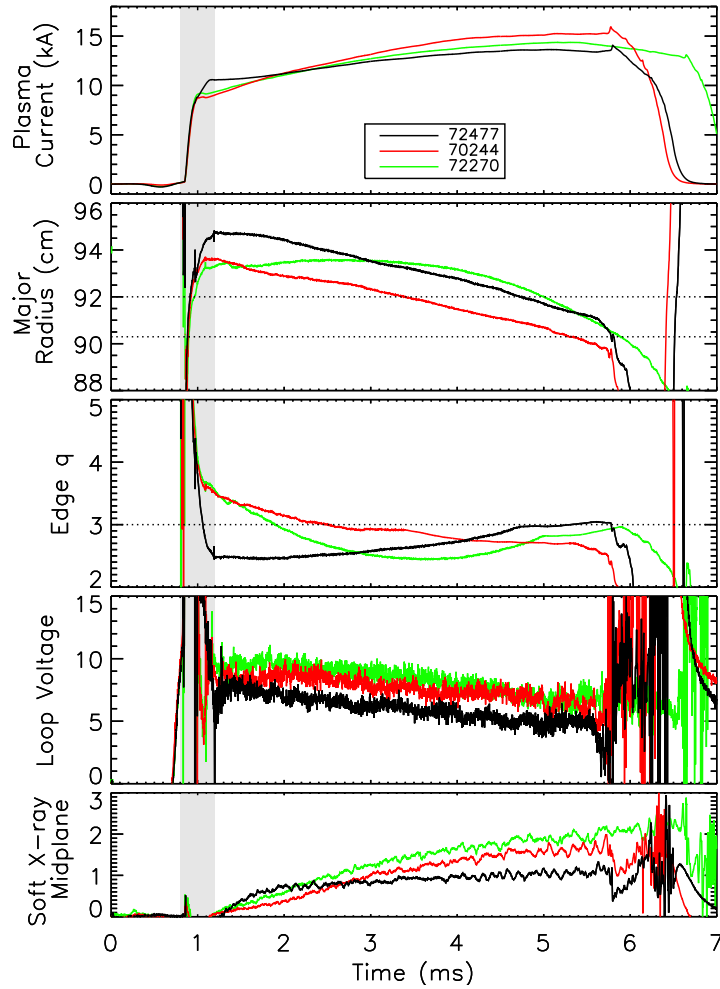
Figure 5.5: Plasma parameters for example low-$q$ (72477, black), high-$q$ (70244, red), and dip-style (72270, green) shots. The startup period (shaded) is not considered when discussing evolution of parameters.

Fourier component. The dominant spatial modes are mostly $m = 2$ for $q_* < 2.5$, and $m = 3$ for $q_* > 2.7$. Mode structures are a mix of $m = 2$ and $3$ Fourier content in the intermediate range, but zero-crossings in the spatial modes suggest that the $m = 3$ designation is more accurate for most shots. Note that the poloidal and toroidal mode numbers are *not* treated separately by the BD; a single BD mode pair contains poloidal and toroidal information together.

Figure 5.6 shows that both mode amplitudes are strongly linked to the major radius. Overall mode amplitudes increase as the major radius decreases. One reason for this is because the plasma boundary becomes more conformal to the sensor set as $R_0$ approaches 92 cm. The plasma gets closer to the toroidal array and poloidal array sensors, thus the mode is measured as stronger. This
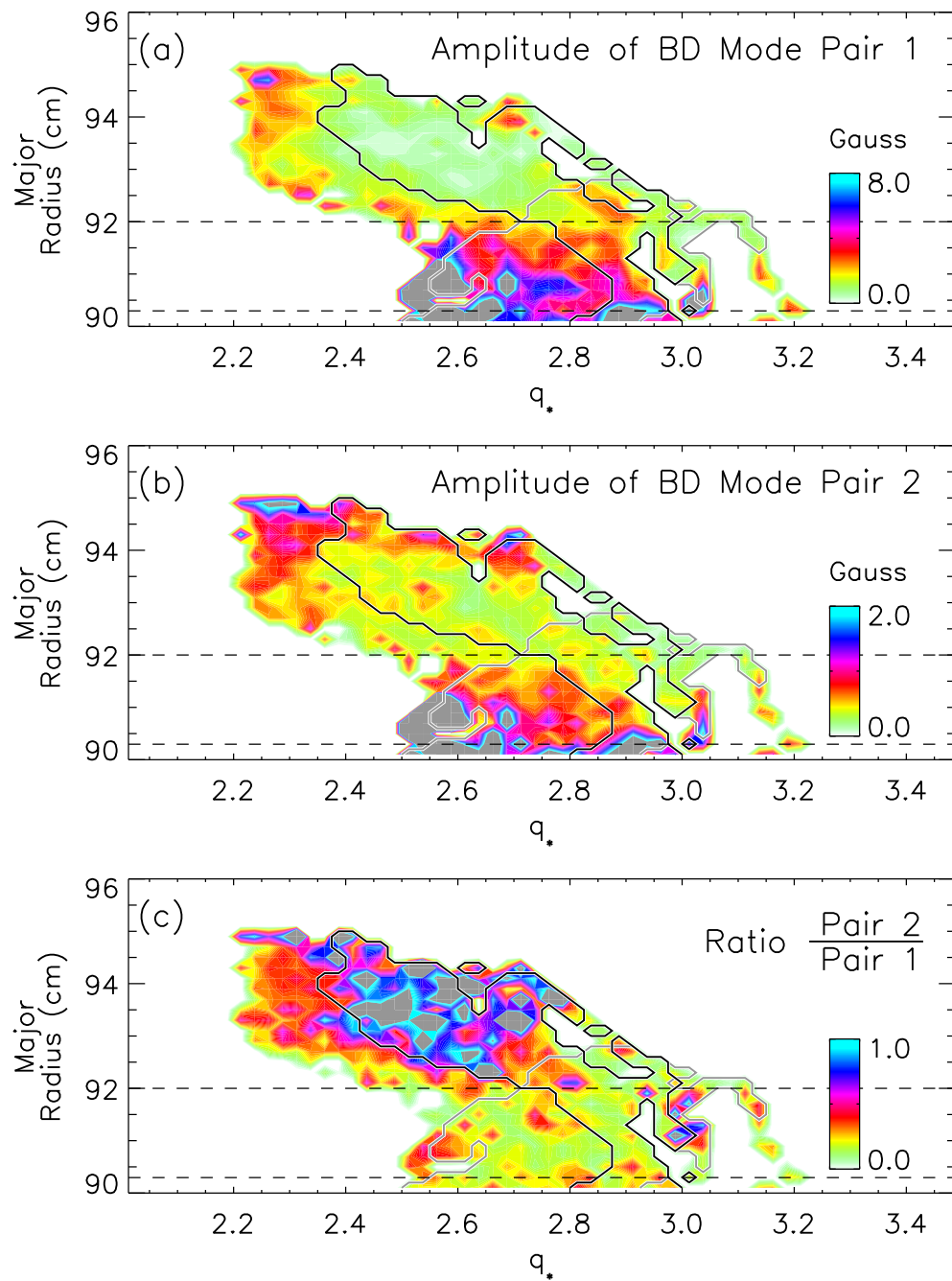
Figure 5.6: Averaged trajectories of 35 shots from low-initial-q experiments. Contours represent instantaneous mode amplitude for (a) the dominant BD mode pair, (b), the second pair, and (c) the ratio $Pair2/Pair1$. The black and gray outlined regions are for later reference.
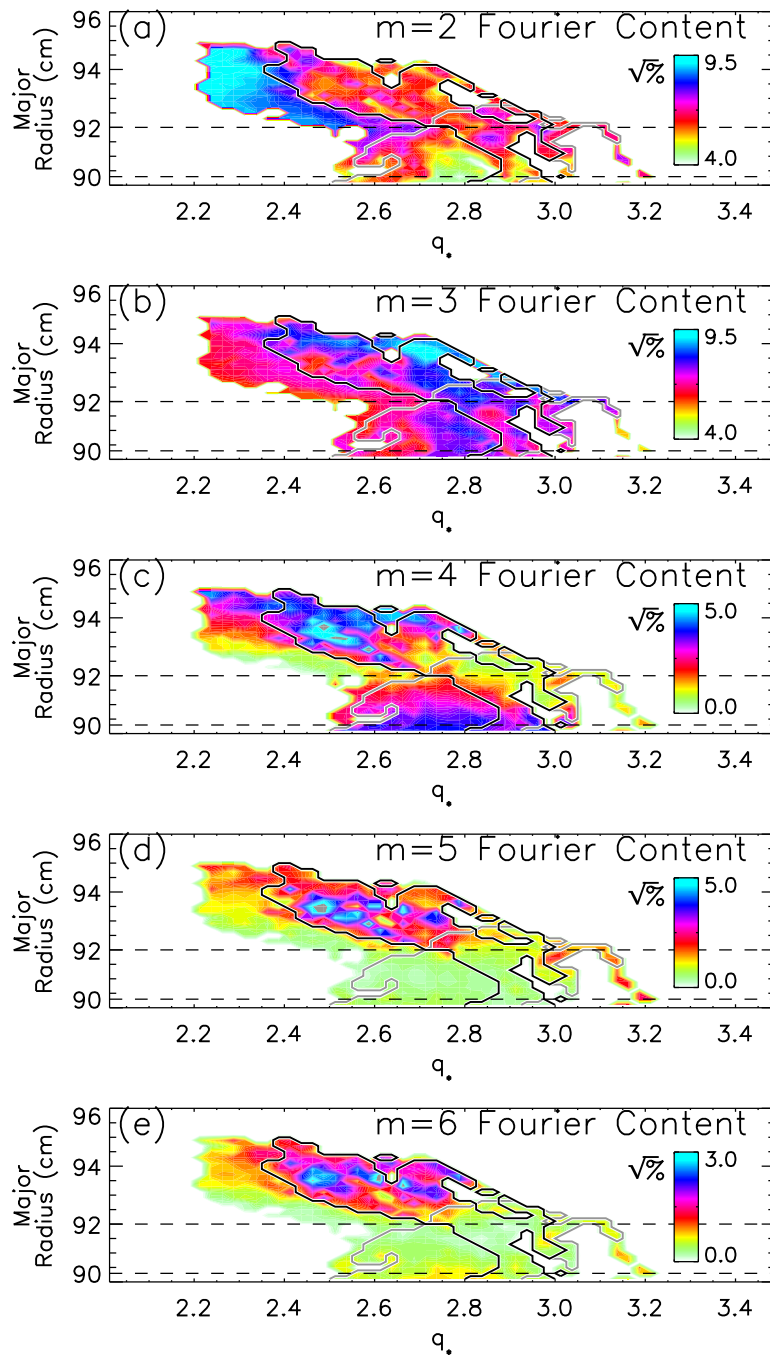
Figure 5.7: Poloidal mode number content in the dominant mode pair for discharges approaching $q_* = 3$ from below. Note that zero is suppressed in the $m = 2$ and $m = 3$ plots for better dynamic range.
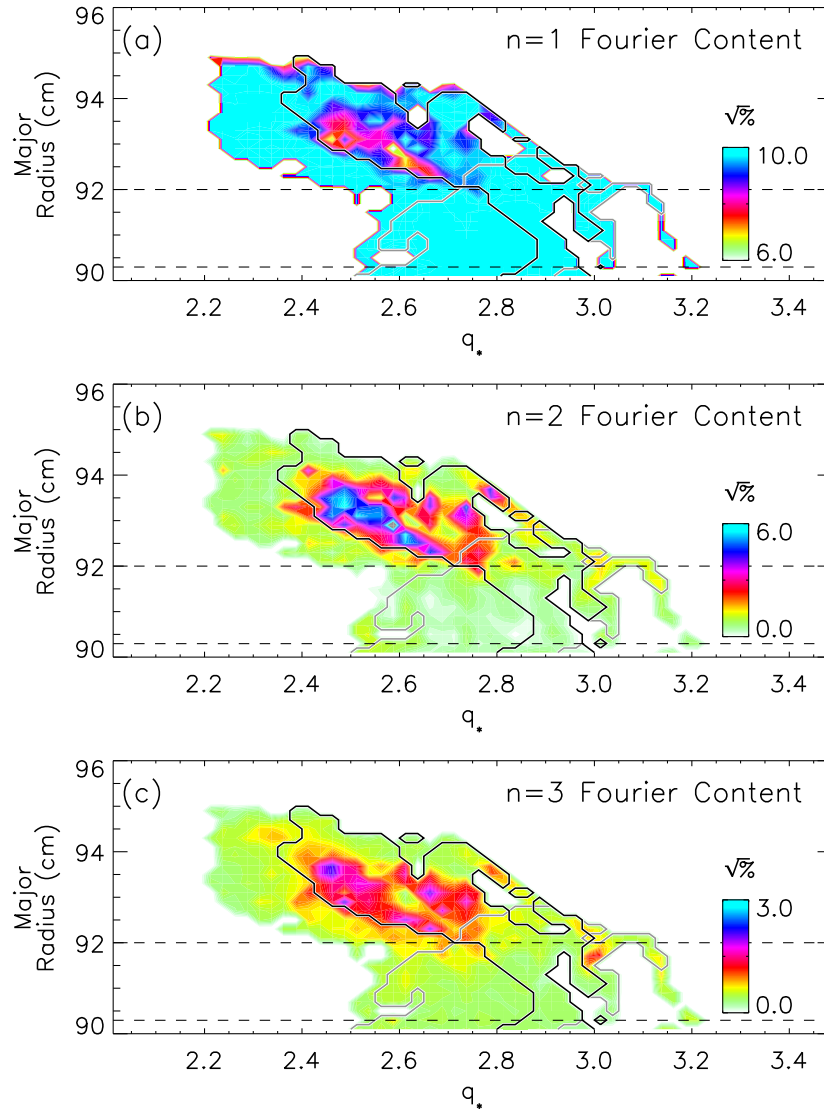
Figure 5.8: Toroidal mode number content in the dominant mode pair for discharges approaching $q_* = 3$ from below.

demonstrates the importance of separating out $R_0$ effects when considering the dependence of mode amplitude on $q_*$.

For $R_0 < 92\ cm$, a $q_*$ dependence can be seen for the first and second BD mode pair amplitudes. Both modes become larger as $q_*$ decreases from $\sim 3.0$ to 2.6. This can also be seen in Figure 5.9, where amplitudes of the first mode have been averaged for 91–92 cm major radii. Relative amplitudes of the modes remain fixed though, as Figure 5.6(c) shows no discernible $q_*$ dependence for $R_0 < 92\ cm$, with the possible exception of stronger secondary modes near $q_* = 3$. There is
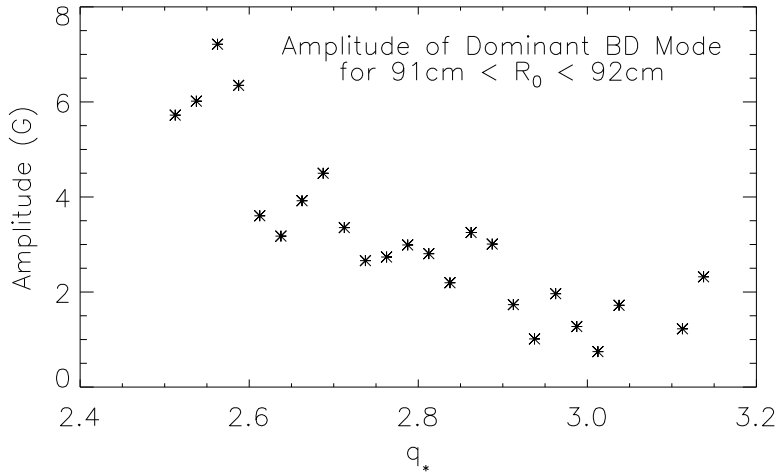
Figure 5.9: Amplitude of the dominant BD mode pair for low-$q$ equilibria with $91\ cm < R_0 < 92\ cm$. This emphasizes the $q_*$ dependence seen in Figure 5.6(a).

a similar increase in mode amplitudes for $R_0 > 92\ cm$ and $q_* < 2.5$, but this is attributed to 2/1 tearing mode activity, as corroborated by Figure 5.7(a).

Strong modes where $R_0 \gtrsim 93.5\ cm$ are often present at the end of the plasma startup period. When $q_* < 2.4$, these initial modes persist as 2/1 tearing modes. The small region of 3/1 activity near $q_* \approx 2.7$, $R_0 \approx 94\ cm$ has been termed the "early mode," which will be discussed in Section 5.4. The early mode typically decays away within 1 ms for shots in this database. For shots where $R_0$ decreases too quickly to be included in this database, the 3/1 early mode persists while $q_*$ rises above 3. Discharges where the early mode persists typically lasted half as long, and were too different to be included.

Figure 5.6(c) suggests that the second BD mode pair is most significant for $2.4 < q_* < 2.7$ when $R_0 > 92\ cm$. Most shots passing through this region have lower-amplitude mode activity relative to earlier or later within the shot. An example is seen in Figure 5.2(c-d), where fluctuations are weaker during 3–4 ms. The $n = 1$ activity is lower during this time, but $n = 2$ activity is about the same, which increases the amplitude ratio. Figure 5.8 shows that $n \geq 2$ Fourier content in the first BD mode pair is highest in this region; however, this does *not* mean that the $n = 2$ mode is larger here than in other regions – it means that modes which are present *look more like* $n = 2$, even if they are low amplitude. Given the value of $q_*$, it's likely that the dominant mode activity is $m/n = 5/2$ in this region. Figure 5.7 supports this notion, showing strong poloidal mode numbers between 4 and 6.

## 5.3.2 Crossing $q_* = 3$ from above

When the edge safety factor approaches the $q = 3$ resonance from above, the plasma passes through periods of 3/1 tearing and ideal external kink instability before reaching the RWM. In these cases, a 3/1 mode is often observed to grow and saturate while in the tearing stage. The onset of the RWM is then less obvious, since saturated 3/1 modes typically persist through the three stages without disappearing.

To compare 3/1 mode behavior when approaching the resonance from different directions, the analysis from the previous section was repeated for discharges starting with $q_* \gtrsim 3.3$. Amplitudes of the dominant BD mode pairs, along with their amplitude ratio, are shown for 18 discharges in Figure 5.10. The discharge set has been restricted to shots where $q_*$ decreases monotonically. Fourier spectra of the dominant poloidal and toroidal mode structures are shown in Figure 5.11. An example discharge from this database, shot 70246, is discussed in detail in Section 4.1. The gray outline in each plot indicates the region of overlapping equilibria contained in both the high- and low-$q$ datasets. This is illustrated in Figure 5.12.

Figure 5.11(c) shows that the $m = 4$ poloidal mode number content is largest when $q_*$ is above 3.2. This is the region in which we might expect 4/1 RWMs. As time progresses, both major radius and edge $q$ decrease for these shots. Following a trajectory in the poloidal mode content plots, one can see that the 4/1 mode gives way to a 3/1. This $m = 4 \rightarrow 3$ transition was studied in Section 4.3.

In overlapping regions, the dominant BD mode is generally not as strong when approaching $q_* = 3$ from above. The second mode is stronger for $R_0 > 91.5$ $cm$ and near $(q_* = 3, R_0 \sim 91$ $cm)$, but weaker below $q_* = 2.9$, versus the low-initial-$q$ shots. The second mode's strength *relative* to the first mode is larger for the high-$q$ cases in the overlap region, as shown in Figure 5.13. This implies that the multimode nature of the plasma near $q_* = 3$ is more significant when crossing the resonance from above. In other words, *multimode effects appear more important when the 3/1 mode begins internally, then moves external.* Fourier content in Figure 5.11 shows that high-$q$ cases have more $m \geq 5$, $n \geq 2$ activity, especially $m/n = 6/2$, near $q_* = 3$. Note again that this is Fourier content for the dominant mode only, not the secondary mode.

One might ask if the difference in multimode characteristics for the high- and low-initial-$q$ discharges is due to different plasma conditions propagating from the startup, or if it relates to the equilibrium immediately before mode onset. To help answer this question, a separate shot set was
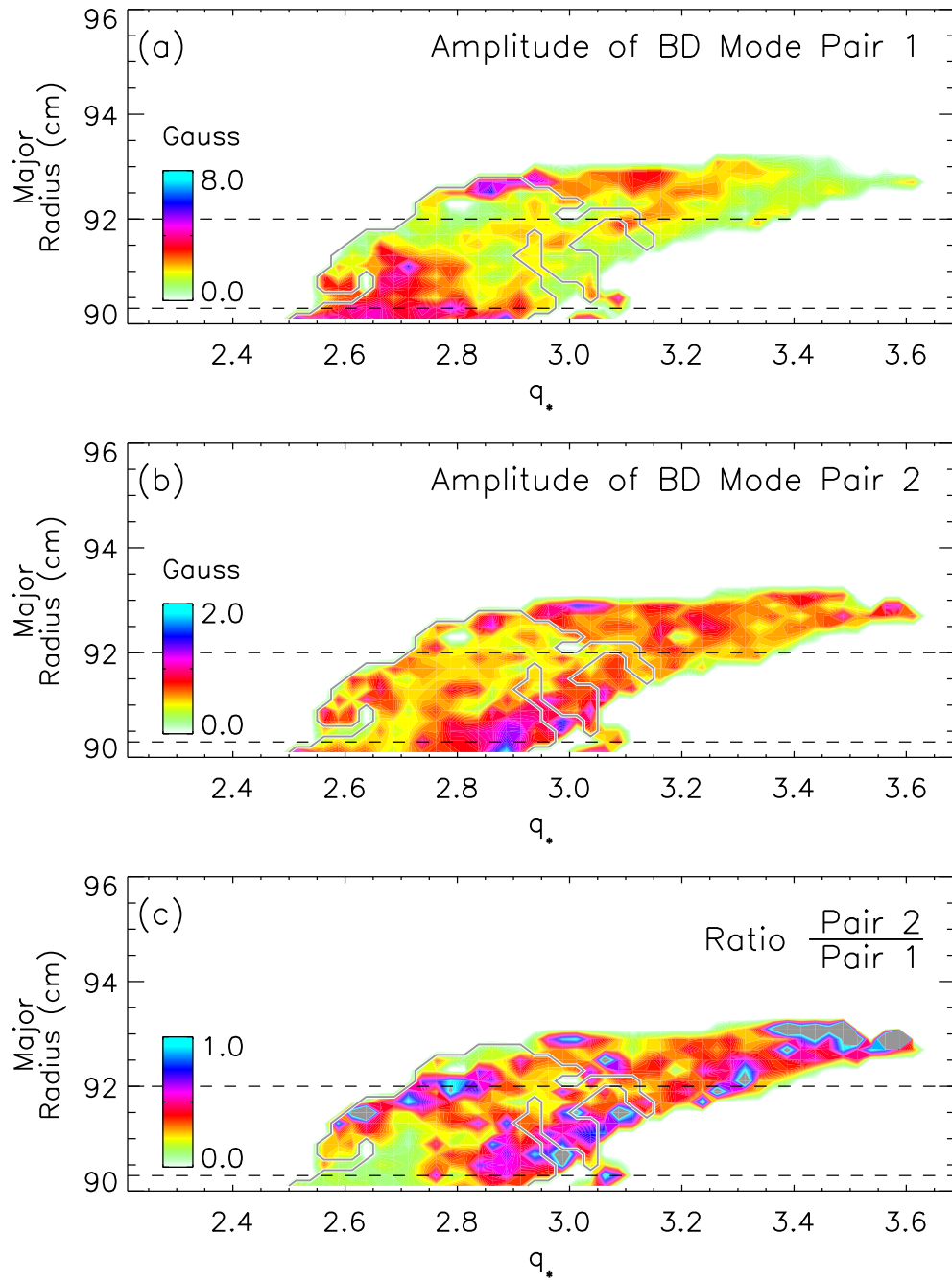
Figure 5.10: Averaged trajectories of 18 shots from high-initial-$q$ experiments, crossing $q_* = 3$ from above, with a monotonic decline in $q_*$. Contours represent mode amplitude for (a) the dominant BD mode pair, (b), the second pair, and (c) the ratio $Pair2/Pair1$. The region outlined in gray is explained in Figure 5.12.
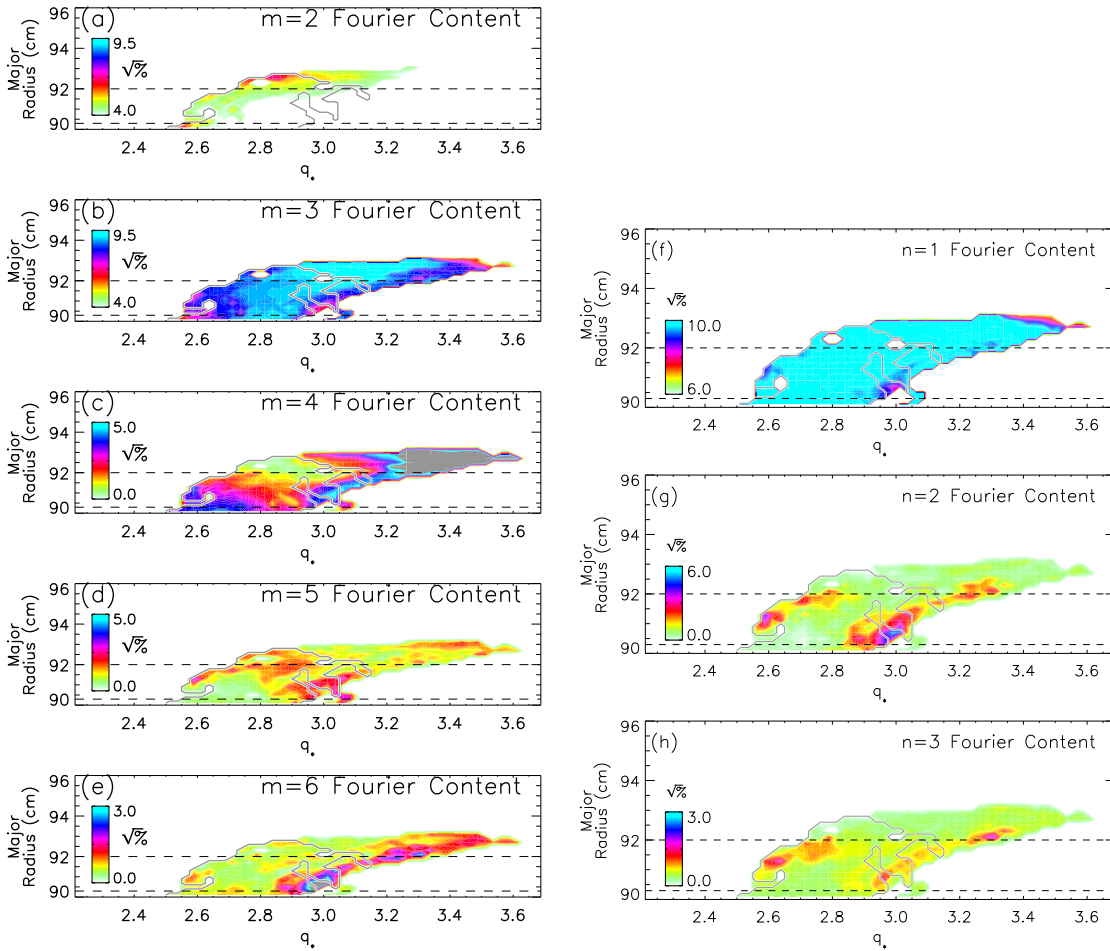
Figure 5.11: Poloidal (a-e) and toroidal (f-h) mode number content in the dominant mode pair for discharges crossing $q_* = 3$ from above.

established where $q_*$ starts above 3, then drops below 3 before rising toward again. This database will be referred to as the "dip" set. A discharge of this type is shown in Figure 5.5.

Repeating statistical analysis on the dip set gives the amplitudes in Figure 5.14. Features of the amplitude ratio in the outlined region of Figure 5.14(c) are similar to those from the low-initial-$q$ discharges. When the $q = 3$ surface starts internal, then is ejected before approaching the plasma edge from outside, mode characteristics as $q_* \to 3$ from below are similar to cases where the resonant surface was external the whole time. When studying external 3/1 mode interactions with other modes later in a discharge, dip-style shots are sufficiently similar to low-initial-$q$ shots to ignore prior 3/1 tearing activity, provided the $q_*$ dips low enough. Fourier content of dip shots is not shown, but is similar to the low-initial-$q$ shots. This result is beneficial for HBT-EP operation, as
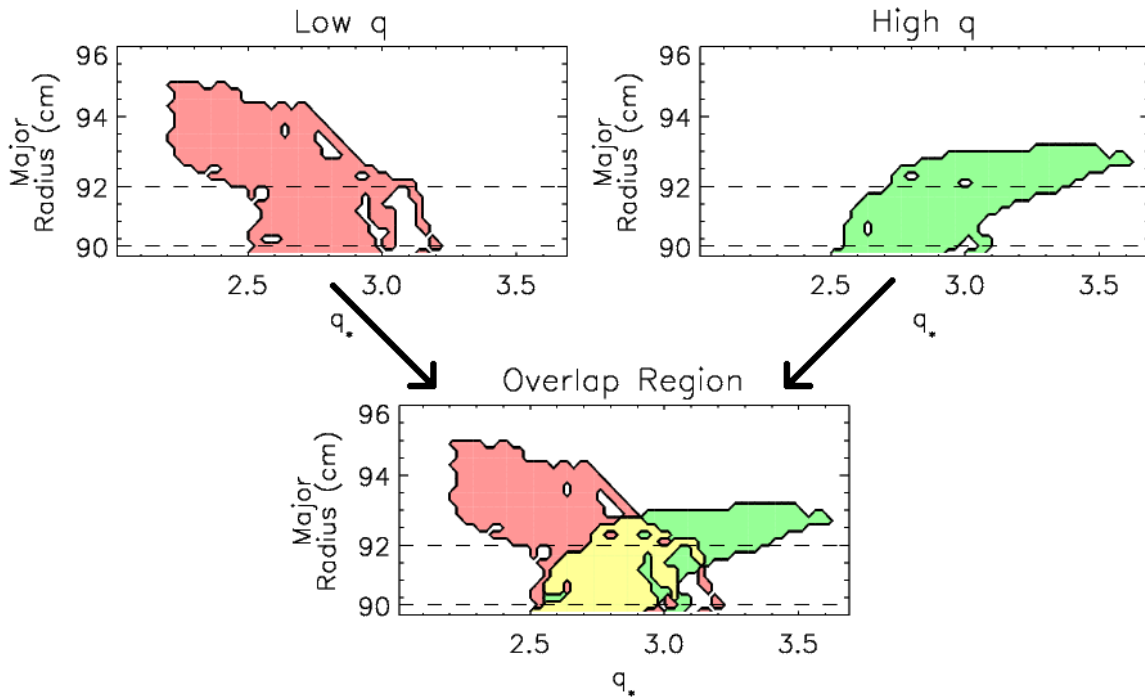
Figure 5.12: Equilibria included in the low-$q$ and high-$q$ discharge sets.  The overlapping region (yellow) is marked in other $R_0$–$q_*$ plots for ease of comparison.
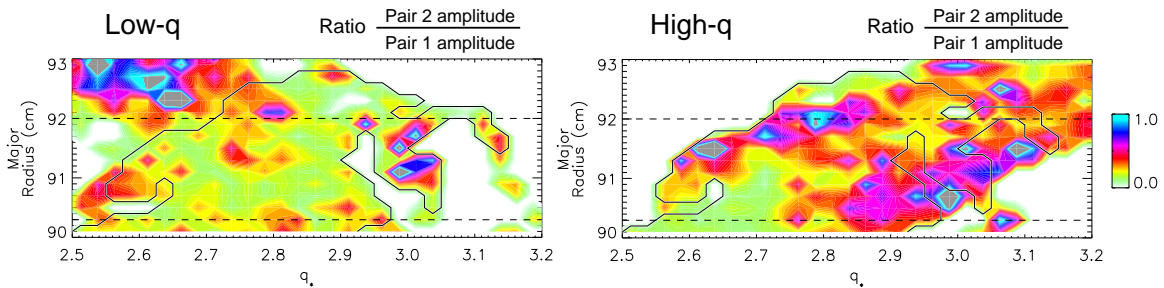


Figure 5.13: Comparison of *secondary/dominant* mode amplitude ratios for low-$q$ and high-$q$ discharges. These plots are subsets of Figures 5.6(c) and 5.10(c), showing only the region with overlapping equilibria. In the overlapping region, high-$q$ discharges have larger ratios on average.

it is easier to achieve reproducible dip-style shots. Figure 5.14(b) shows stronger secondary modes relative to low-$q$ shots when $2.4 < q_* < 2.7$ and $R_0 > 92$ $cm$; poloidal array data suggest this is due to persistent 5/2 modes near the plasma edge.
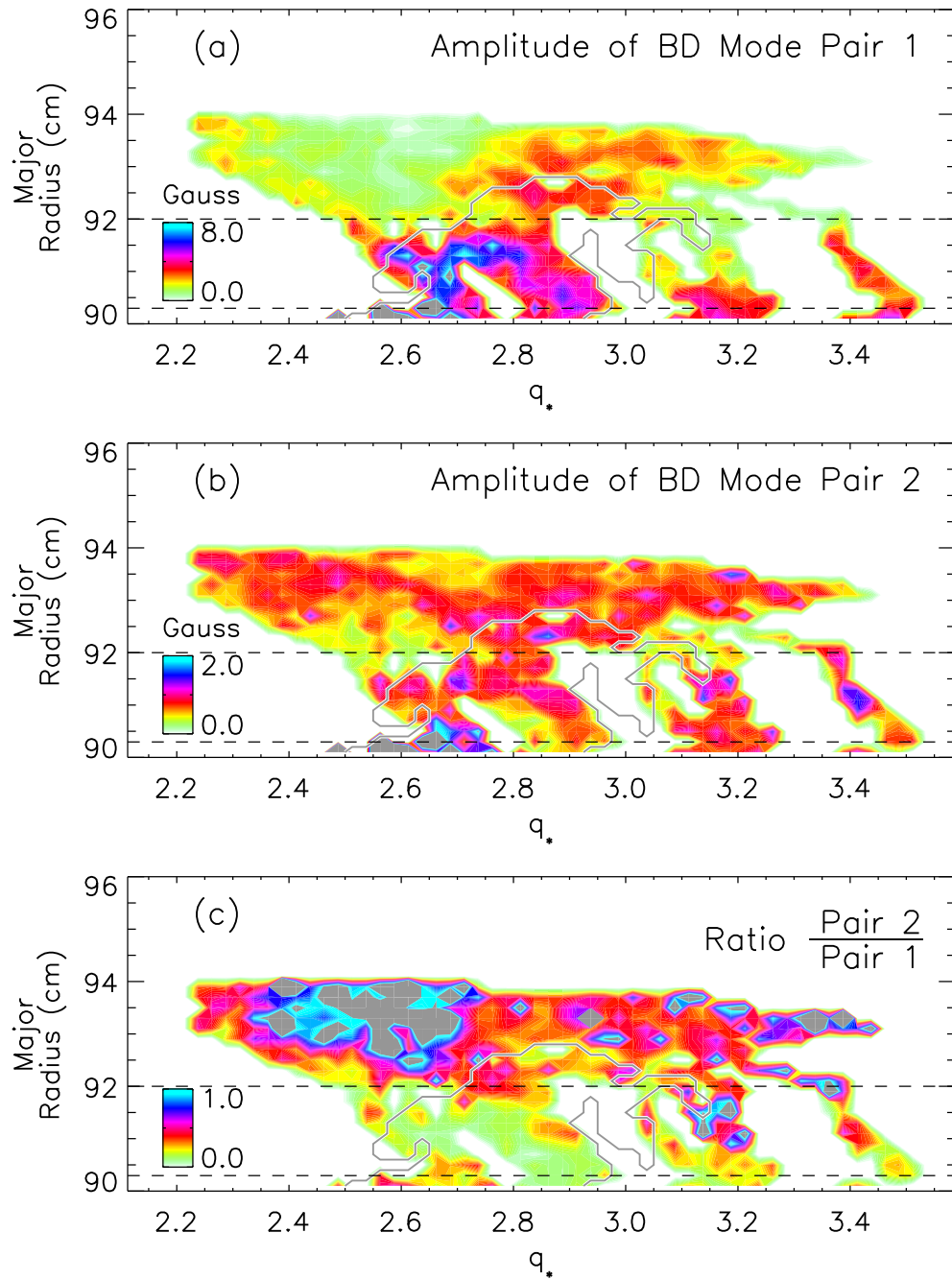
Figure 5.14: Averaged trajectories of 24 shots from high-initial-$q$ experiments which cross $q_* = 3$ from above, then return toward 3 from below. Contours represent mode amplitude for (a) the dominant BD mode pair, (b), the second pair, and (c) the ratio $Pair2/Pair1$. The region outlined in gray is the same as in Figure 5.10.
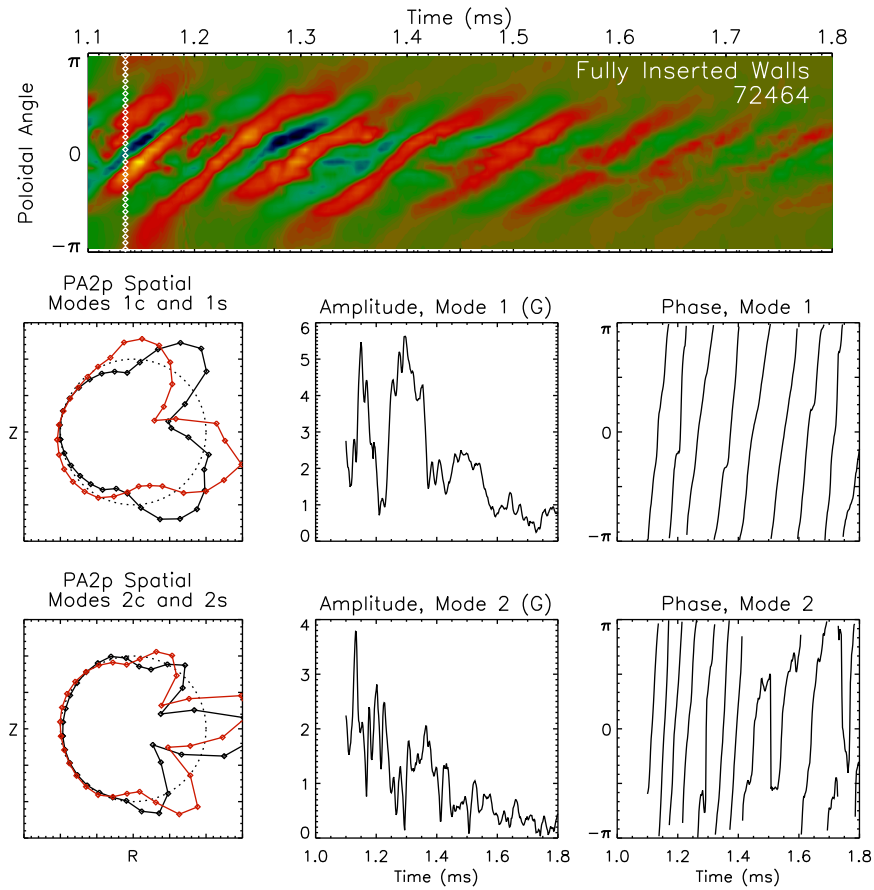
Figure 5.15: The "early mode" for a low-$q$ discharge.

## 5.4   Early modes generated after discharge startup

All of the analysis discussed so far has been for modes existing after 1.5 ms into the shot. However, in many cases there are strong modes that exist prior to 1.5 ms. These have been called "early modes," and may be driven by the large edge current gradient created during the plasma startup. They often decay away within 1 ms as the current gradient relaxes. An example of this mode is shown in Figure 5.15, which has $q_* = 2.65$. Remnants of the early mode are seen at large $R_0$ near $q_* = 2.7$ in Figure 5.4.

Multimode activity is seen during the early mode, but poloidal mode numbers are difficult to determine due to the large major radius. Stronger modes having $\delta B_\theta / B_\theta \sim 10\%$ are seen with asymmetrically retracted walls. This may be caused by reduced wall stabilization, and by non-axisymmetric vertical fields resulting from different soak-throughs with the asymmetric shells. Further study of the early mode is left for future work.

## 5.5   Summary of low- and high-$q$ observations

In the low-$q$ cases, secondary modes were most significant for $2.4 < q_* < 2.7$ when $R_0 > 92$ $cm$. In this region, the $n = 1$ mode was relatively weak, while the $n = 2$ mode had a similar amplitude. The reduced $n = 1$ amplitude and similar $n = 2$ amplitude increased the amplitude ratio. Multimode activity is seen in the "early mode" after discharge startup, and these modes are stronger when several wall sections are retracted.

For discharges with overlapping equilibrium parameters, weaker modes were observed in general for the high-$q$ cases, where the 3/1 mode begins as an internal mode, then is expelled from the plasma. However, multimode effects were more significant in high-$q$ cases, indicated by the secondary mode being strong relative to the primary mode. Note that the multimode shots discussed in Chapter 4 were all of the high-$q$ type.

These results suggest that single-mode-based feedback should be more effective if the target mode is external the whole time – a multimode response is less likely to occur. An important question is how these results apply to diverted plasmas, where all resonances are internal, and many exist in very thin layers near the plasma edge. Future work on HBT-EP will investigate the multimode natural of RWMs in diverted plasmas.

# Chapter 6

# Mode Activity with
# Non-symmetric Walls

One might ask how the structure of kink mode activity in a tokamak changes with the geometry of the conducting wall. This is particularly relevant when a non-symmetric wall is necessary for diagnostic access or heating methods. For instance, large gaps in otherwise symmetric vessel walls are required for plasma heating though neutral beam injection. If introducing a large hole in the conducting wall changes the kink mode structure significantly, feedback systems that are designed based on symmetric walls may fail to suppress modes.

This chapter uses the unique adjustability of the HBT-EP conducting wall to investigate changes in mode activity with non-symmetric wall configurations. Resulting modes are compared against those from the previous chapters, which used HBT-EP's normal symmetric wall. The wall changes imposed have low-order poloidal and toroidal geometry variations in the interest of exciting measurable differences in low $m$- and $n$-number modes.

## 6.1  Kink mode theory with non-axisymmetric walls

Resistive wall mode behavior with varying poloidal [58] and toroidal [59] wall asymmetries has been studied numerically and analytically. In both cases, mode growth rates increase with decreasing wall coverage. Rotational stabilization of the mode also changes – less plasma rotation is needed to

completely stabilize the mode for lesser wall coverage. Poloidal gaps in the wall are more significant on the low-field side for high-$\beta$ plasmas due to the ballooning nature of the mode. At low $\beta$, low-field-side gaps are only slightly more significant than inboard gaps, with the difference being caused by toroidicity. The poloidal asymmetry also changes the instability's poloidal mode number spectrum due to differing eddy-current patterns [58]. The high-resolution poloidal arrays in HBT-EP allow this $m$-spectrum to be experimentally measured in detail with varying poloidal gaps. Effects of poloidal and toroidal wall variations on mode activity were experimentally studied in HBT-EP in the past using Rogowski coils and a poloidal array with $\approx$180° outboard coverage for a previous wall generation [40].

Toroidal wall variations were studied analytically in Reference [59], using a cylindrical geometry and assuming full poloidal wall coverage. To quantify how much of the plasma surface is covered by the conducting wall, we define a fractional wall coverage as

$$f = \frac{A_{wall}}{4\pi^2 bR_0}, \tag{6.1}$$

where $A_{wall}$ is the surface area of the passive stabilizing wall, and $b$ is the wall's minor radius. Here we assume the retracted walls are far enough away from the plasma that their presence is negligible, though this is a very rough approximation for the geometries used in this research. Using this coverage, the resistive wall mode growth rate in the single-mode approximation is

$$\gamma\tau_w^* = \frac{E_{m/n}}{1 - (1 - f)(1 + E_{m/n}/2m)}. \tag{6.2}$$

$E_{m/n}$ is a stability index calculated using the perturbed poloidal flux ($\Psi_{m/n}$) of the mode,

$$E_{m/n} \equiv \left[ r\frac{d\Psi_{m/n}}{dr} \right]_{r_w^-}^{r_w^+} \bigg/ \Psi_{m/n}(r_w) \tag{6.3}$$

where $\left[ \frac{d}{dr} \right]_{r_w^-}^{r_w^+}$ is the jump in the radial derivative across the wall.

In the multimode case, expressions for $\gamma\tau_w^*$ involve more terms which allow coupling between multiple modes [59]. The important feature of Equation 6.2 in the context of this thesis is the dependence of the growth rate on the fractional wall coverage – the RWM growth rate increases as $f$ decreases. Further details of calculating growth rates may be found in References [59] and [40].
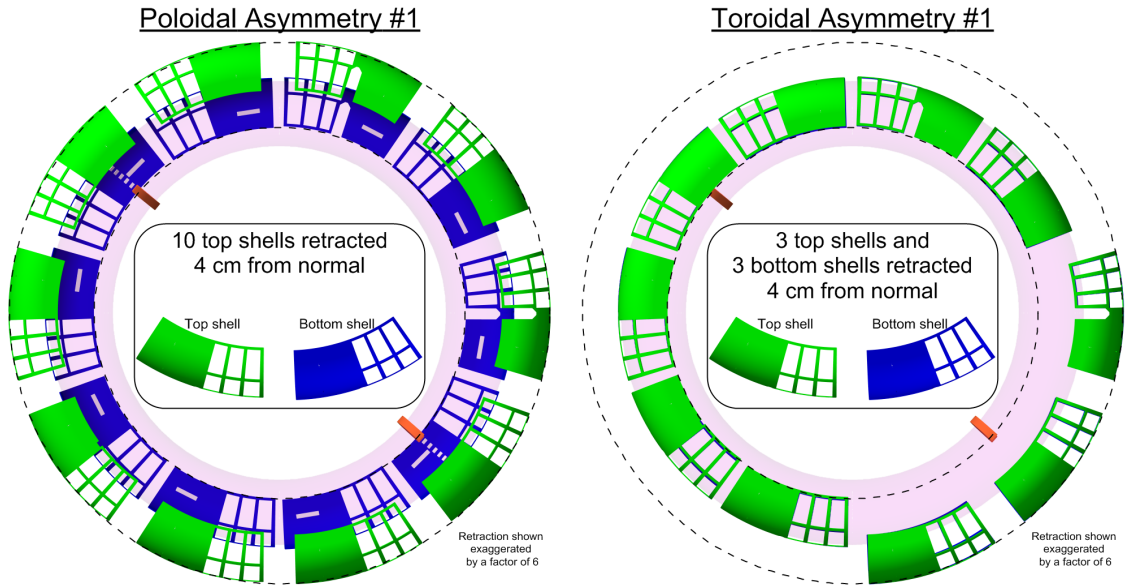
Figure 6.1: Poloidal and toroidal asymmetric wall configurations used for discharges with $q_*$ approaching 3 from above. The poloidal asymmetry had all 10 top shells retracted 4 cm from their usual positions, while the toroidal case had top and bottom shells in 3 sections retracted.

## 6.2 Transitions of m=4 to m=3 modes with asymmetric walls

Several shots were taken with $q_*$ approaching 3 from above with poloidal and toroidal wall asymmetries to study differences in the $m = 4 \rightarrow 3$ transition. The asymmetric wall configurations that were used are shown in Figure 6.1. There were not enough discharges to allow a statistical study, so only the three most similar shots were directly compared – one from each shell configuration. Plasma current, major radius, and edge-q for these shots are shown in Figure 6.2. Decomposing data for 1 ms surrounding when $q_*$ crosses 3 (highlighted region) gives the spatial modes and relative mode powers shown in Figure 6.3. The major radius is relatively constant in the analyzed time interval, which gives confidence in the resulting modes.

The dominant mode pairs have very similar spatial mode shapes for each wall configuration. In the case of the poloidal asymmetry, the spatial modes have lower amplitudes in the upper-right quadrants of Figure 6.3(a-d). This occurs because 9 sensors in each plot have been retracted away from the plasma along with the shells, and measure smaller fluctuation amplitudes. This shows an advantage of using the BD analysis – the dominant mode remains intact instead of being split into several Fourier modes, even though the sensor positions are not specified in the analysis. Spatial modes from poloidal array #1 (not shown) show the same effect for the toroidal asymmetry.
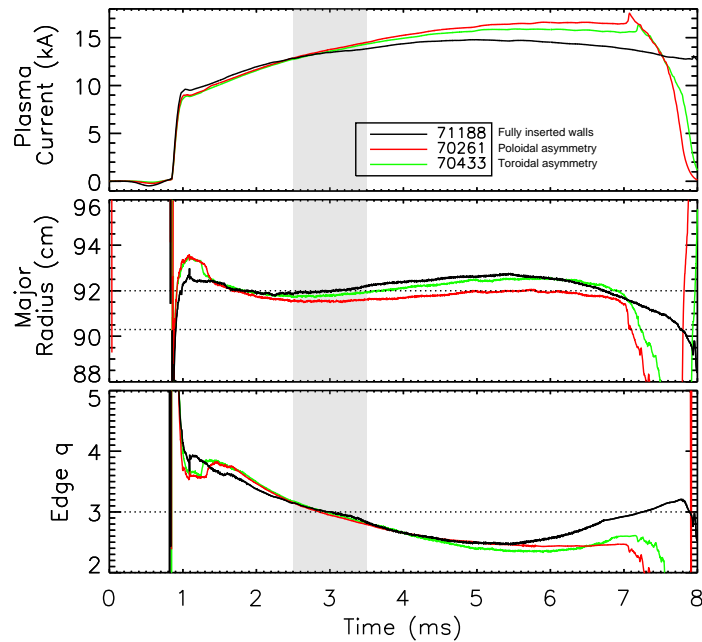
Figure 6.2: Plasma current, major radius, and edge safety factor for three similar shots with different wall configurations. Biorthogonal decomposition results for the highlighted region are shown in Figure 6.3.
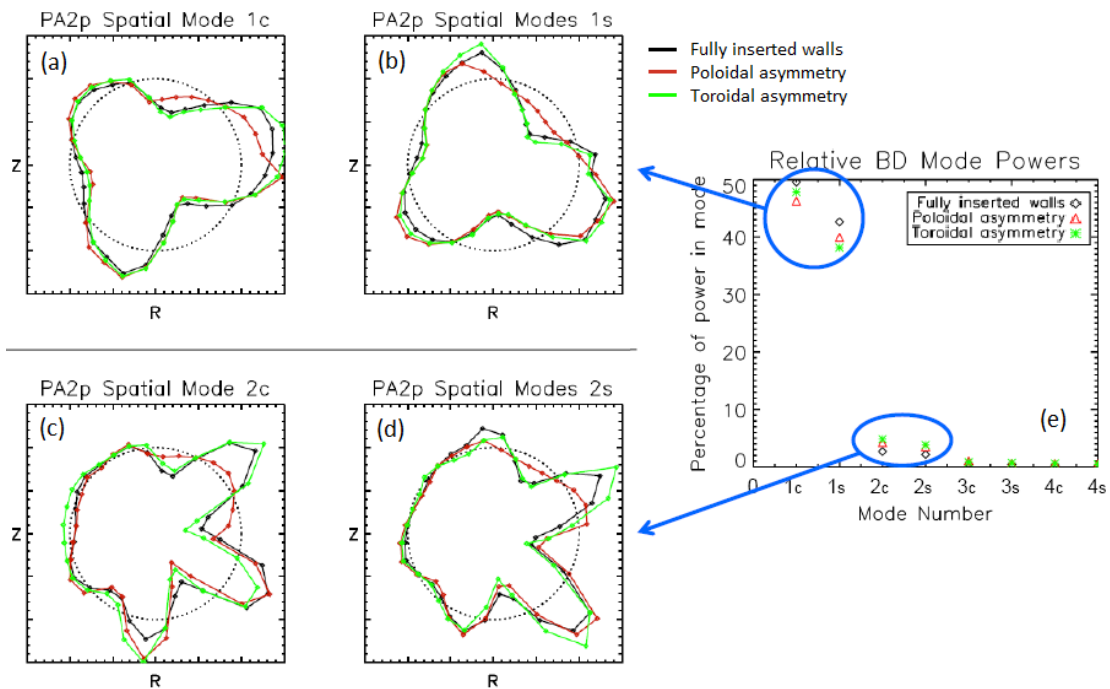


Figure 6.3: (a-d) Spatial modes as seen by poloidal array #2 for three wall configurations. Each wall configuration is shown with a different color. Cosine and sine modes for the first pair are shown in the top row, while the second pair is in the bottom row. (e) Relative power in each BD mode, as defined in Equation 3.3.
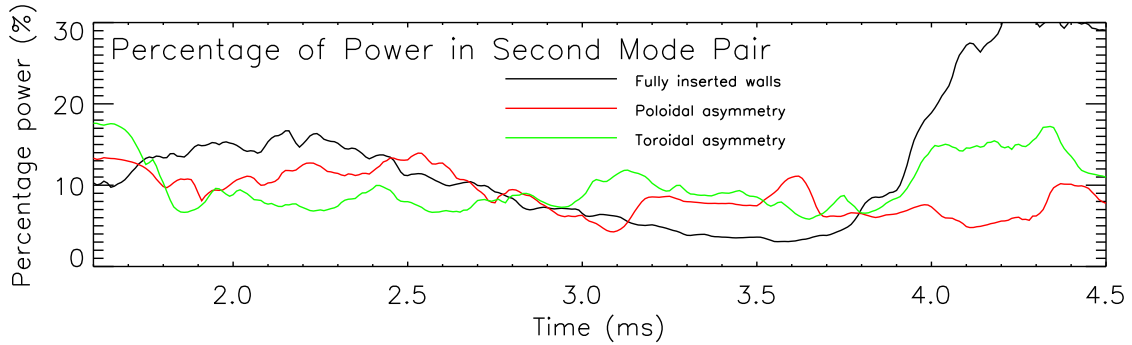
Figure 6.4: Percentage of power in the second BD mode pair for one shot from each of three shell configurations.

The spatial mode shapes are similar, but the *relative powers* in Figure 6.3(e) are different. Relative powers for the secondary modes are larger for the asymmetric cases. This implies that the secondary mode pair is more significant when the walls are non-symmetric. There is large scatter in the mode amplitudes shot-to-shot and within an individual shot, as we have seen in previous chapters, so using the piecewise BD analysis will help show if the result in Figure 6.3(e) is significant. Also, spatial modes from the piecewise BD will show the $m = 4 \rightarrow 3$ transition.

Using 0.5 ms intervals for the piecewise BD gives the secondary mode powers shown in Figure 6.4. Note that these powers are determined by the singular values, which represent averages over 0.5 ms intervals. Between $\sim$3.1 and 3.8 ms, the second mode has a higher relative importance in the asymmetric wall cases versus the normal wall configuration. This is actually caused by the primary mode amplitude being large for the fully inserted walls during this period, while the secondary mode remains small. The results in Figure 6.3(e) were for a 1 ms window ending at $\approx$3.5 ms, which is when the primary mode is large for the fully inserted walls, giving less lower relative power in the second mode. More shots with similar equilibria would be needed to establish statistical significance of the relative mode powers in these cases.

Examining the poloidal mode structure versus edge safety factor for the three shots gives the results in Figure 6.5. The dominant poloidal mode component transitions from $m = 4$ to $m = 3$ at lower $q_*$ values for the asymmetric wall cases. More shots would be needed to decide if this difference is statistically significant, since the spread in transitional $q_*$ values is not known. Plotting the spectra versus time gives similar results, with the $m = 4 \rightarrow 3$ transition happening earliest (highest $q_*$) for the standard shell configuration.
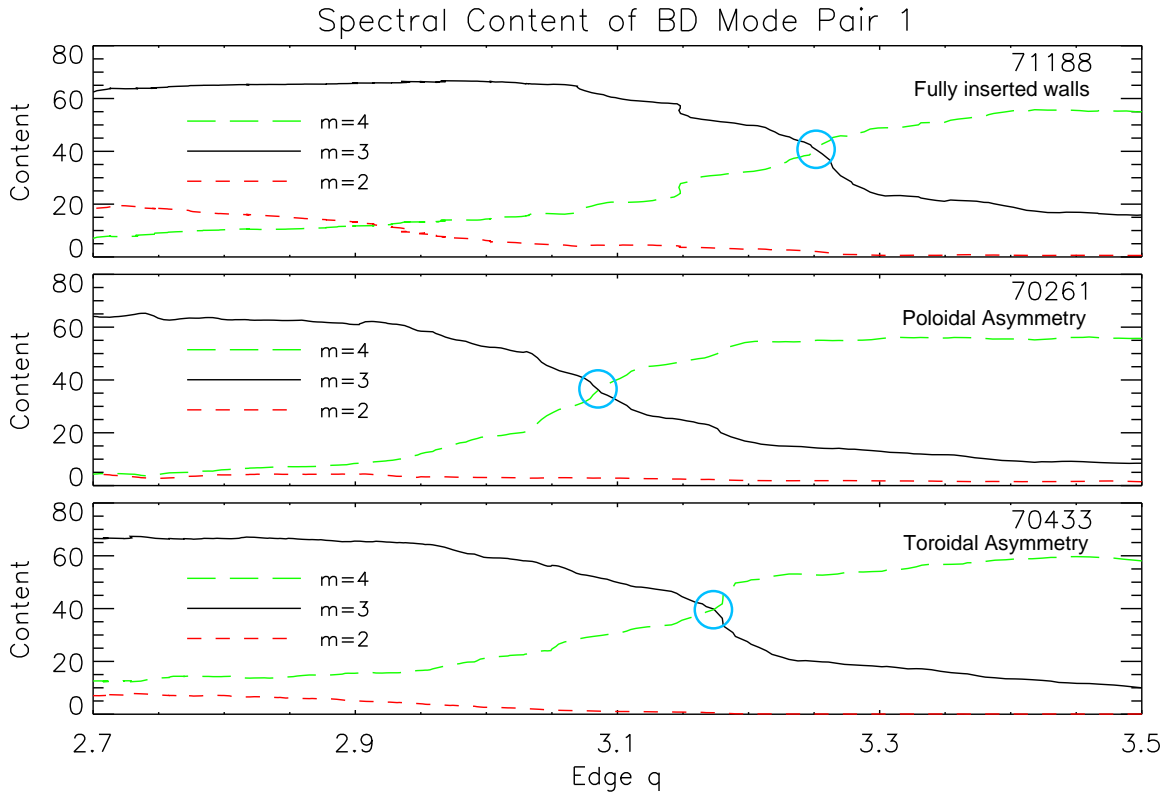
Figure 6.5: Spectral content of the dominant BD mode pair versus $q_*$. Points where the mode transitions from mostly $m = 4$ to $m = 3$ are circled.

## 6.3 Approaching $q_* = 3$ from below

Shell configurations used for the low-initial-$q_*$ discharges are shown in Figure 6.6. Note that these are not the same wall configurations as used in Section 6.2. For these experiments, 8 shells were retracted by 4 cm in each case. Thus the effective wall coverage averaged over the plasma surface, Equation 6.1, is the same for the poloidal and toroidal asymmetries. Shells containing the high-resolution poloidal arrays were not retracted in the interest of keeping the sensors in their original positions, permitting the same poloidal mode number analysis used in Chapter 5.

One consequence of changing the wall configuration was a change in the startup and equilibrium evolution of the plasmas. The achieved low-initial-$q_*$ equilibria in $R_0$–$q_*$ space with each shell configuration are shown in Figure 6.7. The region highlighted in gray was attained in all three wall layouts, and can be directly compared. To ease comparisons, the boundary of this overlapping region is shown in all related low-initial-$q_*$ plots in $R_0$–$q_*$ space. This does not consider differences in plasma pressure or current profiles, however.
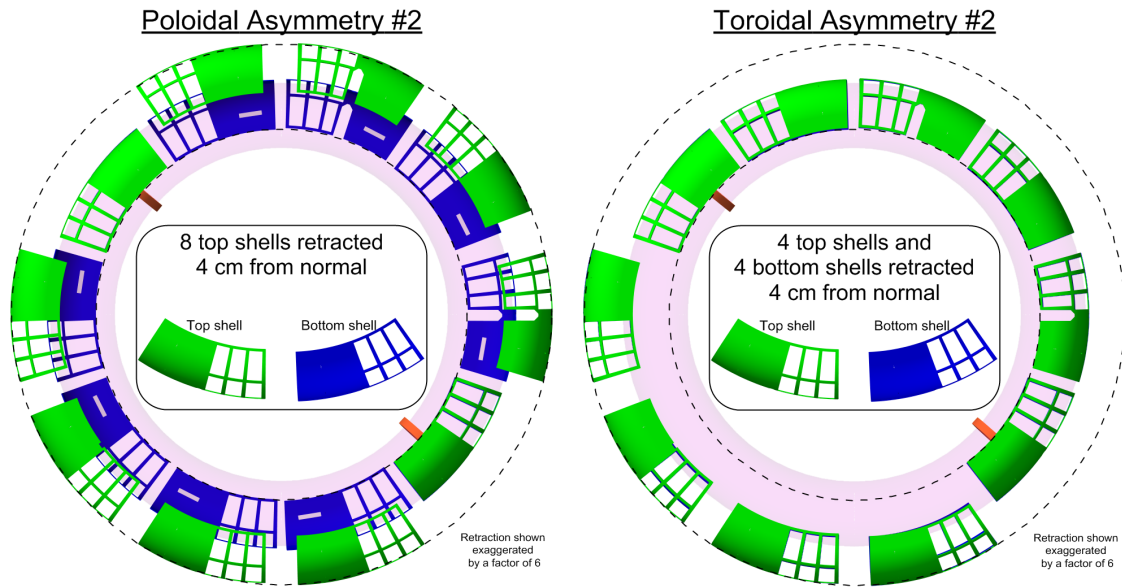
Figure 6.6: Poloidal and $n = odd$ toroidal asymmetric wall configurations used for the low-$q_*$ discharges. The poloidal asymmetry had 8 top shells retracted 4 cm from their usual positions, while the toroidal case had top and bottom shells in 4 sections retracted. High-resolution poloidal array sections were kept fully inserted for diagnostic reasons.
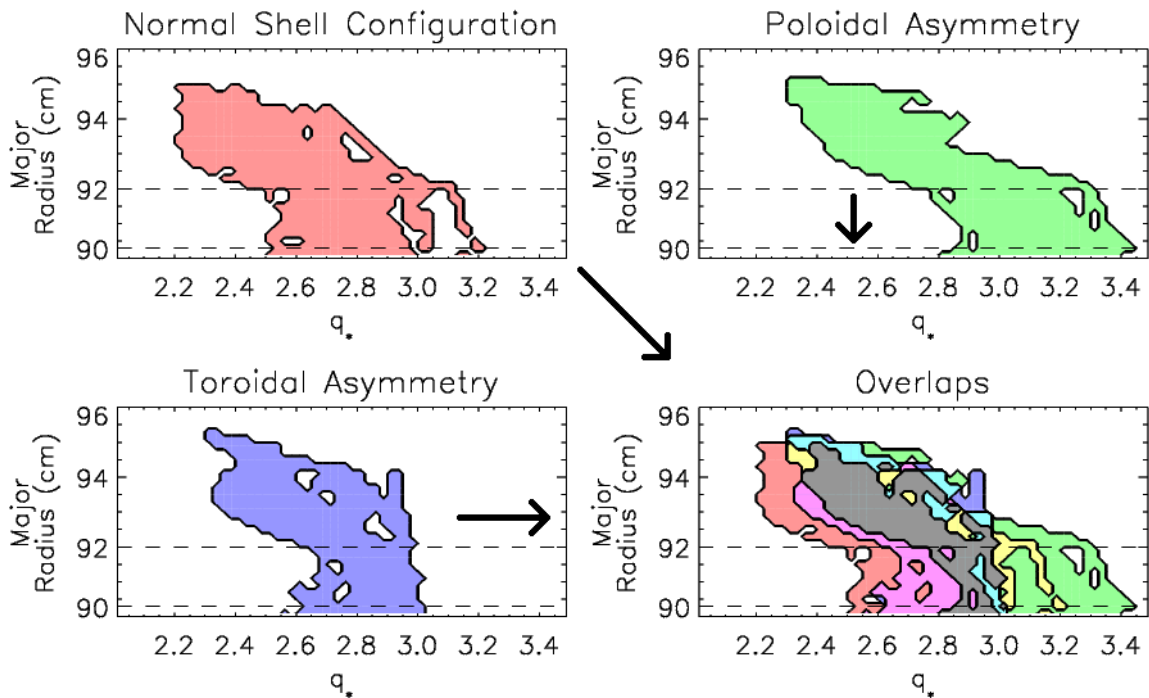


Figure 6.7: Equilibria achieved for three wall configurations in $R_0$–$q_*$ space. The gray region indicates equilibria that were achieved in all three configurations, allowing direct comparison of mode activity. The boundary of the gray region is shown as a black line in related $R_0$–$q_*$ plots to ease comparisons across different wall configurations.
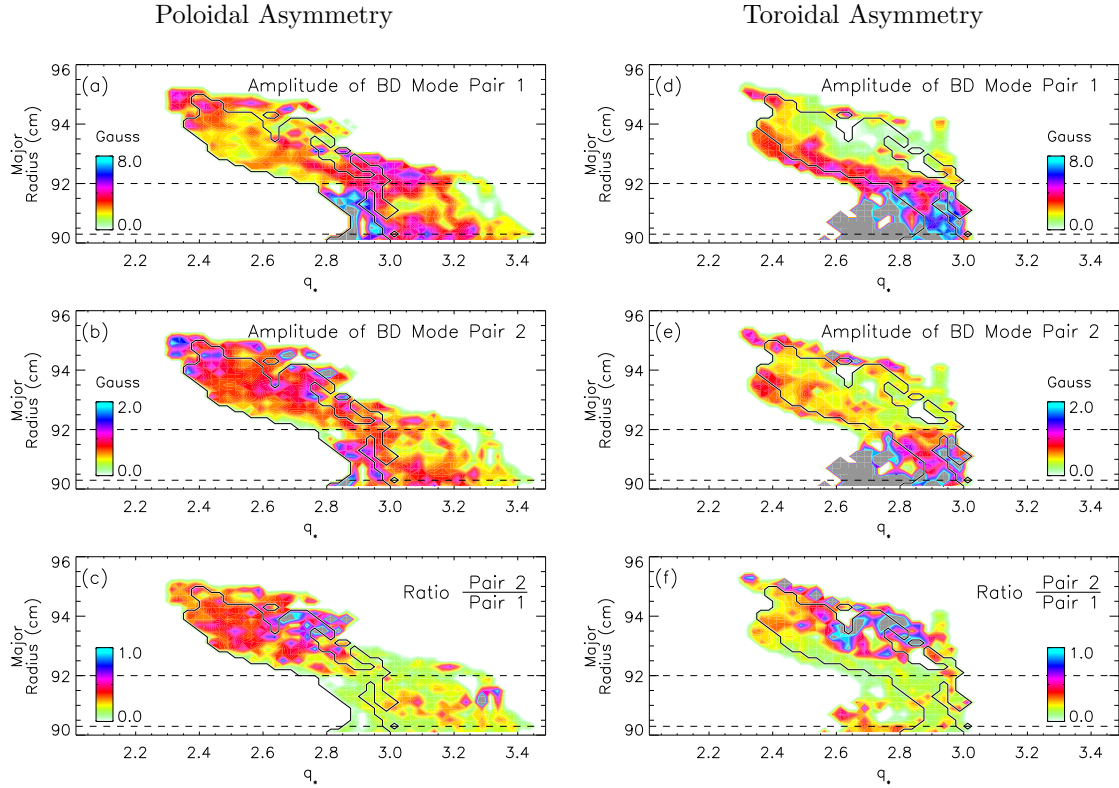
Figure 6.8: Averaged mode amplitudes for the first two BD mode pairs, with poloidal (a-c) and $n = odd$ toroidal (d-f) wall asymmetries. The poloidal asymmetry plots contain 22 shots, while the toroidal asymmetry includes 18 shots.

The same BD analysis from Section 5.3.1 was applied to discharges initializing with $q_* < 3$ when wall asymmetries were introduced. Only sensors which did not move relative to their standard locations were used. Included sensors are the $B_p$ sensors in the poloidal arrays, and all feedback sensors on fully-inserted shell segments – a total of 104 and 107 sensors for the poloidal and $n = odd$ toroidal asymmetries, respectively. Averaging mode amplitudes along trajectories of multiple shots in $R_0$–$q_*$ space gives the results in Figure 6.8. These plots can be directly compared to amplitudes in Figure 5.6 with shells in the standard configuration.

When comparing the overlapping regions of Figure 6.8 to the analogous plots for the standard shell configuration, several differences are apparent. The first BD mode pair is stronger in both asymmetric wall cases versus the fully inserted walls for nearly all $R_0$ and $q_*$ within the common region. The same is true for the second BD mode pair, especially for the poloidal asymmetry when $R_0 > 92$ $cm$. Outside of the triple-overlapping region, the $n = odd$ toroidal asymmetry shows
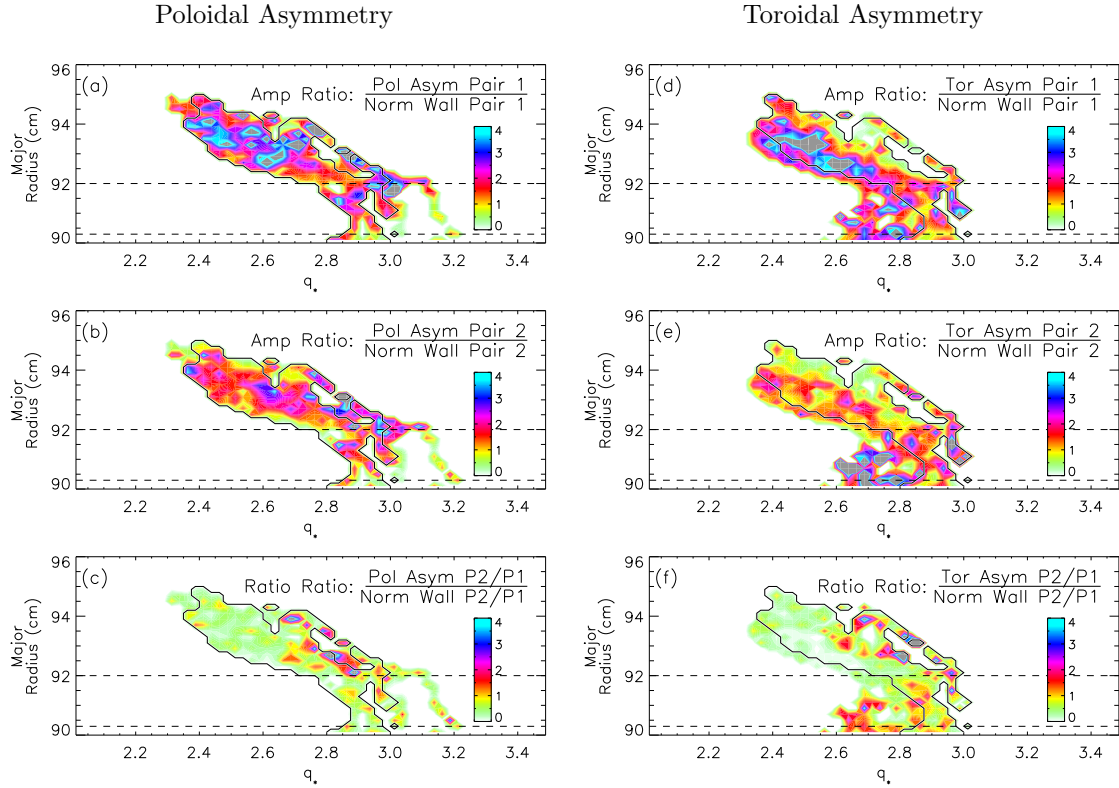
Figure 6.9: Mode amplitudes in the poloidal (a-c) and $n = odd$ toroidal (d-f) asymmetries, relative to amplitudes from the fully-inserted wall configuration. The top two rows are for the first and second mode, while the bottom row is the ratio of *ratios*. The bottom row tells how important the second mode is relative to the first, for the asymmetric cases versus the normal walls.

stronger modes everywhere relative to the axisymmetric walls. These differences are shown clearly in Figure 6.9, where amplitudes from the asymmetric cases have been divided by those from the fully inserted wall configuration. Resulting mode enhancements are likely caused by reduced wall stabilization. From equation 6.2, we should expect larger growth rates when the effective wall coverage is reduced by retracting several shells away from the plasma. Also, strength of the second mode relative to the first when $R_0 > 92$ $cm$ is generally larger for the *fully-inserted* walls, as seen by the low values in Figure 6.9(c,f).

The *trends* of increasing or decreasing mode amplitude versus major radius and edge safety factor are similar for the toroidal asymmetry and normal walls, but with trends shifted to slightly higher $q_*$ for the asymmetric case. Trends look altogether different for the poloidal asymmetry than for the other two cases. Mode strengths do not increase as much with decreasing major radius in the poloidal asymmetry. For the poloidal asymmetry, mode amplitudes decrease with increasing $q_*$
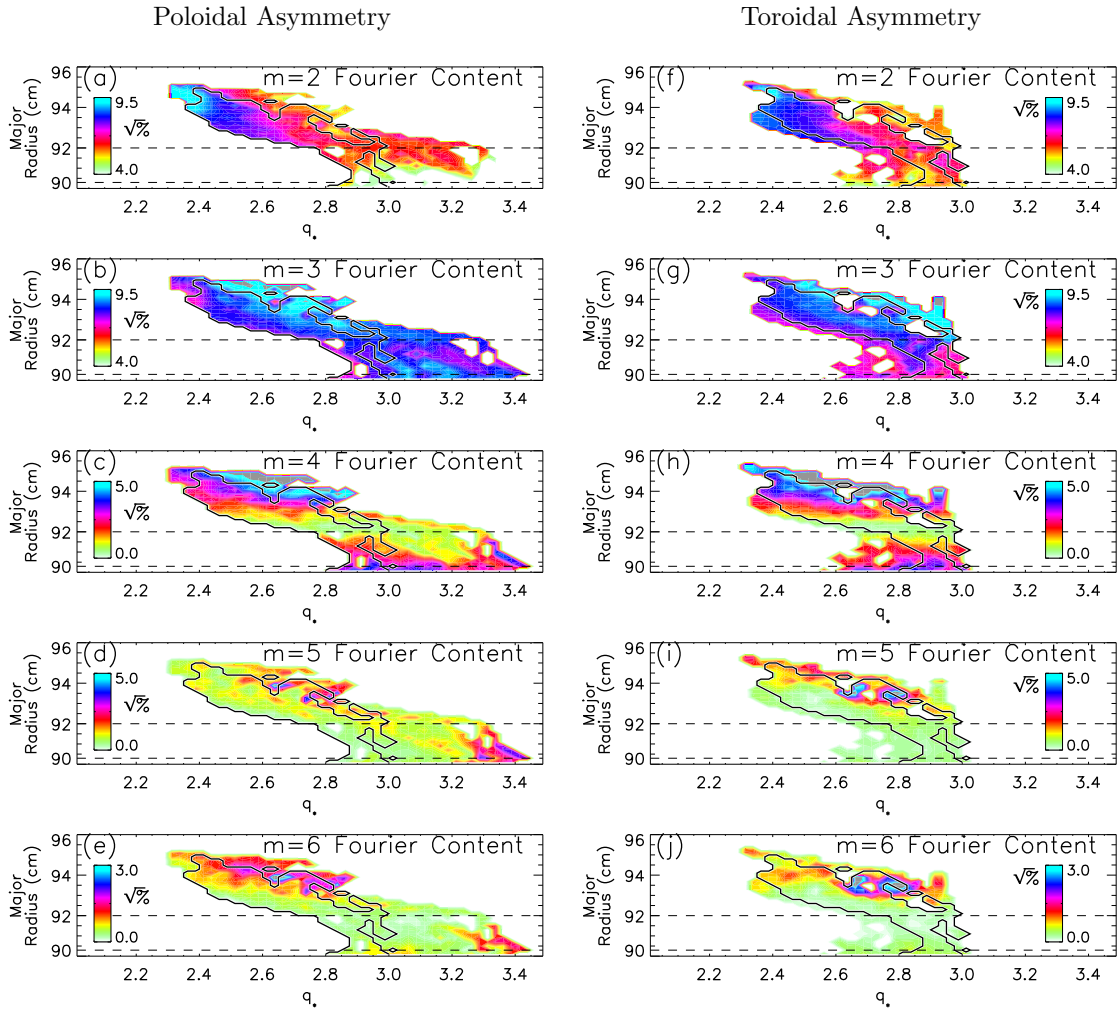
Figure 6.10: Poloidal mode number spectra for the poloidal and toroidal wall asymmetries. Color bars are the same as in the analogous Figure 5.7.

above $q_* = 3$ when $R_0 < 92\ cm$, but this cannot be compared with the other wall cases since there were no similar equilibria. The amplitude ratio is larger in the poloidally asymmetric case near $q_* = 3.3$, but the 3/1 resonant surface is internal here, and sensor contour plots suggest that the $n = 1$ mode is transitioning from $m = 3$ to $m = 4$.

## Spectral content

Figure 6.10 shows the poloidal Fourier content for the poloidal and toroidal shell asymmetries. These can be directly compared with Figure 5.7 which uses the fully-inserted shells. For $R_0 < 92\ cm$, the poloidal mode number content is roughly the same across the three wall configurations. The main

Fully-inserted Walls | Poloidal Asymmetry
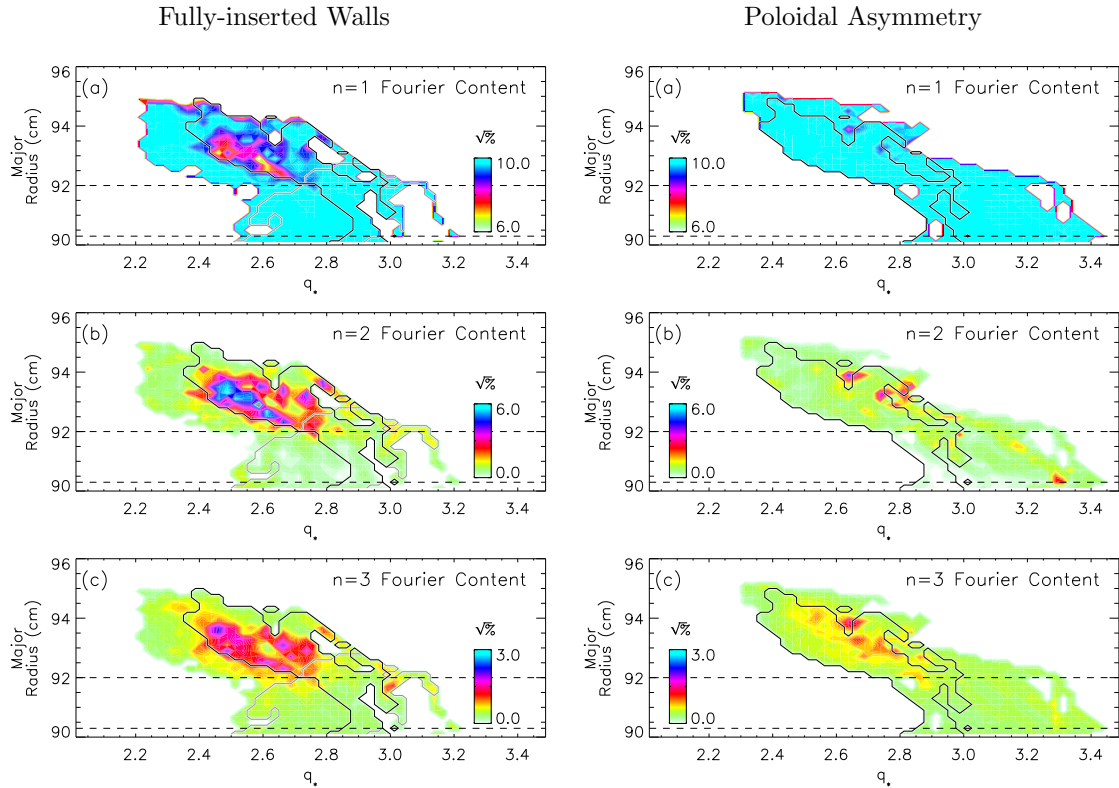


Figure 6.11: Toroidal mode number spectra for the normal fully-inserted walls and the poloidal asymmetry. Plots from Figure 5.8 are repeated here for comparison.

differences appear when examining spectral content for $R_0 > 92\ cm$. In asymmetric cases, the $m = 4 - 6$ activity is shifted to larger $R_0$ relative to the normal walls. There is less higher-order $m$-number activity for $R_0 > 92\ cm$ for asymmetric cases in the overlapping region. Asymmetric walls produce more $m = 2$ and $m = 3$ content for $q_* < 2.7$. The normal shell configuration also has better peaking of the $m = 3$ content near $q_* = 2.8$ across all major radii versus the other cases.

Toroidal mode numbers are compared in Figure 6.11 for the poloidal asymmetry and fully-inserted shells. Poloidal feedback sensors along the bottom shell are used for this analysis. The normal shell configuration produced more $n = 2$ content in the dominant BD mode pair. The poloidally asymmetric shells produced more $n = 1$ content for $q_* < 2.7$ in the overlap region.

For the toroidally asymmetric shells, toroidal mode numbers cannot directly be compared in this analysis due to the exclusion of several sensors. Feedback sensors in 4 chamber sections are ignored for the toroidal asymmetry since they were moved relative to fully-inserted shells. Instead, the toroidal array sensors can be used for $n$ information in all three cases since these sensors are
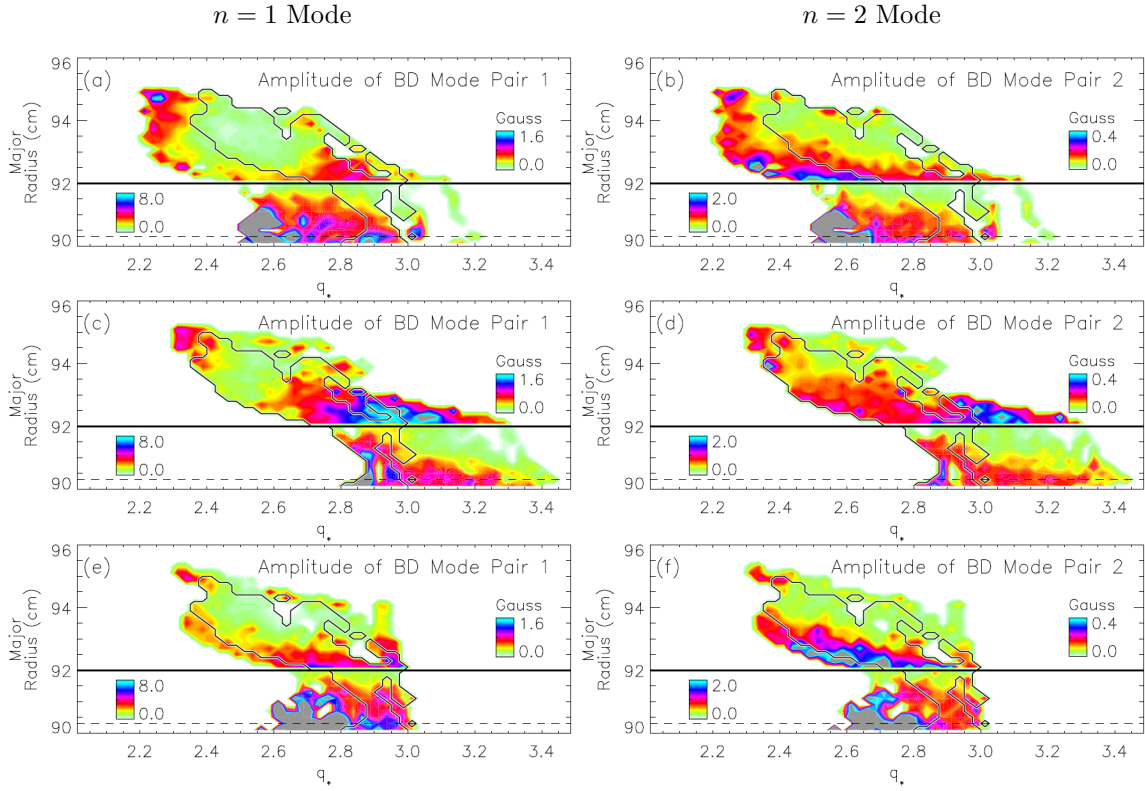
Figure 6.12: Amplitudes of the $n = 1$ ($1^{st}$ column) and $n = 2$ ($2^{nd}$ column) modes using biorthogonal decomposition with only the toroidal array sensors. Rows show the fully-inserted walls, poloidal asymmetry, and $n = odd$ toroidal asymmetry in order. Note that the color bars are different above and below $R_0 = 92\ cm$ due to the reduced TA coupling for $R_0 > 92\ cm$.

fixed in place. However, since the plasma is outboard limited for the majority of each discharge, the TA signals are relatively weak compared to other sensors. This will cause the TA signals to have a lesser impact on the BD modes when all sensors are included. In order to enhance the sensitivity to modes seen by the toroidal array, the BD analysis was repeated using only TA sensors. Resulting amplitudes for the $n = 1$ and $n = 2$ modes are shown in Figure 6.12 for the three shell configurations.

All toroidal mode amplitudes strongly depend on major radius since the toroidal array is located near the high-field-side midplane. Again, the poloidal and toroidal asymmetries produce larger mode amplitudes versus the fully-inserted shells in overlapping regions, in agreement with Figure 6.9. Relative amplitudes of the $n = 2$ versus $n = 1$ modes are shown in Figure 6.13. The $n = 2$ mode appears more prominent for $q_* < 2.65$, which may be attributed to 5/2 activity. The poloidal asymmetry has slightly less relative $n = 2$ amplitude for $2.7 < q_* < 3.0$, but otherwise the different cases look statistically very similar in overlapping regions. This suggests that the wall changes did
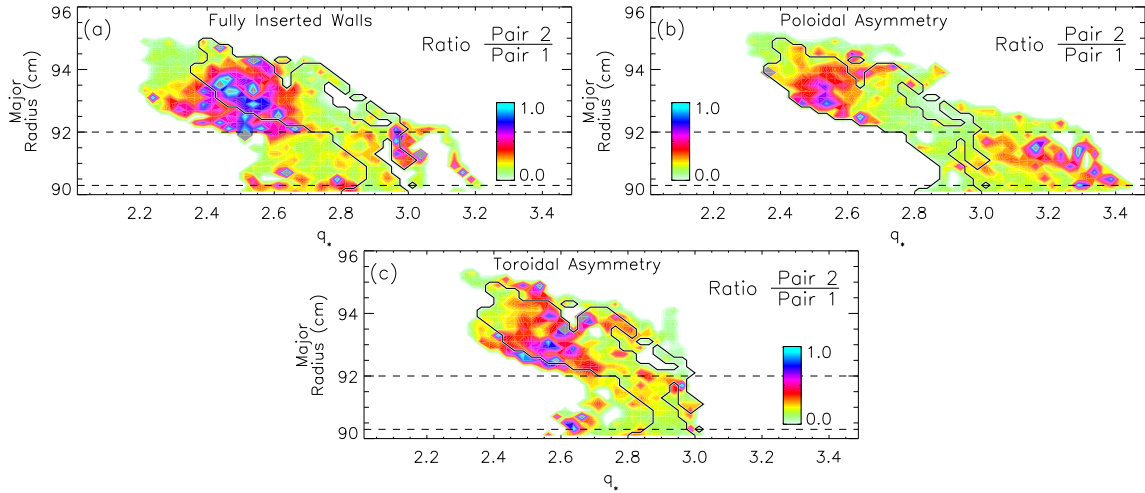
Figure 6.13: Ratios for $(n = 2)/(n = 1)$ mode amplitudes for the three shell configurations, using only toroidal array sensors in the BD.

not significantly affect the relative toroidal mode number content when comparing $n = 1$ and $n = 2$ modes – amplitudes rose fairly uniformly across mode numbers with retracted shells.

## Implications of spectral changes due to changing the wall geometry

For both asymmetric wall cases tested, changing the wall geometry affected relative $m$-spectra, but not $n$-spectra, of the modes. This has important implications for projecting the performance of active magnetic feedback systems when a tokamak's conducting wall is changed, for instance when adding a port.

If a feedback system is designed with only $n$-resolution, such as the DIII-D external coil (C-coil) system [60] and the NSTX RWM coils [35], then there shouldn't be drastic reductions in feedback performance as the walls change. Reducing the effective wall coverage will increase mode growth rates, and will therefore increase necessary feedback power, but the toroidal spectrum is still unchanged. A different $m$-spectrum will change the amount of flux that the control coils can put in to a given mode, but the original $n$-resolution will still be sufficient.

For a feedback system that includes $m$-resolution, such as HBT-EP's active coils and DIII-D's internal coils (I-coils) [61, 62], the changes to the poloidal mode spectrum induced by wall changes could make a difference. Each $m$-number will couple to the active coils differently for their various poloidal locations. A change in the wall could affect the optimal coil angles for a given mode. In HBT-EP, the control coils move along with the wall, so the situation is more complicated.

It is important to note that these experiments only considered changes in the plasma's major radius and $q_*$ resonance condition. Changes in $\beta$ which are responsible for pressure-driven kink modes could affect mode spectra in a different way. High-$\beta$ modes have a ballooning character, and will have different $m$ distortions for similar wall changes. Distortions of poloidal mode structure, causing "bulging" through a midplane gap in passive stabilizing plates, has been inferred in high-$\beta$ cases in NSTX [47].

### 6.3.1 *Odd* versus *even* toroidal wall asymmetry

To examine possible changes in mode structure due to differences in the toroidal structure of the wall, several shots were taken with an $n = even$ wall in addition to the $n = odd$ wall. These two wall configurations are shown in Figure 6.14. In each case, 8 of the shell segments (4 top, 4 bottom) were pulled back to a distance of 5 cm from the plasma surface. Figure 6.15 shows plasma parameters for a shot from each wall arrangement, which overlay very well. Since the measured equilibria are very similar, a direct comparison of mode structures and amplitudes versus time is appropriate for these two shots.
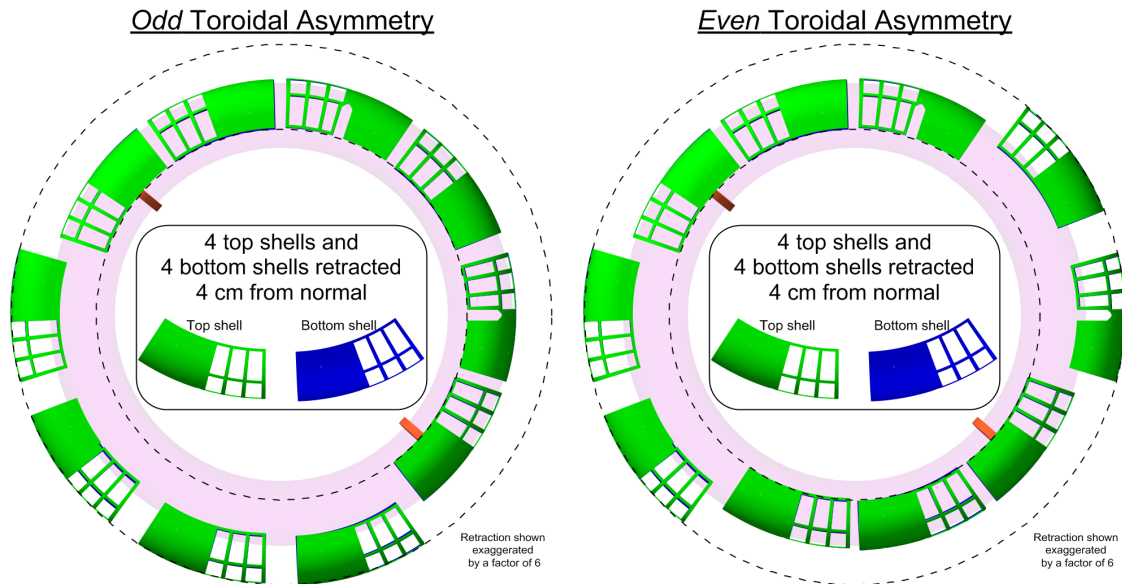


Figure 6.14: *Odd* and *even* toroidal wall asymmetries. Both cases had top and bottom shells in 4 sections retracted 4 cm from their usual positions. High-resolution poloidal array sections were kept fully inserted for diagnostic reasons.
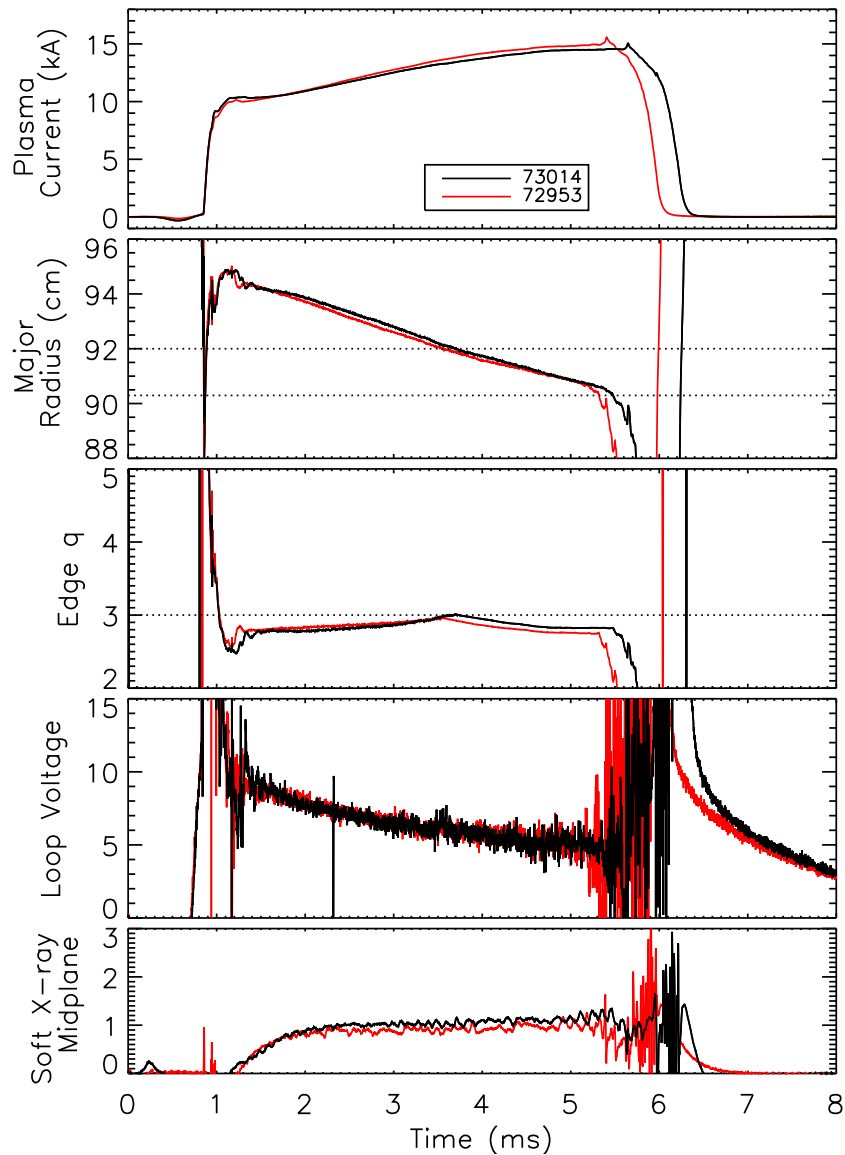
Figure 6.15: Plasma parameters for two shots from the toroidal wall asymmetry experiments. Shot 72953 (red) has an $n = odd$ wall, while 73014 (black) has an $n = even$ wall.

In each case, biorthogonal decomposition was done using only the sensors which were not moved along with shells. For the $n = even$ case, the 32 feedback sensors in chamber sections 4, 5, 9, and 10 were removed from the analysis. For the $n = odd$ case, the 32 feedback sensors in chamber sections 1, 2, 9, and 10 were ignored. Neither case has a complete toroidal set of undisturbed feedback sensors. In order to have a uniform measurement set in the toroidal direction, comparison was done using the toroidal array sensors.
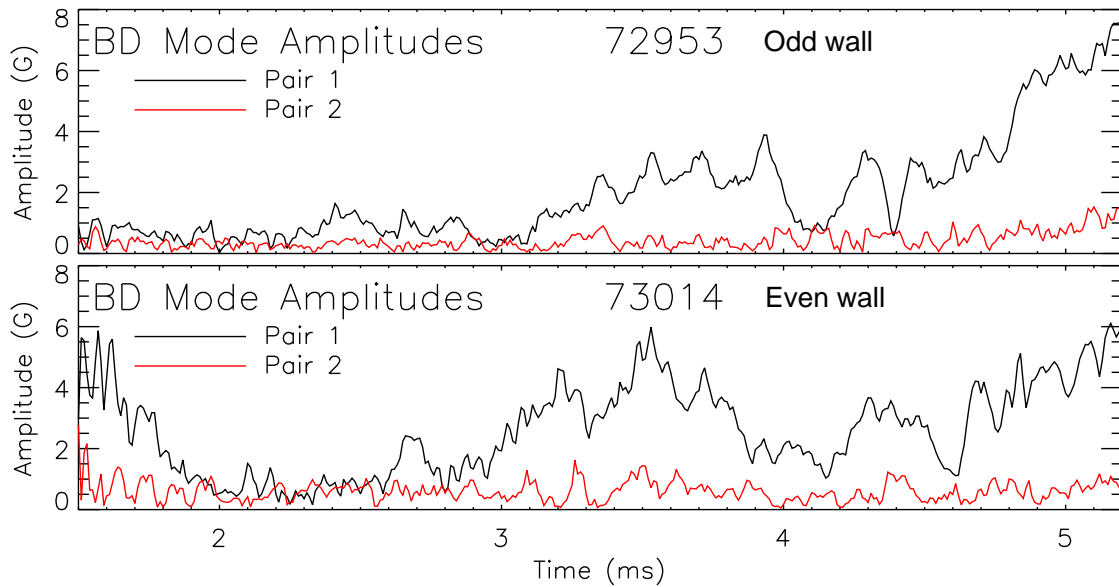
Figure 6.16: Amplitudes of the two most-significant BD mode pairs for an $n = odd$ wall (72953) and an $n = even$ wall (73014) shot. Each point represents the amplitude of the BD mode pair calculated by using data from the previous 0.5 ms, per Equation 4.2.

Piecewise BD analysis with 0.5 ms time intervals for the shots in Figure 6.15 provides the mode amplitudes in Figure 6.16. Amplitudes of the dominant mode pairs are similar in each shot, and differences are within typical shot-to-shot variation.

Spatial mode structures were analyzed during the 4.3–5.2 ms period, when the plasma is well-centered in the poloidal array sets. This is also when the plasma is closer to the toroidal array sensors, providing larger $\delta B$ signals from the modes. Figures 6.17 and 6.18 show spatial mode structures from analyzing 0.5 ms intervals separated by 0.1 ms. These figures have the same layout as Figure 4.7, but show the toroidal array instead of feedback sensors for $n$ information. Here the gray lines show the spatial amplitude of each mode pair. The stronger apparent amplitude at $\phi = 200°$ is due to one sensor having a higher sensitivity – it has larger amplitudes in all shots. The increased sensitivity may be from a slight gain miscalibration, or from the sensor being closer to the plasma.

The spatial amplitudes show that the $n = 1$ mode is uniform in the toroidal direction for both wall configurations. There is no evidence of "bulging" into toroidal gaps for the dominant mode pair. This bulging would be evident if the spatial amplitude was larger in given toroidal sections, as long as the bulging was proportional to the dominant mode amplitude. If the bulging is not tied to the dominant mode amplitude,then it will appear as a different BD mode when the temporal evolution
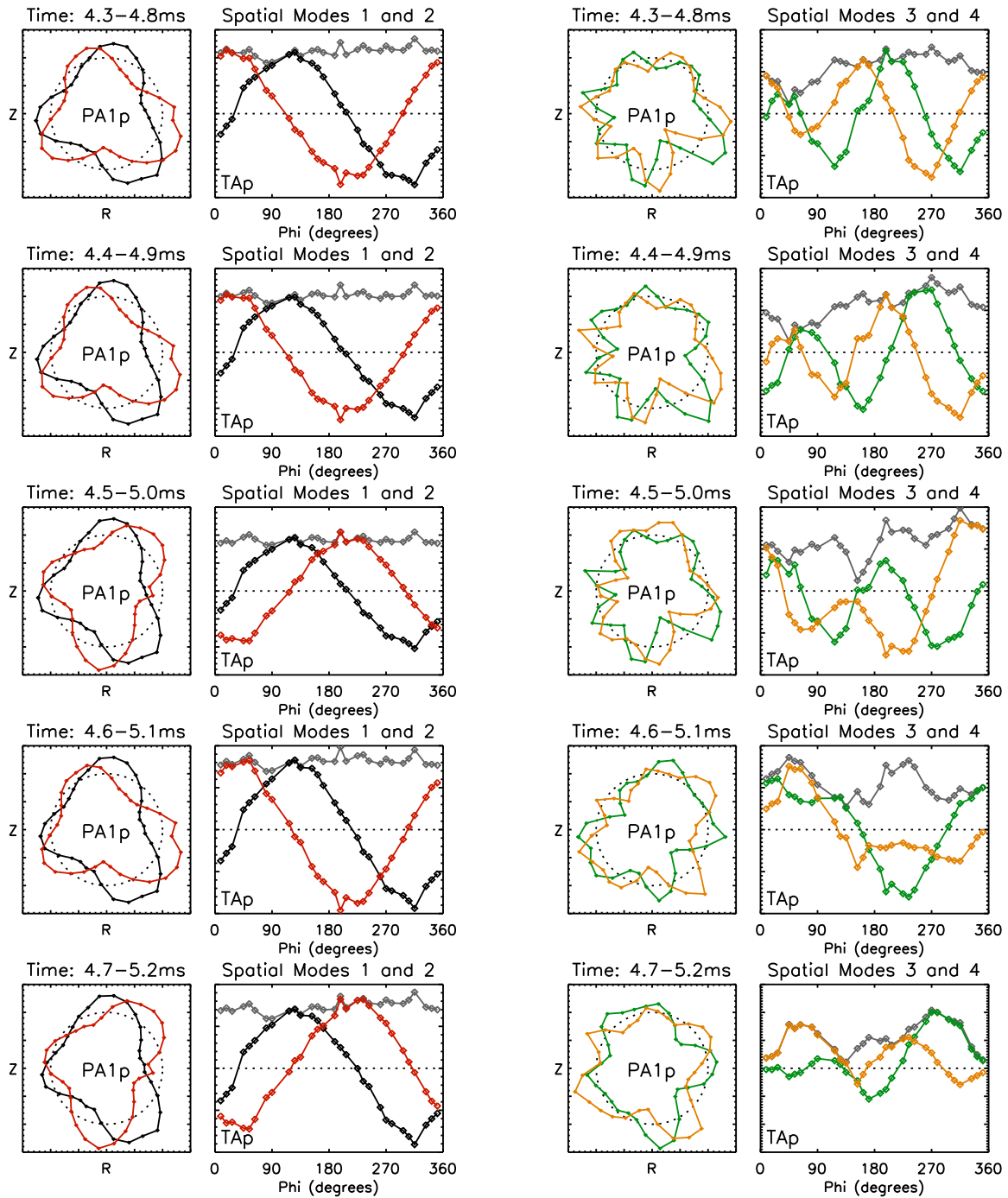
Figure 6.17: First four BD spatial modes for an *odd* wall configuration (shot 72953). Analysis intervals are 0.5 ms long, spaced by 0.1 ms, with time progressing downward. $\delta B_p$ modes are shown for one poloidal array and the toroidal array. The first mode pair is in the first two columns, while the second pair is in the last two columns. Gray lines in TA plots show local spatial mode amplitude.
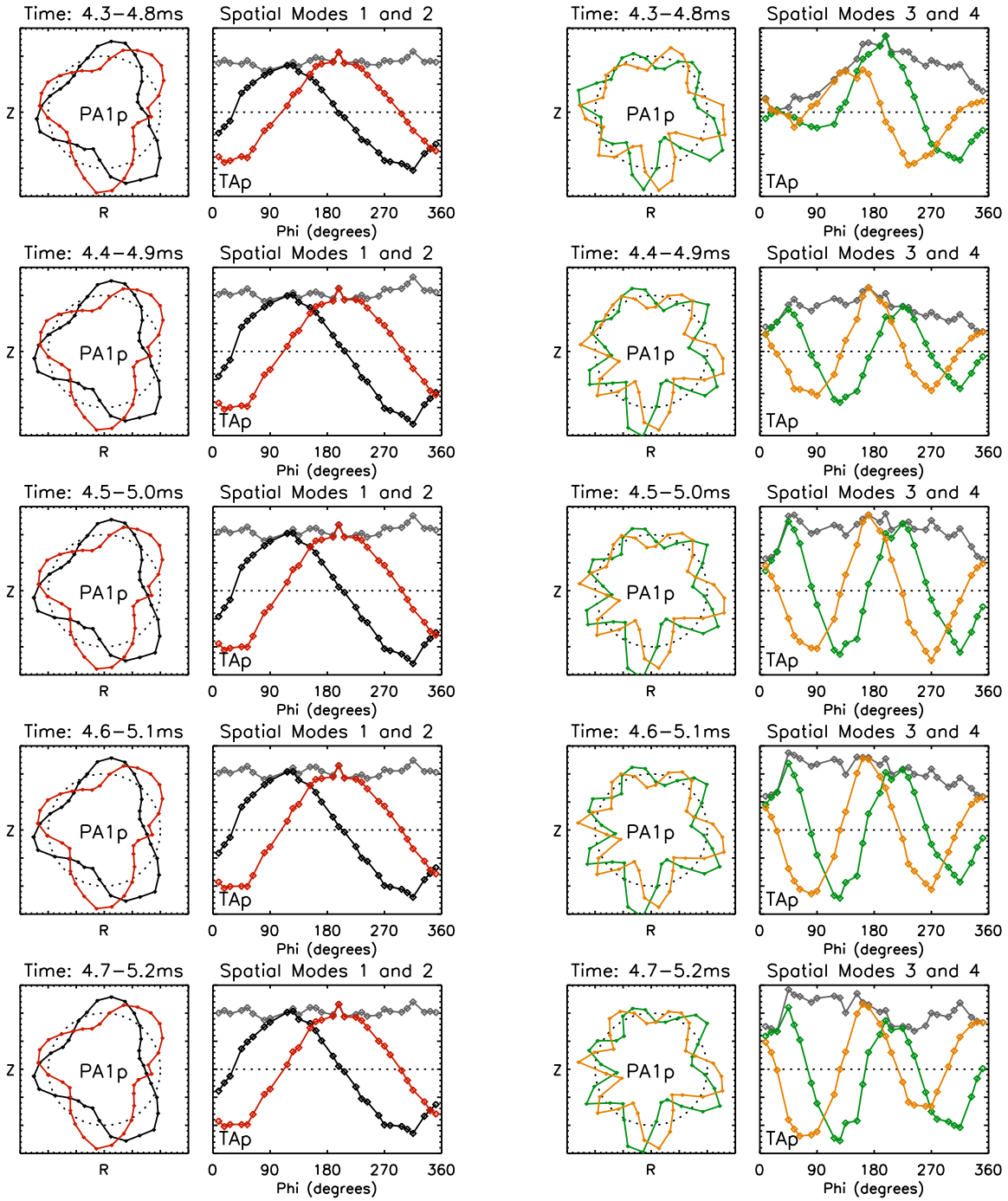
Figure 6.18: First four BD spatial modes for an *even* wall configuration (shot 73014). Analysis intervals are 0.5 ms long, spaced by 0.1 ms, with time progressing downward. $\delta B_p$ modes are shown for one poloidal array and the toroidal array. The first mode pair is in the first two columns, while the second pair is in the last two columns. Gray lines in TA plots show local spatial mode amplitude.
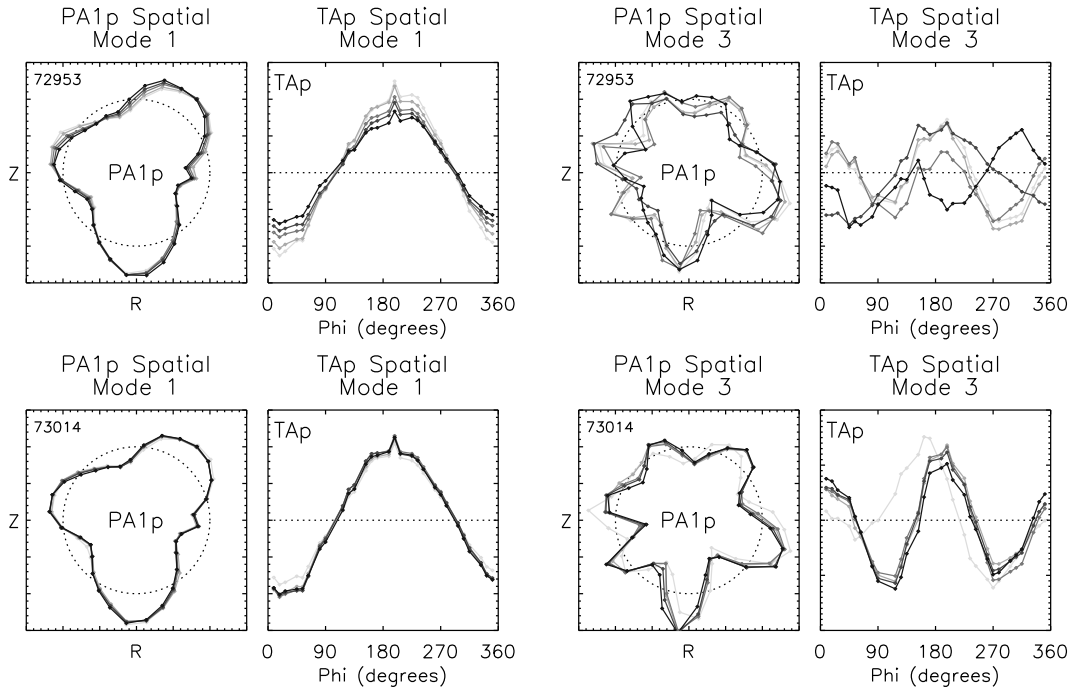
Figure 6.19: Spatial modes from Figures 6.17 and 6.18 overlaid for easier comparison. The first row is for the *odd* wall, while the second row is for the *even* wall. One mode from each quadrature pair is shown. Darker lines are for later times.

is different enough. The absence of bulging suggests that the lack of toroidal wall symmetry for these cases is not enough to enhance the toroidal mode number spectrum – *n is still a good quantum number*. This has important implications for magnetic feedback; a system designed for $n = 1$ feedback should not couple more strongly to $n = 2$ modes when wall asymmetries are introduced.

Modes from Figures 6.17 and 6.18 are overlaid in Figure 6.19 to easily compare how they evolve over time. The first mode in each case retains the same general 3/1 structure for all analysis windows. However for the odd wall case, the toroidal array spatial mode amplitude reduces over time. Since BD modes are normalized, this means the mode is getting stronger in other sensor sets. Feedback sensor spatial modes confirm that amplitudes are indeed getting relatively stronger on the low-field side. Thus the dominant mode balloons more over time for the odd wall.

The second mode pair is clearly 6/2 over the entire analysis period for the $n = even$ wall configuration. For the $n = odd$ wall, however, the second mode pair does not retain the same shape for the times shown. This suggests that the mode is not as coherent, or that other modes are competing for dominance. Also, the second mode's toroidal structure in the toroidal array is not as uniform for the *odd* wall as for the *even* wall.
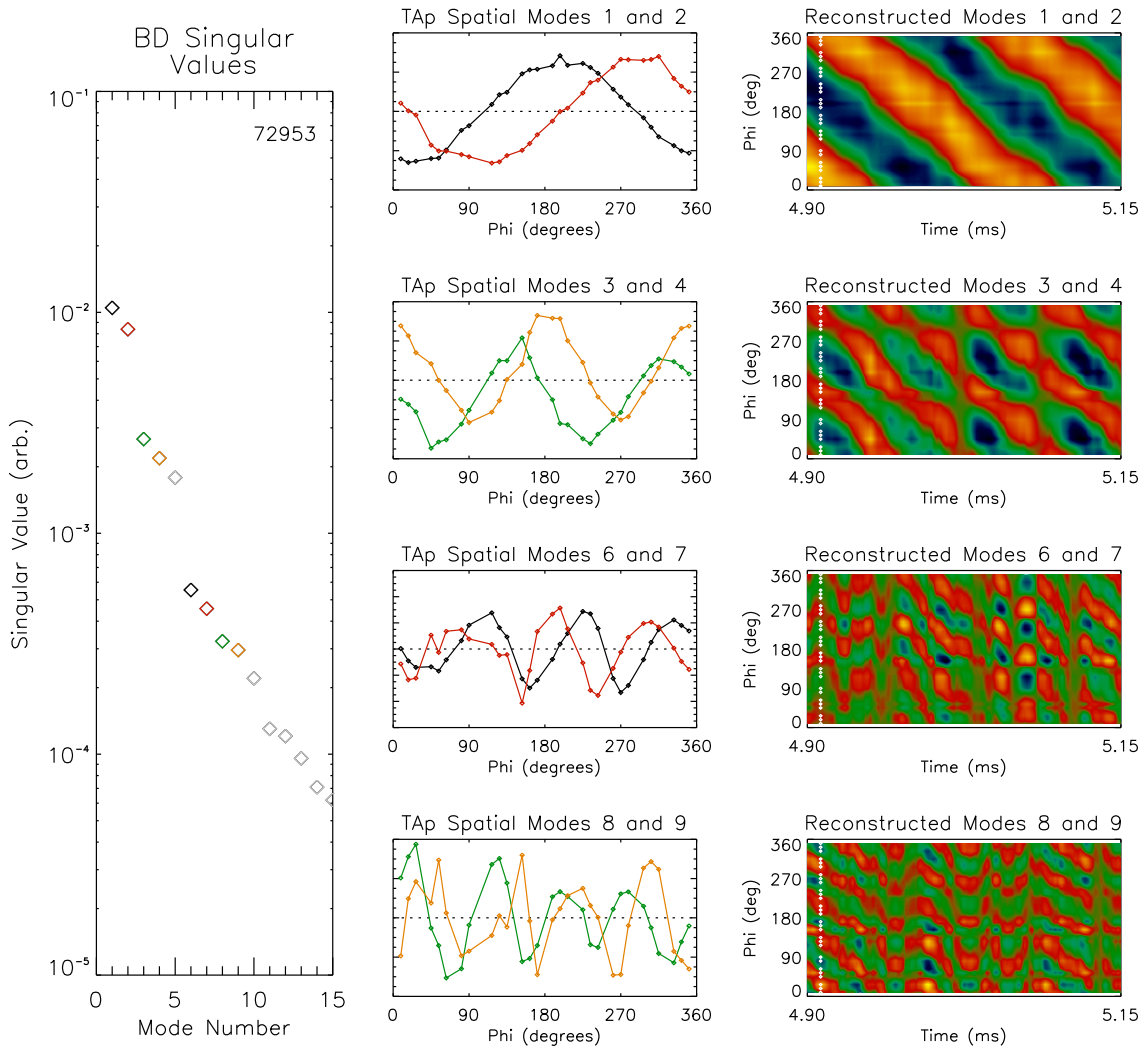
Figure 6.20: Singular values and spatial modes, analyzing only the poloidal field sensors in the toroidal array during 4.90–5.15 ms, for an *odd* wall configuration. Spatial modes are plotted using the same color as their respective singular values. BD mode number 5 is skipped since it is not associated with a quadrature pair. Reconstructions use Equation 3.7 to show the space-time evolution of each individual mode. Toroidal mode numbers are $n = 1, 2, 3$, and $4$.

**Modes found using only the toroidal array**

To isolate only toroidal mode number effects, the BD analysis was also done using only the toroidal array of sensors. When poloidal array sensors are included in the BD, they have a large influence on the mode structure computation since there are so many of them. Using only the TA sensors ensures that only toroidal features will determine the modes. Results of analyzing only TA sensors during 4.90–5.15 ms are shown in Figures 6.20 and 6.21. For comparison, a discharge with fully
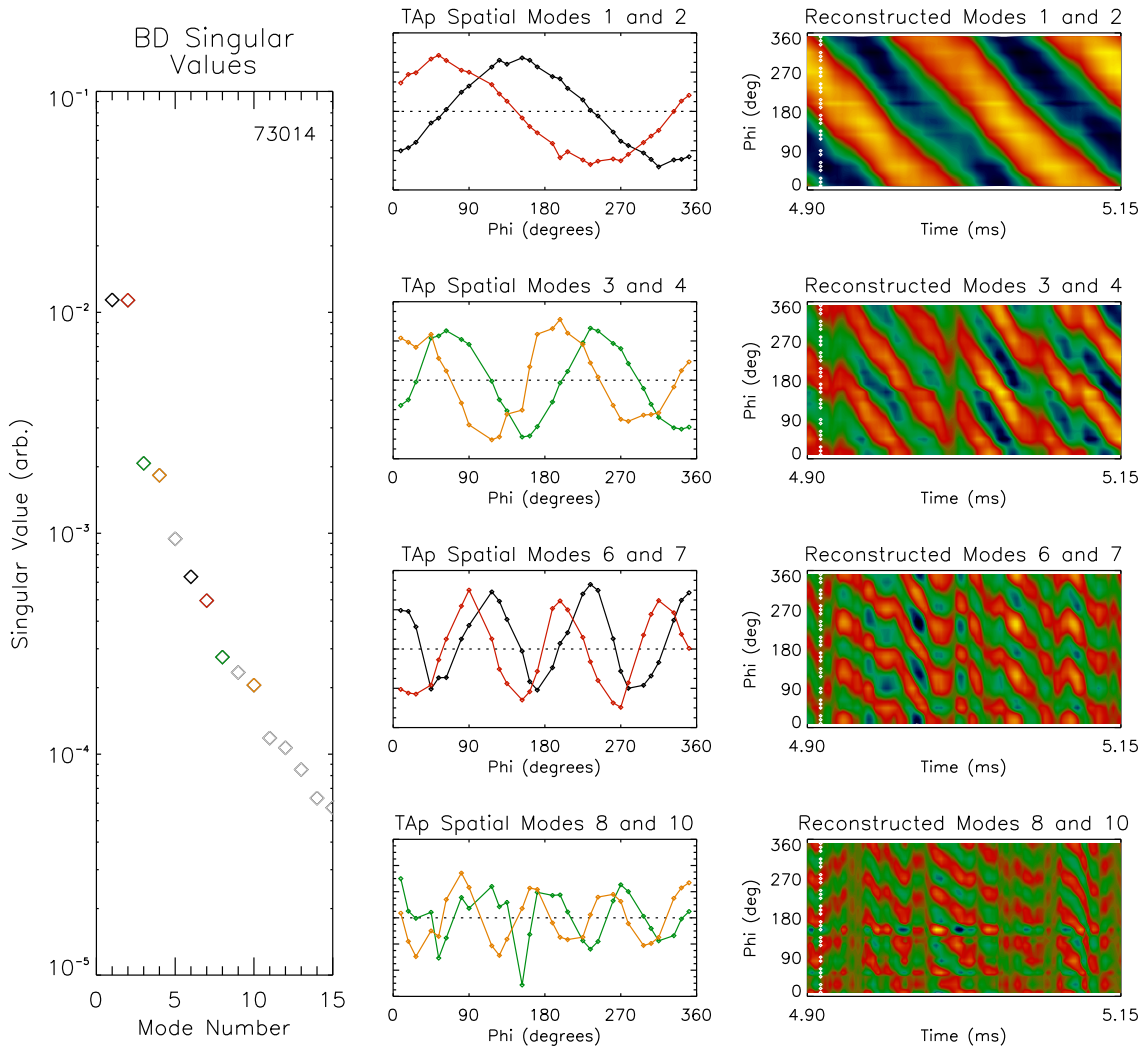
Figure 6.21: Singular values and spatial modes, analyzing only the poloidal field sensors in the toroidal array during 4.90–5.15 ms, for an *even* wall configuration. BD mode numbers 5 and 9 are skipped since they are not associated with quadrature pairs. Toroidal mode numbers are $n = 1, 2, 3$, and 4.

inserted walls and similar equilibrium evolution was also analyzed, as shown in Figure 6.22. The modes are easily identified with toroidal mode number 1, 2, 3, and 4, with no *a priori* assumption of basis. Reconstructed spatiotemporal modes have good coherence. When one of the poloidal arrays is included in the BD, it becomes difficult to pair coherent modes above $n = 2$, $m = 6$. This may be in part due to the lack of resolution for poloidal mode numbers higher than 8, if they are present.

Relative power in the $n = 1$–4 toroidal modes are compared for several shots with *even*, *odd*, and *normal* wall configurations in Figure 6.23. Mode energies are given relative to the $n = 1$ mode
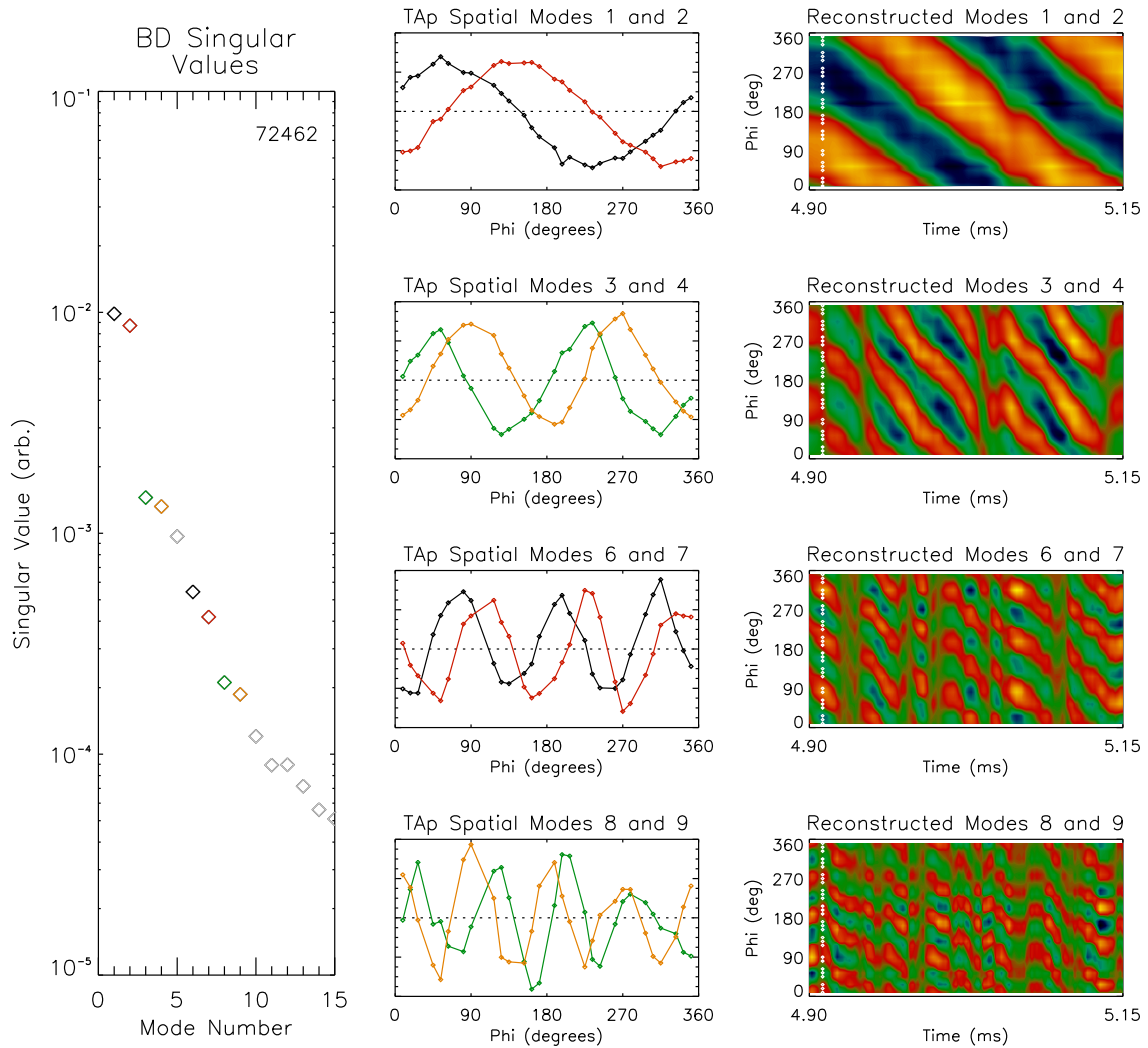
Figure 6.22: Singular values and spatial modes, analyzing only the poloidal field sensors in the toroidal array during 4.90–5.15 ms, for an *normal* wall configuration (shot 72462). BD mode numbers 5 and 9 are skipped since they are not associated with quadrature pairs. Toroidal mode numbers are $n = 1, 2, 3,$ and $4$.

energy to normalize across shots. Only seven discharges that were similar enough to be compared directly were available, including the three in Figures 6.20–6.22. Analysis was done using 0.25 and 0.50 ms long BD intervals. Since the singular values are used for these energies, they represent an average power over the analysis window. The large difference in $(n = 2)/(n = 1)$ power for shot 73013 is caused by the $n = 1$ mode growing significantly at the end of the longer time window, but not in the shorter window. The *even* toroidal mode numbers are seen to be more active for the *odd* wall than for the other two configurations, although there are not enough data to be conclusive,
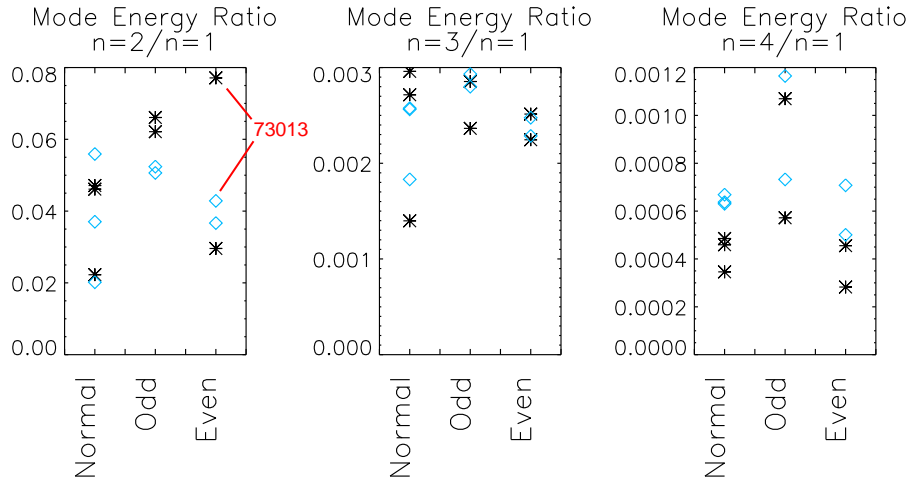
Figure 6.23: Mode energies of the $n = 2$, 3, and 4 modes relative to the $n = 1$ mode for seven similar discharges with different wall configurations. The x-axis denotes the wall configuration: normal (fully inserted) walls, odd wall, and even wall. The BD interval was 0.25 ms wide for the stars, and 0.5 ms wide for the diamonds.

especially given the large spread.

Given comparisons between the normal wall and odd wall in Figure 6.13, it is unlikely that the even-$n$ enhancement found here is statistically significant. However in Section 7.2.1 of Reference [40], Eisner found that an $n = 1$ wall from a previous HBT-EP shell generation produced more power in even-$n$ rotating modes than an axisymmetric wall.

## 6.4  Amplitude and rotation modulation

Retracting several wall sections has been shown to increase average mode amplitudes, as would be expected from the reduced wall stabilization. However, it is also possible that changing the wall geometry could produce phase-dependencies for mode growth and rotation rates. When the wall is non-axisymmetric, the degeneracy of a quadrature mode pair is broken. If a given mode orientation reduces coupling to the wall, that phase should be preferred for faster mode growth. Phase-dependent eddy-current amplitudes in the walls will also change the torque between the wall and the mode as a function of mode orientation. Simulations in VALEN predict that phase-dependent rotation modulation should be observable in HBT-EP when walls are asymmetrically retracted. Even in the case of nominally symmetric walls, diagnostic cutouts or alignment errors from the wall assembly could produce phase-dependent modulations, if the asymmetries are large enough.
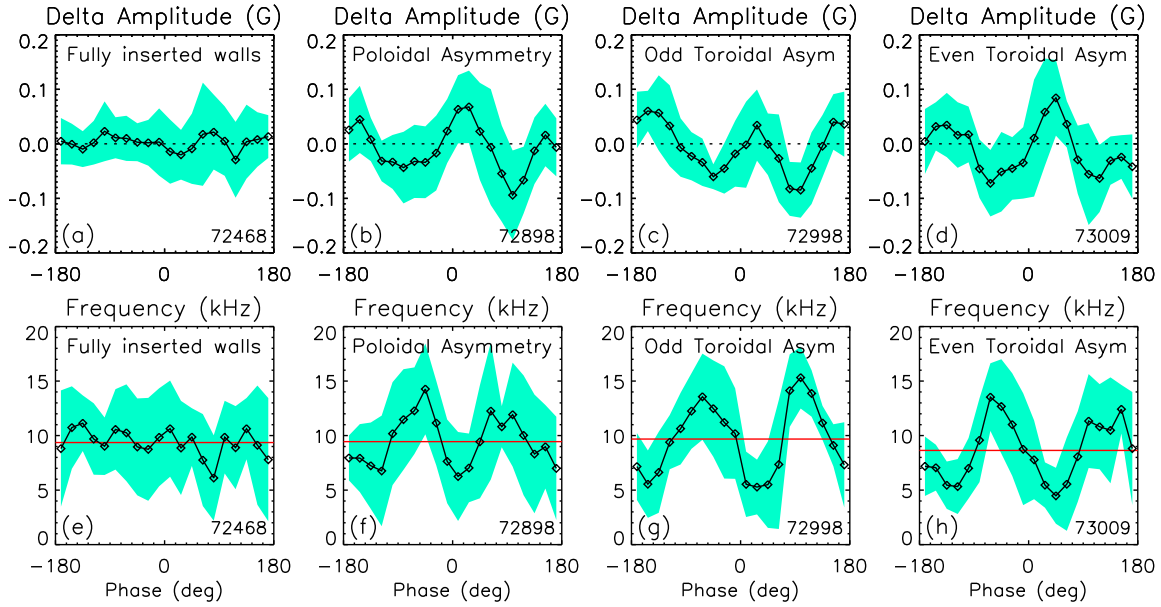
Figure 6.24: Instantaneous amplitude of the $n = 1$ mode, relative to averages over the surrounding period (a-d), and instantaneous frequency of the mode (e-h). Four discharges with different wall configurations were analyzed during the 4.5–5.5 ms period. Points are averaged in $18°$ sectors, with aqua regions showing the standard deviation for points within that sector. Modulations are indicated by the phase dependence seen for the asymmetric wall configurations.

To investigate amplitude and rotation modulations, similar discharges were selected from four wall configurations (fully-inserted walls, plus the three configurations in Figures 6.6 and 6.14). Biorthogonal decomposition was done over the same 1 ms interval for each shot, containing 3/1-dominated mode activity. Only sensors in the toroidal array were used since they gave purely toroidal mode information and did not move for any case. Only radial sensors were used because the poloidal signals were too noisy for the selected time interval. Mode amplitudes and phases were calculated using Equations 3.4 and 3.5. Since amplitudes can change significantly over several revolutions, averages were calculated using the surrounding period for each time point. The difference between instantaneous amplitude and the period-average is taken as the amplitude modulation.

Amplitude modulations versus phase for the $n = 1$ mode are shown in Figures 6.24 and 6.25, along with instantaneous rotation frequency versus phase. The arbitrary phase offsets in the BD modes have been corrected here to yield absolute phase of the mode's peak in lab coordinates. Average frequencies are mostly in the 8–10 kHz range, so the frequency modulations are actually very large. Eddy-currents have a negligible contribution to the toroidal array sensors at 10 kHz.

A phase dependence is seen for each asymmetric wall configuration, with the toroidal asymmetries
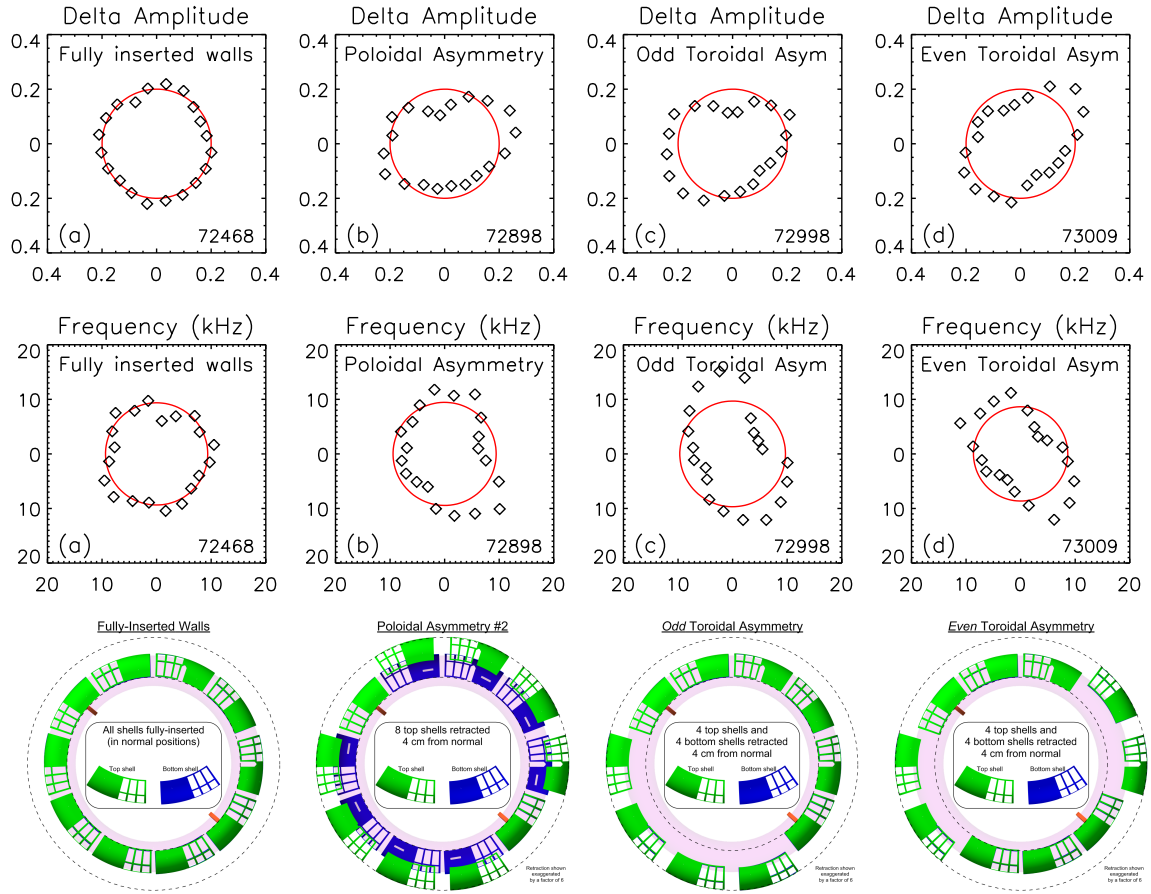
Figure 6.25: Instantaneous amplitude of the $n = 1$ mode, relative to averages over the surrounding period (a-d), and instantaneous frequency of the mode (e-h). These plots show the same sector-averaged information as Figure 6.24, but using polar plots to emphasize the toroidal phase dependence. The $\Delta$Amplitude plots include a 0.2G offset for the baseline circle. Points in the fully-inserted wall case fall along a zero-centered circle, showing a lack of phase-dependent modulation. The asymmetric wall configurations form ellipses, showing a phase dependence for amplitude and rotation frequency. Each wall configuration is shown in the bottom row.

arguably having the clearest dependence. Amplitudes and frequencies peak at two phases, with higher frequencies corresponding to lower amplitudes. As seen in Figure 6.25, amplitude peaks roughly line up with retracted wall sections. For the asymmetries considered, we could expect two peaks in the frequency modulations of $n = 1$ modes due to the phase-dependent torque between wall eddy-currents and the mode. Wall eddy-currents are driven by $\partial_t B_r(r = r_{wall})$ from the mode, thus a wall segment that is further from the plasma surface will have lower induced currents due to the field drop-off. The lesser wall current produces a lower field at the plasma surface, resulting in less $\vec{j}_{mode} \times \vec{B}$ torque on the mode. Since $|\partial_t B_r|$ in a given toroidal section peaks twice per

revolution, when the wall in that section is removed, the torque on the mode will be reduced twice per revolution.

These rotation modulations can have a significant impact on feedback performance. If only the average rotation frequency is used in a feedback scheme, then performance will be diminished, as the feedback may suppress or excite the mode depending on its phase. If variations in the frequency are tracked, then feedback performance may improve. Nevertheless, feedback using only average mode frequencies has been successful in previous HBT-EP research [43, 44].

## 6.5 Summary of asymmetric wall effects

Using an asymmetric wall configuration produced different mode behavior versus the fully-inserted wall configuration. Both dominant and secondary mode amplitudes were larger with the retracted walls. The strength of the secondary mode *relative* to the dominant mode was larger for the normal symmetric walls when plasmas were outboard-limited ($R_0 > 92\ cm$).

Poloidal mode structures changed slightly after retracting walls, with better peaking of the $m = 3$ content near $q_* = 2.8$ for symmetric walls. This can be seen by comparing Figure 5.7(b) with Figure 6.10(b,g). The $m = 4 \rightarrow 3$ transition for $n = 1$ modes occurs at lower $q_*$ with asymmetric walls, though the statistical significance of this observation has not been analyzed.

Phase-dependent modulations in amplitude and frequency of the dominant mode were observed for the asymmetric wall configurations. Modulations were most pronounced for the toroidal wall asymmetries.

# Chapter 7

# Conclusions and Future Studies

The research in this thesis presents the first systematic study of multimode external kinks in a tokamak, with mode structures that are directly measured using a high-resolution magnetic sensor set. Multiple coexisting modes were measured with no prior assumptions about mode structure or interactions. A major diagnostic and passive stabilizing wall upgrade in HBT-EP enabled these detailed measurements. Upgraded machine capabilities will continue to be used in additional experiments studying kink physics. Significant results from this thesis are summarized in the following sections.

**Experimental methods and analysis technique**

The biorthogonal decomposition was shown to be an effective analysis technique for studying kink mode dynamics with the HBT-EP magnetic sensor set when used properly. Coherent mode activity was measured without an *a priori* basis assumption. Toroidal mode numbers up to $n = 3$ were observed when using the full sensor set, and up to $n = 4$ when using only the toroidal array. In some cases up to $n = 5$ may have been seen, but quadrature pairs could not be found. Clear poloidal mode numbers up to $m = 8$ have been seen with the poloidal arrays.

Effects of a changing major radius on calculated BD modes were quantified. Spurious modes appeared when $R_0$ changed too much during the analysis interval – when a rotating mode is present with poloidal mode number $m$, spurious BD mode pairs with higher $m$-numbers are seen if the noise level is low enough. These modes have characteristic amplitude and phase evolutions which make them easier to identify when they appear. Spurious modes were avoided in statistical analysis by using intervals which were short enough for $\Delta R_0$ to be small, but long enough that rotating mode

structures were sufficiently sampled. This is especially important in HBT-EP, where the major radius may change significantly during periods of interest. The BD was also seen to accurately capture bursting mode activity, and has no problems with chirping mode frequencies.

**Multimode observations**

Transitions between dominant poloidal mode numbers were observed simultaneously for $n = 1$ and $n = 2$ modes. Specifically, $m = 4 \to 3/n = 1$ transitions were accompanied by simultaneous $m = 7 \to 6/n = 2$ transitions. Merging of peaks during the transition occurs on the high-field side of the torus for all cases that have been examined, which demonstrates the importance of having adequate poloidal coverage of sensors when determining poloidal mode structure.

Non-rigid behavior has been observed for multiple modes sharing the same helicity. Coexistent $m/n$=3/1 and 6/2 modes are seen to have differing phase velocities, and can slow down or speed up independently. A rigid mode structure would have the $n = 2$ mode rotating twice as fast as the $n = 1$ mode, but this is not what is observed in many cases. Amplitudes of the harmonic modes are also observed to be independent – 6/2 mode amplitude is not simply proportional to the 3/1 amplitude. During times of dominant 3/1 activity, the 6/2 mode is observed to modulate the 3/1 amplitude. Occasional bursts of 6/2 activity have been seen to dominate the mode structure over the 3/1 mode for brief periods, with no measured changes in the equilibrium. Multimode interactions can vary dramatically on a shot-to-shot basis, necessitating the use of statistics over many shots to establish trends.

Many discharges were analyzed to collect statistics with differing plasma and wall conditions. Discharges were analyzed while approaching the $q_* = 3$ resonance from different directions. In other words, the $q = 3$ surface was moved radially inward or outward to approach the plasma edge. The multimode nature of 3/1-dominated kink modes was found to be more significant when crossing the $q_* = 3$ resonance from above – when the 3/1 initially grows as an internal mode, then moves external, relative amplitudes of secondary ($n = 2$) modes are larger. This observation may be obscured by the possible existence of internal $n = 2$ modes, such as 5/2 tearing modes.

**Influence of wall geometry**

Retracting walls from their normal fully-inserted positions provided modes that were generally stronger in each asymmetric configuration. This was true for both the first and second BD mode

pairs. The enhancement may be a result of reduced wall stabilization when parts of the wall are far-
ther from the plasma – the effective average wall coverage is reduced. However, the second mode was
generally stronger relative to the first in the normal wall configuration in outboard-limited plasmas
($R_0 > 92\ cm$). The reason for this relative difference is unclear.

Shapes of the dominant modes are slightly different for the asymmetric wall cases versus the
normal walls, based on the poloidal mode spectral content. Normal symmetric walls produced
better peaking of $m = 3$ content near $q_* = 2.8$ across all major radii versus the asymmetric wall
cases. Appearance of $m = 4 - 6$ content in the dominant mode is shifted to larger major radii for
outboard-limited plasmas with poloidally or toroidally aysmmetric walls. In statistical treatments,
the toroidal mode number content did not change significantly with different wall configurations, at
least for $n = 1$ and $n = 2$. This implies that $n$ is still a good quantum number when the toroidal
wall symmetry is broken, which is important for the design of magnetic feedback systems.

Comparing several $n = even$ toroidal wall asymmetry discharges versus $n = odd$ and normal
walls showed slightly more power in $even$ toroidal mode numbers in the $odd$ wall cases. Here, modes
up to $n = 4$ were analyzed. Considering the spread in the data, this result may not be statistically
significant, especially given the results of many-shot analyses. However, this does agree with the
results in Section 7.2.1 of Reference [40], where an $n = odd$ wall produced more power in $n = even$
modes versus other tested wall configurations.

The $m = 4 \rightarrow 3$ transition was seen to take place at lower $q_*$ for toroidal and poloidal wall
asymmetries versus the normal wall. Spread in the data has not been quantified since only three
shots were analyzed. Again, this may not be statistically significant. There are not enough similar
discharges available in this case to determine the spread.

Mode amplitude and rotation modulations were observed for the asymmetric wall configurations.
Rotation modulations will negatively affect feedback performance if the phase-dependent mode ro-
tation is not accurately tracked. The modulations could presumably be compensated for with a
sophisticated feedback system.

## 7.1    Future studies

Multimode kink physics is an active research subject for advanced tokamak plasmas. The RFX
reversed field pinch experiment [32] has dedicated time to running as a tokamak in order to study

multimode feedback with modular coils [63]. Multimode VALEN computations are being used to examine RWM behavior at high $\beta_N$ and low $l_i$ in NSTX and advanced ITER scenarios [64, 65]. Significant multimode effects are predicted for steady-state (Scenario 4) ITER plasmas.

### 7.1.1 Multimode research on HBT-EP

Upcoming experiments in HBT-EP will continue to investigate multimode external kink behavior. Feedback studies using the active control coils with a new GPU-based controller [66] are currently in progress. Multimode kink response to applied feedback will be studied in detail. Experiments will explore how secondary modes respond to feedback on dominant modes, and vice-versa. The modular design of the control coils permits feedback using different coil sizes to see how sensitive the feedback results are to sideband content in the applied fields. If multimode responses are significant, larger sideband content when controlling the dominant mode is predicted to excite sub-dominant modes.

The present HBT-EP configuration still allows many more passive studies to be done. Modes seen by the high-resolution poloidal arrays could improve equilibrium reconstructions through best-fitting the mode structure with the $\lambda$ parameter, thereby determining $\beta_p + l_i/2$ [55]. This would require knowing the mode structure at the plasma surface instead of at the wall, which could in principle be determined using the radial and poloidal sensors together to separate plasma and eddy-current contributions to the sensor signals.

This thesis focused only on rotating modes. Any locked modes that are present in the data were removed during the equilibrium subtraction while extracting fluctuations. However, locked modes also exhibit multimode phenomena, and would be important to study due to their deleterious effects on plasmas. This could be especially interesting for the asymmetric wall cases, where locked modes should have a preferred phase to reduce wall coupling. The effects of static error fields on mode behavior is also an important topic; this could be investigated by using the active control coils to apply stationary non-axisymmetric fields.

The Multimude VALEN code can use the full 3D structure of HBT-EP to simulate passive resistive wall mode growth as well as mode behavior during active feedback. VALEN has simulated modes with retracted walls for previous conducting wall generations, but has not been used for retracted walls in the present upgraded configuration. These simulations will commence soon to compare simulated mode amplitude and rotation modulations to those observed in Section 6.4. This
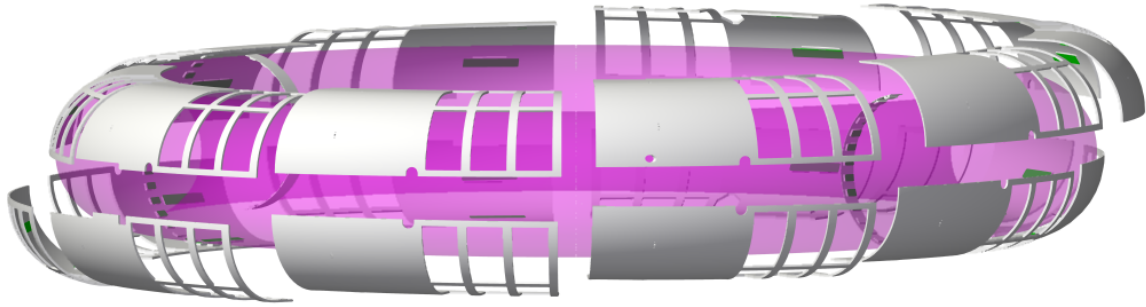
Figure 7.1: Example of a possible asymmetric wall configuration with $m = odd, n = 1$. In order to emphasize the structure, retractions are shown using a factor of 3 larger than what is possible in HBT-EP.

will be done in conjunction with detailed experiments measuring modulations with respect to the orientation of toroidal wall asymmetries. Simulations can also be done to find wall configurations that maximize the coupling between two specific modes through eddy-current patterns. An example $m = odd, n = 1$ wall is shown in Figure 7.1.

**Machine upgrades**

A shaping coil will soon be installed on the high-field-side of the torus, allowing diverted plasma operation [67]. This is predicted to change the multimode character of resistive wall modes by eliminating the edge helicity resonance [37]. Multimode studies will be done while scanning the shaping parameters.

An improved Thomson scattering system is presently being assembled. Internal measurements of the pressure profile for different discharge styles will permit systematic studies of multimode behavior under various pressure conditions. High- versus low-$\beta$ multimode behavior can be compared.

# Bibliography

[1] M. I. Hoffert, K. Caldeira, G. Benford, D. R. Criswell, C. Green, H. Herzog, A. K. Jain, H. S. Kheshgi, K. S. Lackner, J. S. Lewis, H. D. Lightfoot, W. Manheimer, J. C. Mankins, M. E. Mauel, L. J. Perkins, M. E. Schlesinger, T. Volk, and T. M. L. Wigley. Advanced Technology Paths to Global Climate Stability: Energy for a Greenhouse Planet. *Science*, **298**(5595):981–987, 2002.

[2] J. P. Freidberg. *Plasma Physics and Fusion Energy*. Cambridge University Press, 2007.

[3] C. L. Smith and S. Cowley. The path to fusion power. *Philosophical Transactions of the Royal Society A: Mathematical, Physical and Engineering Sciences*, **368**(1914):1091–1108, 2010.

[4] J. D. Lawson. Some Criteria for a Power Producing Thermonuclear Reactor. *Proceedings of the Physical Society. Section B*, **70**(1):6, 1957.

[5] J. Wesson. *Tokamaks*. Clarendon Press - Oxford, 1997.

[6] J. P. Freidberg. *Ideal Magnetohydrodynamics*. Plenum Press, New York, 1987.

[7] F. Troyon and R. Gruber. A semi-empirical scaling law for the $\beta$-limit in tokamaks. *Physics Letters A*, **110**(1):29 – 34, 1985.

[8] S. Kaye, M. Bell, R. Bell, S. Bernabei, J. Bialek, T. Biewer, W. Blanchard, J. Boedo, C. Bush, M. Carter, W. Choe, N. Crocker, D. Darrow, W. Davis, L. Delgado-Aparicio, S. Diem, J. Ferron, A. Field, J. Foley, E. Fredrickson, D. Gates, T. Gibney, R. Harvey, R. Hatcher, W. Heidbrink, K. Hill, J. Hosea, T. Jarboe, D. Johnson, R. Kaita, C. Kessel, S. Kubota, H. Kugel, J. Lawson, B. LeBlanc, K. Lee, F. Levinton, R. Maingi, J. Manickam, R. Maqueda, R. Marsala, D. Mastrovito, T. Mau, S. Medley, J. Menard, H. Meyer, D. Mikkelsen, D. Mueller, T. Munsat, B. Nelson, C. Neumeyer, N. Nishino, M. Ono, H. Park, W. Park, S. Paul, T. Peebles, M. Peng, C. Phillips, A. Pigarov, R. Pinsker, A. Ram, S. Ramakrishnan, R. Raman, D. Rasmussen,

M. Redi, M. Rensink, G. Rewoldt, J. Robinson, P. Roney, A. Roquemore, E. Ruskov, P. Ryan, S. Sabbagh, H. Schneider, C. Skinner, D. Smith, A. Sontag, V. Soukhanovskii, T. Stevenson, D. Stotler, B. Stratton, D. Stutman, D. Swain, E. Synakowski, Y. Takase, G. Taylor, K. Tritz, A. von Halle, M. Wade, R. White, J. Wilgen, M. Williams, J. Wilson, W. Zhu, S. Zweben, R. Akers, P. Beiersdorfer, R. Betti, T. Bigelow, M. Bitter, P. Bonoli, C. Bourdelle, C. Chang, J. Chrzanowski, C. Domier, L. Dudek, P. Efthimion, M. Finkenthal, E. Fredd, G. Fu, A. Glasser, R. Goldston, N. Greenough, L. Grisham, N. Gorelenkov, L. Guazzotto, R. Hawryluk, J. Hogan, W. Houlberg, D. Humphreys, F. Jaeger, M. Kalish, S. Krasheninnikov, L. Lao, J. Lawrence, J. Leuer, D. Liu, N. Luhmann, E. Mazzucato, G. Oliaro, D. Pacella, R. Parsells, M. Schaffer, I. Semenov, K. Shaing, M. Shapiro, K. Shinohara, P. Sichta, X. Tang, R. Vero, D. Walker, and W. Wampler. Progress towards high performance plasmas in the National Spherical Torus Experiment (NSTX). *Nuclear Fusion*, **45**(10):S168, 2005.

[9] J. Callen. Effects of 3D magnetic perturbations on toroidal plasmas. *Nuclear Fusion*, **51**(9):094026, 2011.

[10] T. Hender, J. Wesley, J. Bialek, A. Bondeson, A. Boozer, R. Buttery, A. Garofalo, T. Goodman, R. Granetz, Y. Gribov, O. Gruber, M. Gryaznevich, G. Giruzzi, S. Gnter, N. Hayashi, P. Helander, C. Hegna, D. Howell, D. Humphreys, G. Huysmans, A. Hyatt, A. Isayama, S. Jardin, Y. Kawano, A. Kellman, C. Kessel, H. Koslowski, R. L. Haye, E. Lazzaro, Y. Liu, V. Lukash, J. Manickam, S. Medvedev, V. Mertens, S. Mirnov, Y. Nakamura, G. Navratil, M. Okabayashi, T. Ozeki, R. Paccagnella, G. Pautasso, F. Porcelli, V. Pustovitov, V. Riccardo, M. Sato, O. Sauter, M. Schaffer, M. Shimada, P. Sonato, E. Strait, M. Sugihara, M. Takechi, A. Turnbull, E. Westerhof, D. Whyte, R. Yoshino, H. Zohm, D. the ITPA MHD, and M. C. T. Group. Chapter 3: MHD stability, operational limits and disruptions. *Nuclear Fusion*, **47**(6):S128, 2007.

[11] K. Shinohara, Y. Suzuki, S. Sakurai, K. Masaki, T. Fujita, and Y. Miura. Orbit Following Calculation of Energetic Ions in the Design of Ferritic Insertion in the JT-60U. *Plasma and Fusion Research*, **1**:7, 2006.

[12] K. C. Shaing, S. P. Hirshman, and J. D. Callen. Neoclassical transport fluxes in the plateau regime in nonaxisymmetric toroidal plasmas. *Physics of Fluids*, **29**(2):521–526, 1986.

[13] S. Sabbagh, A. Sontag, J. Bialek, D. Gates, A. Glasser, J. Menard, W. Zhu, M. Bell, R. Bell, A. Bondeson, C. Bush, J. Callen, M. Chu, C. Hegna, S. Kaye, L. Lao, B. LeBlanc, Y. Liu,

R. Maingi, D. Mueller, K. Shaing, D. Stutman, K. Tritz, and C. Zhang. Resistive wall stabilized operation in rotating high beta NSTX plasmas. *Nuclear Fusion*, **46**(5):635, 2006.

[14] W. Zhu, S. A. Sabbagh, R. E. Bell, J. M. Bialek, M. G. Bell, B. P. LeBlanc, S. M. Kaye, F. M. Levinton, J. E. Menard, K. C. Shaing, A. C. Sontag, and H. Yuh. Observation of Plasma Toroidal-Momentum Dissipation by Neoclassical Toroidal Viscosity. *Phys. Rev. Lett.*, **96**:225002, Jun 2006.

[15] J. Scoville, R. L. Haye, A. Kellman, T. Osborne, R. Stambaugh, E. Strait, and T. Taylor. Locked modes in DIII-D and a method for prevention of the low density mode. *Nuclear Fusion*, **31**(5):875, 1991.

[16] E. Lazzaro, R. J. Buttery, T. C. Hender, P. Zanca, R. Fitzpatrick, M. Bigi, T. Bolzonella, R. Coelho, M. DeBenedetti, S. Nowak, O. Sauter, and M. S. C. to the EFDA-JET work programme. Error field locked modes thresholds in rotating plasmas, anomalous braking and spin-up. *Physics of Plasmas*, **9**(9):3906–3918, 2002.

[17] L. Piron, L. Grando, G. Marchiori, L. Marrelli, P. Piovesan, A. Soppelsa, and D. Terranova. Dynamic decoupling and multi-mode magnetic feedback for error field correction in RFX-mod. *Nuclear Fusion*, **51**(6):063012, 2011.

[18] E. J. Strait. Stability of high beta tokamak plasmas. *Physics of Plasmas*, **1**(5):1415–1431, 1994.

[19] A. H. Boozer. Resistive wall modes and error field amplification. *Physics of Plasmas*, **10**(5):1458–1467, 2003.

[20] H. Reimerdes, M. S. Chu, A. M. Garofalo, G. L. Jackson, R. J. La Haye, G. A. Navratil, M. Okabayashi, J. T. Scoville, and E. J. Strait. Measurement of the Resistive-Wall-Mode Stability in a Rotating Plasma Using Active MHD Spectroscopy. *Phys. Rev. Lett.*, **93**:135002, Sep 2004.

[21] Y. In, I. Bogatu, A. Garofalo, G. Jackson, J. Kim, R. L. Haye, M. Lanctot, L. Marrelli, P. Martin, M. Okabayashi, H. Reimerdes, M. Schaffer, and E. Strait. On the roles of direct feedback and error field correction in stabilizing resistive-wall modes. *Nuclear Fusion*, **50**(4):042001, 2010.

[22] M. S. Chu and M. Okabayashi. Stabilization of the external kink and the resistive wall mode. *Plasma Physics and Controlled Fusion*, **52**(12):123001, 2010.

[23] C. Gimblett. On free boundary instabilities induced by a resistive wall. *Nuclear Fusion*, **26**(5):617, 1986.

[24] S. W. Haney and J. P. Freidberg. Variational methods for studying tokamak stability in the presence of a thin resistive wall. *Physics of Fluids B: Plasma Physics*, **1**(8):1637, 1989.

[25] A. H. Glasser and M. S. Chance. Bull. Am. Phys. Soc. **42**, 1848 (1997), abstract dMopP12.

[26] J. Bialek, A. H. Boozer, M. E. Mauel, and G. A. Navratil. Modeling of active control of external magnetohydrodynamic instabilities. *Physics of Plasmas*, **8**(5):2170–2180, 2001.

[27] A. H. Boozer. Simplified multimode calculations of resistive wall modes. *Physics of Plasmas*, **17**(7):072503, 2010.

[28] M. Baruzzo, T. Bolzonella, S. Guo, Y. Liu, G. Marchiori, R. Paccagnella, A. Soppelsa, F. Villone, and Z. Wang. 3D effects on RWM physics in RFX-mod. *Nuclear Fusion*, **51**(8):083037, 2011.

[29] T. S. Pedersen, D. Maurer, J. Bialek, O. Katsuro-Hopkins, J. Hanson, M. Mauel, R. James, A. Klein, Y. Liu, and G. Navratil. Experiments and modelling of external kink mode control using modular internal feedback coils. *Nuclear Fusion*, **47**(9):1293, 2007.

[30] M. Okabayashi, I. Bogatu, M. Chance, M. Chu, A. Garofalo, Y. In, G. Jackson, R. L. Haye, M. Lanctot, J. Manickam, L. Marrelli, P. Martin, G. Navratil, H. Reimerdes, E. Strait, H. Takahashi, A. Welander, T. Bolzonella, R. Budny, J. Kim, R. Hatcher, Y. Liu, and T. Luce. Comprehensive control of resistive wall modes in DIII-D advanced tokamak plasmas. *Nuclear Fusion*, **49**(12):125003, 2009.

[31] M. Okabayashi, J. Bialek, M. S. Chance, M. S. Chu, E. D. Fredrickson, A. M. Garofalo, M. Gryaznevich, R. E. Hatcher, T. H. Jensen, L. C. Johnson, R. J. L. Haye, E. A. Lazarus, M. A. Makowski, J. Manickam, G. A. Navratil, J. T. Scoville, E. J. Strait, A. D. Turnbull, and M. L. W. D.-D. Team. Active feedback stabilization of the resistive wall mode on the DIII-D device. *Physics of Plasmas*, **8**(5):2071–2082, 2001.

[32] P. Martin, J. Adamek, P. Agostinetti, M. Agostini, A. Alfier, C. Angioni, V. Antoni, L. Apolloni, F. Auriemma, O. Barana, S. Barison, M. Baruzzo, P. Bettini, M. Boldrin, T. Bolzonella, D. Bonfiglio, F. Bonomo, A. Boozer, M. Brombin, J. Brotankova, A. Buffa, A. Canton, S. Cappello, L. Carraro, R. Cavazzana, M. Cavinato, L. Chacon, G. Chitarin, W. Cooper, S. D.

Bello, M. D. Palma, R. Delogu, A. D. Lorenzi, G. D. Masi, J. Dong, M. Drevlak, D. Escande, F. Fantini, A. Fassina, F. Fellin, A. Ferro, S. Fiameni, A. Fiorentin, P. Franz, E. Gaio, X. Garbet, E. Gazza, L. Giudicotti, F. Gnesotto, M. Gobbin, L. Grando, S. Guo, Y. Hirano, S. Hirshman, S. Ide, V. Igochine, Y. In, P. Innocente, S. Kiyama, S. Liu, Y. Liu, D. L. Bruna, R. Lorenzini, A. Luchetta, G. Manduchi, D. Mansfield, G. Marchiori, D. Marcuzzi, L. Marrelli, S. Martini, G. Matsunaga, E. Martines, G. Mazzitelli, K. McCollam, S. Menmuir, F. Milani, B. Momo, M. Moresco, S. Munaretto, P. Nis, L. Novello, M. Okabayashi, S. Ortolani, R. Paccagnella, R. Pasqualotto, M. Pavei, G. Perverezev, S. Peruzzo, R. Piovan, P. Piovesan, L. Piron, A. Pizzimenti, N. Pomaro, N. Pomphrey, I. Predebon, M. Puiatti, V. Rigato, A. Rizzolo, G. Rostagni, G. Rubinacci, A. Ruzzon, H. Sakakita, R. Sanchez, J. Sarff, F. Sattin, A. Scaggion, P. Scarin, W. Schneider, G. Serianni, P. Sonato, E. Spada, A. Soppelsa, S. Spagnolo, M. Spolaore, D. Spong, G. Spizzo, M. Takechi, C. Taliercio, D. Terranova, V. Toigo, M. Valisa, M. Veranda, N. Vianello, F. Villone, Z. Wang, R. White, D. Yadikin, P. Zaccaria, A. Zamengo, P. Zanca, B. Zaniol, L. Zanotto, E. Zilli, G. Zollino, and M. Zuin. Overview of the RFX fusion science program. *Nuclear Fusion*, **51**(9):094023, 2011.

[33] R. Lorenzini *et al.* Self-organized helical equilibria as a new paradigm for ohmically heated fusion plasmas. *Nature Physics*, **5**:570–574, August 2009.

[34] R. Paccagnella, S. Ortolani, P. Zanca, A. Alfier, T. Bolzonella, L. Marrelli, M. E. Puiatti, G. Serianni, D. Terranova, M. Valisa, M. Agostini, L. Apolloni, F. Auriemma, F. Bonomo, A. Canton, L. Carraro, R. Cavazzana, M. Cavinato, P. Franz, E. Gazza, L. Grando, P. Innocente, R. Lorenzini, A. Luchetta, G. Manduchi, G. Marchiori, S. Martini, R. Pasqualotto, P. Piovesan, N. Pomaro, P. Scarin, G. Spizzo, M. Spolaore, C. Taliercio, N. Vianello, B. Zaniol, L. Zanotto, and M. Zuin. Active-Feedback Control of the Magnetic Boundary for Magnetohydrodynamic Stabilization of a Fusion Plasma. *Phys. Rev. Lett.*, **97**:075001, Aug 2006.

[35] S. Sabbagh, J. Berkery, R. Bell, J. Bialek, S. Gerhardt, J. Menard, R. Betti, D. Gates, B. Hu, O. Katsuro-Hopkins, B. LeBlanc, F. Levinton, J. Manickam, K. Tritz, and H. Yuh. Advances in global MHD mode stabilization research on NSTX. *Nuclear Fusion*, **50**(2):025020, 2010.

[36] M. Sankar, E. Eisner, A. Garofalo, D. Gates, T. Ivers, R. Kombargi, M. Mauel, D. Maurer, D. Nadle, G. Navratil, and Q. Xiao. Initial high beta operation of the HBT-EP Tokamak. *Journal of Fusion Energy*, **12**:303–310, 1993.

[37] D. A. Maurer, J. Bialek, P. J. Byrne, B. D. Bono, J. P. Levesque, B. Q. Li, M. E. Mauel, G. A. Navratil, T. S. Pedersen, N. Rath, and D. Shiraki. The high beta tokamak-extended pulse magnetohydrodynamic mode control research program. *Plasma Physics and Controlled Fusion*, **53**(7):074016, 2011.

[38] T. H. Ivers, E. Eisner, A. Garofalo, R. Kombargi, M. E. Mauel, D. Maurer, D. Nadle, G. A. Navratil, M. K. V. Sankar, M. Su, E. Taylor, Q. Xiao, R. R. Bartsch, W. A. Reass, and G. A. Wurden. Observation of wall stabilization and active control of low-n magnetohydrodynamic instabilities in a tokamak. *Physics of Plasmas*, **3**(5):1926–1934, 1996.

[39] R. Kombargi. *The Influence of a Conducting Wall on Disruptions in HBT-EP*. PhD thesis, Columbia University, 1997.

[40] E. C. Eisner. *The Effects of Wall Coverage, Symmetry, and Plasma-Wall Separation on the Stability of Tokamak Plasmas*. PhD thesis, Columbia University, 1998.

[41] C. Cates, M. Shilov, M. E. Mauel, G. A. Navratil, D. Maurer, S. Mukherjee, D. Nadle, J. Bialek, and A. Boozer. Suppression of resistive wall instabilities with distributed, independently controlled, active feedback coils. *Physics of Plasmas*, **7**(8):3133–3136, 2000.

[42] M. Mauel, J. Bialek, A. Boozer, C. Cates, R. James, O. Katsuro-Hopkins, A. Klein, Y. Liu, D. Maurer, D. Maslovsky, G. Navratil, T. Pedersen, M. Shilov, and N. Stillits. Dynamics and control of resistive wall modes with magnetic feedback control coils: experiment and theory. *Nuclear Fusion*, **45**(4):285, 2005.

[43] A. J. Klein, D. A. Maurer, T. S. Pedersen, M. E. Mauel, G. A. Navratil, C. Cates, M. Shilov, Y. Liu, N. Stillits, and J. Bialek. Suppression of rotating external kink instabilities using optimized mode control feedback. *Physics of Plasmas*, **12**(4):040703, 2005.

[44] J. M. Hanson, B. D. Bono, J. P. Levesque, M. E. Mauel, D. A. Maurer, G. A. Navratil, T. S. Pedersen, D. Shiraki, and R. W. James. A Kalman filter for feedback control of rotating external kink instabilities in the presence of noise. *Physics of Plasmas*, **16**(5):056112, 2009.

[45] D. A. Maurer, D. Shiraki, J. P. Levesque, J. Bialek, S. Angelini, P. Byrne, B. DeBono, P. Hughes, M. E. Mauel, G. A. Navratil, Q. Peng, D. Rhodes, N. Rath, and C. Stoafer. High resolution detection and excitation of resonant magnetic perturbations in a wall-stabilized tokamak. *Physics of Plasmas*, **19**(5):056123, 2012.

[46] D. Shiraki. *High-Resolution MHD Spectroscopy of External Kinks in a Tokamak Plasma*. PhD thesis, Columbia University, 2012.

[47] S. A. Sabbagh, R. E. Bell, J. E. Menard, D. A. Gates, A. C. Sontag, J. M. Bialek, B. P. LeBlanc, F. M. Levinton, K. Tritz, and H. Yuh. Active Stabilization of the Resistive-Wall Mode in High-Beta, Low-Rotation Plasmas. *Phys. Rev. Lett.*, **97**:045004, Jul 2006.

[48] J. P. Levesque, B. A. DeBono, J. M. Hanson, R. James, M. E. Mauel, D. A. Maurer, G. A. Navratil, T. S. Pedersen, and D. Shiraki. Soft X-ray Analysis of HBT-EP Plasmas. *Bulletin of the American Physical Society*, JP6.00101, 2008.

[49] M. Greenwald. Density limits in toroidal plasmas. *Plasma Physics and Controlled Fusion*, **44**(8):R27, 2002.

[50] B. A. Grierson, M. W. Worstell, and M. E. Mauel. Global and local characterization of turbulent and chaotic structures in a dipole-confined plasma. *Physics of Plasmas*, **16**(5):055902, 2009.

[51] S. Benkadda, T. D. de Wit, A. Verga, A. Sen, A. team, and X. Garbet. Characterization of Coherent Structures in Tokamak Edge Turbulence. *Phys. Rev. Lett.*, **73**:3403–3406, Dec 1994.

[52] C. Nardone. Multichannel fluctuation data analysis by the singular value decomposition method. Application to MHD modes in JET. *Plasma Physics and Controlled Fusion*, **34**(9):1447, 1992.

[53] T. D. de Wit, A.-L. Pecquet, J.-C. Vallet, and R. Lima. The biorthogonal decomposition as a tool for investigating fluctuations in plasmas. *Physics of Plasmas*, **1**(10):3288–3300, 1994.

[54] J. S. Kim, D. H. Edgell, J. M. Greene, E. J. Strait, and M. S. Chance. MHD mode identification of tokamak plasmas from Mirnov signals. *Plasma Physics and Controlled Fusion*, **41**(11):1399, 1999.

[55] O. Klüber, H. Zohm, H. Bruhns, J. Gernhardt, A. Kallenbach, and H. Zehrfeld. MHD mode structure and propagation in the ASDEX tokamak. *Nuclear Fusion*, **31**(5):907, 1991.

[56] V. D. Shafranov. "Plasma Equilibrium in a Magnetic Field," in *Reviews of Plasma Physics*, edited by M. A. Leontovich, Vol 2, Consultants Bureau, New York (1966).

[57] M. A. Shilov. *Measurement of the Response of External Kink Modes to Resonant Magnetic Perturbation in HBT-EP Tokamak Plasmas*. PhD thesis, Columbia University, 2005.

[58] D. J. Ward. The effect of partial poloidal wall sections on the wall stabilization of external kink modes. *Physics of Plasmas*, **3**(10):3653–3660, 1996.

[59] R. Fitzpatrick. Effect of a nonuniform resistive wall on the stability of tokamak plasmas. *Physics of Plasmas*, **1**(9):2931–2939, 1994.

[60] E. Strait, J. Bialek, N. Bogatu, M. Chance, M. Chu, D. Edgell, A. Garofalo, G. Jackson, T. Jensen, L. Johnson, J. Kim, R. L. Haye, G. Navratil, M. Okabayashi, H. Reimerdes, J. Scoville, A. Turnbull, M. Walker, and the DIIID Team. Resistive wall stabilization of high-beta plasmas in DIIID. *Nuclear Fusion*, **43**(6):430, 2003.

[61] E. J. Strait, J. M. Bialek, I. N. Bogatu, M. S. Chance, M. S. Chu, D. H. Edgell, A. M. Garofalo, G. L. Jackson, R. J. Jayakumar, T. H. Jensen, O. Katsuro-Hopkins, J. S. Kim, R. J. L. Haye, L. L. Lao, M. A. Makowski, G. A. Navratil, M. Okabayashi, H. Reimerdes, J. T. Scoville, A. D. Turnbull, and D.-D. Team. Resistive wall mode stabilization with internal feedback coils in DIII-D. *Physics of Plasmas*, **11**(5):2505–2513, 2004.

[62] M. Okabayashi, J. Bialek, A. Bondeson, M. Chance, M. Chu, A. Garofalo, R. Hatcher, Y. In, G. Jackson, R. Jayakumar, T. Jensen, O. Katsuro-Hopkins, R. L. Haye, Y. Liu, G. Navratil, H. Reimerdes, J. Scoville, E. Strait, M. Takechi, A. Turnbull, P. Gohil, J. Kim, M. Makowski, J. Manickam, and J. Menard. Control of the resistive wall mode with internal coils in the DIIID tokamak. *Nuclear Fusion*, **45**(12):1715, 2005.

[63] M. Baruzzo, T. Bolzonella, R. Cavazzana, G. Marchiori, L. Marrelli, P. Martin, R. Paccagnella, P. Piovesan, L. Piron, A. Soppelsa, P. Zanca, Y. in, Y. Liu, M. Okabayashi, M. Takechi, and F. Villone. Resistive Wall Modes Identification and Control in RFX-mod low qedge tokamak discharges. In *APS Meeting Abstracts*, page 4006, November 2011.

[64] J. Bialek, S. A. Sabbagh, L. Delgado-Aparicio, and S. P. Gerhardt. Multi-mode RWM analysis of NSTX high beta plasmas. In *APS Meeting Abstracts*, page 9059P, November 2010.

[65] S. A. Sabbagh *et al.* Stabilization of Low Internal Inductance Plasmas and First RWM State Space Control Experiments in NSTX. *15th Workshop on MHD Stability Control*, 2010.

[66] N. Rath, J. Bialek, P. Byrne, B. DeBono, J. Levesque, B. Li, M. Mauel, D. Maurer, G. Navratil, and D. Shiraki. High-speed, multi-input, multi-output control using GPU processing in the HBT-EP tokamak. *Fusion Engineering and Design*, (Article in Press), 2012.

[67] P. Byrne, D. Shiraki, J. P. Levesque, D. A. Maurer, M. E. Mauel, and N. Rath. Multimode MHD Stability Investigations using Plasma Shaping on HBT-EP. *Bulletin of the American Physical Society*, TP9.00115, 2011.